



UNIVERSITÀ DI PISA

**Methods for quantitative analysis  
of brain micro-architecture:  
application to animal model of  
autism and claustral organization**

DOCTORAL SCHOOL OF ENGINEERING "LEONARDO DA VINCI"  
PhD Program on Automatic, Robotics and Bioengineering  
XXVIII CYCLE

SSD: ING-IND/34

*Author:*

Chiara Magliaro

*Tutors:*

Prof. Arti Ahluwalia

Eng. Nicola Vanello

2013 - 2015



University of Pisa  
Research Center E. Piaggio  
Automatic, Robotics and Bioengineering  
PhD Cycle XXVIII (2013-2015)

Thesis title:  
Methods for quantitative analysis of brain micro-architecture:  
application to animal model of autism and claustral organization

*Author:* Chiara Magliaro

*Supervisor:* Prof. Arti Ahluwalia

*Supervisor:* Eng. Nicola Vanello



---

*"THE BRAIN is wider than the sky,  
For, put them side by side,  
The one the other will include  
With ease, and you beside."  
(E. Dickinson)*

*To my grandfather, Ercole*

---

# Abstract

One of the grand challenges of digital imaging in the field of neuroanatomy is the ability to extensively quantify anatomical structures and thus investigate the brain's structure-function relationship in great detail.

In the light of this challenge, my PhD thesis aims to investigate the brain's micro-structure to obtain faithful and reproducible information on neuron morphology within their native three-dimensional arrangement. A rigorous work-flow was designed, that integrates delipidation methods, advanced imaging techniques and image processing algorithms to better understand neural micro-structure and its contribution to neural function. In particular, the work-flow provides i) the optimization and standardization, through the quantification of non-invasive and macroscopic indices, of the CLARITY2 protocol, a tissue clarification method which eliminates lipids and reduces tissue scattering from thick brain slices, ii) the development of a Smart Region Growing (SmRG) algorithm for single neuron tracing from confocal three-dimensional datasets representing densely packed neurons within the brain, and iii) the implementation of N3MO, an open-source tool for quantitative morphometric extraction and multivariate analysis of neurons.

The work-flow was then applied to two case studies. The first aims to investigate sexual dimorphism in animal models of autism, because of the unbalanced incidence of the disorder in males and females. The second study is focused on the assessment of neural organization in the claustrum, giving the basis for distinguishing the different neuronal types with respect to their shape.



# Contents

<b>1</b>	<b>Introduction</b>	<b>1</b>
<b>2</b>	<b>Clarifying CLARITY: quantitative optimization of the diffusion-based delipidation protocol</b>	<b>15</b>
2.1	From brain tissue to confocal acquisition: tissue clearing protocol standardization and optimization . . . . .	17
2.2	Optimization method for perfused and genetically labelled tissues . . . . .	20
2.2.1	Materials and Methods . . . . .	20
2.2.2	Results . . . . .	26
2.3	Optimization method for perfused and un-labelled tissues . . . . .	32
2.3.1	Materials and Methods . . . . .	32
2.3.2	Quantification of the proteins lost in solution . . . . .	33
2.3.3	Results . . . . .	34
2.4	Customization of the CLARITY2 protocol for un-perfused tissues . . . . .	36
2.4.1	Materials and Methods . . . . .	37
2.4.2	Results . . . . .	38
2.5	Discussion . . . . .	39
<b>3</b>	<b>SmRG: a Smart Region-Growing algorithm for single-neuron tracing</b>	<b>43</b>
3.1	State of Art of algorithms and tools for neuron 3D tracing from confocal stack acquisitions . . . . .	44
3.2	SmRG algorithm description . . . . .	49
3.3	SmRG algorithm performance evaluation . . . . .	52

3.3.1	SmRG vs manual tracing . . . . .	54
3.3.2	SmRG vs standard 3D region growing algorithm . . . . .	57
3.3.3	A “Self validation” approach on segmented somata . . . . .	59
3.3.4	SmRG algorithm vs Tree2Tree tools . . . . .	61
3.4	Discussion . . . . .	62
<b>4</b>	<b>N3MO: a NEuron MORphological analysis tool for 3D morphometrics</b>	<b>67</b>
4.1	Introduction . . . . .	68
4.2	N3MO development and implementation . . . . .	70
4.3	N3MO: an outline . . . . .	72
4.3.1	Loading an image stack in N3MO . . . . .	72
4.3.2	3D neuron Tracing with SmRG . . . . .	73
4.3.3	Datamatrix creation . . . . .	73
4.3.4	Neuron Skeletonization . . . . .	75
4.3.5	3D morphological analysis . . . . .	75
4.3.6	Global 3D morphometric parameters . . . . .	80
4.3.7	Multivariate analysis . . . . .	82
4.4	N3MO vs ImageJ [1] . . . . .	84
4.5	Discussion . . . . .	84
4.6	Conclusion . . . . .	88
<b>5</b>	<b>Study of sexual dimorphism in murine models of autism</b>	<b>89</b>
5.1	A survey on the Autism Spectrum Disorders . . . . .	90
5.1.1	The cerebellum and the ASDs . . . . .	90
5.1.2	The importance of murine models for the study of neurological disorders and od ASDs . . . . .	92
5.1.3	Sexual Dimorphism in the brain and in ASDs . . . . .	96
5.2	Sexual dimorphism in REELER model of autism: a proof of concept . . . . .	101
5.2.1	Materials and Methods . . . . .	101
5.2.2	Results . . . . .	106
5.2.3	Discussion . . . . .	109
5.3	From NeMo to N3MO: application of the designed work-flow to the Engrailed murine model of autism . . . . .	110
5.3.1	Materials and Methods . . . . .	110
5.3.2	Results . . . . .	111
5.3.3	Discussion . . . . .	119
5.4	Conclusion . . . . .	124

<b>6</b>	<b>A starting point for the study of claustral organization</b>	<b>127</b>
6.1	What is the function of the claustrum? . . . . .	128
6.1.1	Neuron cell types in mammalian claustrum . . . . .	131
6.2	Parvalbumin-immunoreactive neuron classification in dog claustrum his- tological sections: a proof of concept . . . . .	133
6.2.1	Materials and Methods . . . . .	133
6.2.2	Results . . . . .	135
6.2.3	Discussion . . . . .	137
6.3	A starting point to unravel the mystery of the human claustrum . . . . .	138
6.3.1	Materials and Methods . . . . .	138
6.3.2	Results . . . . .	141
6.3.3	Discussion . . . . .	144
6.4	Conclusion . . . . .	145
	<b>Conclusions</b>	<b>151</b>
	<b>List of Publications</b>	<b>158</b>
	<b>Bibliography</b>	<b>159</b>



# List of Figures

1.1	The penetration depth and resolution of modern imaging techniques for brain tissues. The methods on the left are primarily limited by light scattering, whereas methods to the right are limited by light attenuation in tissue, a parameter that depends on both absorption and scattering. Abbreviations: OPT: Optical Projection Tomography, 2P/MP: two-photon/multi-photon, fPAM: functional Photo-Acoustic Microscopy, hFMT: hybrid Fluorescence Molecular Tomography, MSOT: Multi-Spectral Opto-acoustic Tomography, SPIM: Selective Plane Illumination Microscopy, MFT: Mesoscopic Fluorescence Tomography. [2] . . . . .	5
1.2	From traditional brain imaging to direct volume imaging, thanks to the advance in optical microscopy and delipidation methods. . . . .	8
1.3	The work-flow designed for the study of brain micro-architecture. After brain tissue clarification, standardized and optimized as detailed in Chapter 2, and, if needed, an immuno-labelling procedure to highlight structures of interest (i.e. Tubulin III antibody to label all mammalian neurons), three-dimensional datasets were obtained using a confocal microscope. The stacks were then processed with the SmRG algorithm, described in Chapter 3, for single neuron tracing. Then, each three-dimensional structure obtained was analysed with N3MO, whose features are described in Chapter 4, to extract morphometric variables and store the data obtained; if needed, data can be also analysed using statistical multivariate analysis (i.e. 3-way PCA) . . . . .	11

2.1 Schematic work-flow with the standardization procedures established, from tissue harvesting to confocal acquisition, for **A** perfused and genetically labelled tissues (green path), **B** perfused and non genetically-labelled tissue (blue path) and **C** non perfused and non-genetically labelled tissues (red path). . . . . 19

2.2 Photographs of cerebellar slices at different clearing times. The images were used to calculate BTCi through equation 2.1, comparing the intensity of the black line below the slice and in the region without the slice. (pixel size: 0.125 mm) . . . . . 23

2.3 **A** BTCi as a function of clearing time for control cerebellar slices in PBS (n=5, red) and in CLARITY clearing solution (n=5, blue) slices. **B** Cumulative GFP measured in the clearing solution over time (n=5 slices). **C** Fraction of GFP retained ( $GFP_{fr}$ ), expressed as in equation 2.4, showing no significant differences between slices at the same time point. **D** BTCi and  $GFP_{fr}$  time series obtained grouping results from the 5 different slices together, showing the relationship between the two parameters. . . . . 27

2.4 **(A)** Mean pixel intensity (MPI) as a function of stack depth for tissue slices immersed in clearing solution for different times (n=2 slices per line). **(B)** MPI for controls (n=2 slices per line). **(C)** CNR (contrast to noise ratio) as a function of stack depth for tissue slices immersed in clearing solution for different times (n=2 slices per line). **(D)** MPI for controls (n=2 slices per line). For each sample acquired, the MPI and CNR were calculated over 200  $\mu$ m thick regions from 100 different images spaced 2  $\mu$ m apart, i.e. a total of 100 data points). . . . . 30

2.5 Volume view of a confocal stack acquired at day 5 (Ex/Em: 488/502, pixel-to micron ratio size: 0.62  $\mu$ m , z-resolution: 1.2  $\mu$ m). Volume dimensions (w\*h): 317\*317\*172  $\mu$ m (numbers in the edges of the box represent distances in microns). . . . . 31

2.6 BTCi and  $P_{fr}$  time series obtained grouping results from the 5 different slices together, showing the relationship between the two parameters. . . 35

2.7 Confocal image acquired at day 5 (Ex/Em: 561/594, pixel-to micron ratio size: 0.31  $\mu$ m), representing a detail of *substantia nigra* SERT-positive neurons. . . . . 36

2.8 BCTi as a function of clearing time for 1mm- (n=12, blue), 500  $\mu$ m- (n=12, red) and 250  $\mu$ m- (n=12, green) human brain slices. . . . . 39

---

3.1	Images from the same confocal stack, representing L7GFP clarified murine Purkinje neurons, and relative histogram for <b>(A)</b> $z = 0 \mu$ and <b>(B)</b> $z = 100 \mu\text{m}$ . . . . .	45
3.2	Image from a confocal dataset representing L7GFP clarified murine Purkinje cells: in-plane signal differences due to biological variability are evident. . . . .	46
3.3	Algorithm work-flow: after a pre-processing step, soma are identified and the SmRG algorithm is run to trace all the neurons in the stack. . .	49
3.4	Volume rendering of <b>(A)</b> an original stack (Ex/Em: 488/502, pixel-to-micron ratio size: $0.62 \mu\text{m}$ , z-resolution: $1.2 \mu\text{m}$ ) and of <b>(B)</b> a $3*3*3$ median-filtered and interpolated stack. . . . .	50
3.5	<b>(A)</b> 2D image from an original stack chosen by the user (Ex/Em: 488/502, pixel-to-micron ratio size: $0.62 \mu\text{m}$ , z-resolution: $1.2 \mu\text{m}$ ) and <b>(B)</b> after the Hugh transform, which identifies somata and their relative soma center coordinates. The outputs are subsequently used as initial seed for the SmRG algorithm. . . . .	51
3.6	An example of SmRG algorithm output. The input confocal dataset represents stacks from clarified L7GFP murine cerebellum slices. Different colours refer to different structures segmented with the SmRG algorithm. . . . .	53
3.7	<b>(A)</b> The scroll down menu to visualize the images constituting the confocal dataset and to identify the neuron structure manually; <b>(B)</b> ImageJ 3D viewer automatically refreshed. . . . .	56
3.8	The residual error estimation for $n=20$ neurons. The residuals are the differences between the Surface-to-Volume ratio in the Purkinje cells segmented manually and with the SmRG algorithm. . . . .	57
3.9	An example of a neuron segmented with <b>(A)</b> the SmRG algorithm and <b>(B)</b> manually by an experts. For visually comparing the results, a merge of them is shown in <b>(C)</b> . . . . .	59
3.10	Two examples of neuron structures segmented with the SmRG algorithm and with a standard 3D region growing algorithm. To highlight the differences between the two techniques, a merge of them is shown in the last column. . . . .	60
3.11	Hough transform-based circle detection applied on an specific z-plane of <b>(A)</b> the original stack and <b>(B)</b> the stack segmented with the SmRG algorithm . . . . .	61

---

---

3.12	Residual error for n=20 soma. The residuals are the difference between soma radii obtained by the SmRG algorithm and by Matlabs <i>imfindcircles</i> function. Maximum error: 14%	62
3.13	Fruit fly <i>Drosophila</i> neuron dataset, processed with <b>(A)</b> the SmRG algorithm and <b>(B)</b> Tree2Tree tool.	63
3.14	A Purkinje cell 3D-printed using a Stratasys Fortus 450mc (Stratasys)	66
4.1	<b>(A)</b> Stack renaming and <b>(B)</b> respective datamatrix organization	74
4.2	<b>(A)</b> An example of Purkinje neuron segmented with the SmRG algorithm, <b>(B)</b> its skeleton and <b>(C)</b> a merge of the two.	76
4.3	An example of a Purkinje cell circumscribed by the coordinate spheric system, centered on the soma.	77
4.4	Minimum length vectors for a Purkinje cell.	79
4.5	Radial extension of a Purkinje cell.	80
5.1	<b>(A)</b> Low magnification view of a para-sagittal cryosection of the vermis of a WT male mouse. The piriform layer consisting of the aligned somata of the PCs is clearly visible. Note that the GFP tag is distributed in the entire cytoplasm of the PCs so that their extensive dendritic arborizations appear as an overall diffuse fluorescence of the molecular layer and the axons can easily be seen travelling across the white matter to reach the fastigial nucleus at the basis of cerebellum. The five lobules considered in this study are indicated by their descriptive names and corresponding roman numerals. Abbreviation: CE = lobulus centralis; CU = culmen; NO = nodulus; TU = tuber vermis; UV = uvula; PNs = Purkinje neurons; ANT = anterior; POS = posterior. <b>(B)</b> Diagram showing the 3D planes of the mouse cerebellum. Parasagittal sections are cut along the YZ plane (green). The fluorescent somata of the PNs (yellow ovals) are aligned along a curved dashed line. Displacement of the PNs along the YZ plane (green) is exemplified by the somata that lie above or below the black dashed line of the piriform layer.	103



5.2 Main steps in the NEMO work-flow used to calculate the dispersion of PCs along the YZ cerebellar plane. **(A)** The effect of image thresholding to separate the fluorescent white pixels from the black background. Thresholding was necessary to eliminate the fluorescent dendritic arbores in the molecular layer. In the example, fluorescent Purkinje axons are still visible in the granular layer. **(B)** Purkinje somata detected by the Hough transform **(C)** Plot of X and Y coordinates of five Purkinje somata (blue circles) and the linear fitting line (red) calculated by NEMO. 105

5.3 **(A)** Frequency distribution histogram of the size of PCs after exclusion of the 2D objects smaller than  $9 \mu\text{m}$  and larger than  $\mu\text{m}$ . Soma size follows a normal distribution. **(B)** 2-way ANOVA shows that  $\text{reln}+/-$  males have larger PC areas than the female genotypes. . . . . 107

5.4 2-way ANOVA with multiple comparison test shows statistically significant differences in the mean RMSE (that measures PC misalignment along the YZ cerebellar axis) between  $\text{reln}+/-$  males and  $\text{reln}+/-$  females in four of the five cerebellar lobules examined in this study (with the exception of the lobulus centralis) and between  $\text{reln}+/-$  and WT males in all lobules considered (\*\* $\text{P} = 0.001$ ; \*\*\*\* $\text{P} < 0.001$ ). Error bars in graphs indicate SD. Abbreviation: CE = lobulus centralis; CU = culmen; NO = nodulus; TU = tuber vermis; UV = uvula; PNs = Purkinje neurons; F = female; M = male; RMSE = root mean squared error of linear fit. . . . . 108

5.5 Interpolation of the number of intersections as a function of radius for an typical PC from **(A)** a L7GFP/WT male mice, **(B)** a L7GFP/WT female mice, **(C)** a L7GFP/En2 +/- male mice and **(D)** a L7GFP/En2 -/- female mice. . . . . 113

5.6 2-way ANOVA for repeated measures with multiple comparison test shows statistically significant differences in the mean values of the Schoenen Coefficient between WT and En2 -/- mice for both males and females. Error bars in graphs indicate SD. ( $\text{p} < 0.001$ ) . . . . . 113

5.7 2-way ANOVA for repeated measures with multiple comparison test shows statistically significant differences in the mean values of the Sholl regression coefficient between the four groups analysed. Error bars in graphs indicate SD. ( $\text{p} < 0.001$ ). . . . . 114

5.8 2-way ANOVA for repeated measures with multiple comparison test shows statistically significant differences in the mean values of the Soma Volume between males and females for both WT and En2 -/- mice. Error bars in graphs indicate SD. (p<0.001) . . . . . 115

5.9 2-way ANOVA for repeated measures with multiple comparison test shows statistically significant differences in the mean values of the Surface-Area-to-Volume ratio between WT and En2 -/- mice for both males and females. Error bars in graphs indicate SD. (p<0.001) . . . . . 116

5.10 2-way ANOVA for repeated measures with multiple comparison test shows statistically significant differences in the mean values of the Number of Branches between WT and En2 -/- mice for both males and females. Error bars in graphs indicate SD. (p<0.001) . . . . . 117

5.11 2-way ANOVA for repeated measures with multiple comparison test shows statistically significant differences in the mean values of the Fractal Dimension, measured using the box-counting method, between WT and En2 -/- mice for both males and females. Error bars in graphs indicate SD. (p<0.001) . . . . . 118

5.12 2-way ANOVA for repeated measures with multiple comparison test shows statistically significant differences in the mean values of the Radial Extension between WT and En2 -/- mice for both males and females. Error bars in graphs indicate SD. (p<0.001) . . . . . 119

6.1 Microphotographs of immunohistochemical and histological staining of coronal brain sections. **(A)** Low magnification image (left side) of the anti-parvalbumin antibody distribution in the left hemisphere including the claustrum; schematic draw (right side) with charting representing the distribution of the PV labeled somata (red dots) in the claustrum. Scalebar: 1 mm. **(B)** Low magnification image of a Luxol Fast Blue (left side) and Nissl (right side) stained sections. Scalebar: 1 mm **(C)** Detail of A and **(D)** detail of C showing anti-parvalbumin labelled neurons in the ventral claustrum. Scale bars: C = 10 mm and D = 20 mm. . . . . 134

6.2 Silhouette plot showing how soma size and shape form 2 unique and tightly grouped clusters with very few outliers. Within each cluster, the high silhouette values suggest that the objects are well-matched . . . . . 136

6.3 Volume view of a confocal stack representing calretinin positive components (Em/Ex: 568/603 pixel-to-micron ratio size: 2.46  $\mu\text{m}$  , z-resolution: 5  $\mu\text{m}$ ). Volume dimensions (w\*h): 1259\*1259\*196  $\mu\text{m}$ . . . . . 141

6.4	Two examples of parvalbumin-immunoreactive interneuron traced with the SmRG algorithm. . . . .	143
6.5	Number of publications by year on the claustrum (according to PUBMED <a href="http://www.ncbi.nlm.nih.gov/pubmed">http://www.ncbi.nlm.nih.gov/pubmed</a> ) . . . . .	146



# List of Tables

1.1	State of Art of the principal tissue clarification methods, with their pros and cons. . . . .	6
3.1	Confocal Acquisition settings for 1-mm thick cerebellar slices from L7GFP mice . . . . .	55
3.2	Comparative Sholl analysis (with constant number of spheres) for a Purkinje cell segmented with the SmRG algorithm and through manual tracing performed by an expert . . . . .	58
4.1	Tools and functions implemented in N3MO. . . . .	71
4.2	Comparative Sholl analysis usign N3MO and the ImageJ plug-in [3] . .	85
4.3	Characteristics of the principal software for neuron morphological analysis	87
5.1	Comparison of features extracted from PCs for the four groups analysed, classified in gender- and genotype related. . . . .	121
6.1	Confocal acquisition settings for 500 $\mu$ m thick claustrum slices, immunostained with anti-calretinin and anti-parvalbumin antibodies. . . . .	140



# Chapter 1

## Introduction

*“As humans, we can identify galaxies light years away, we can study particles smaller than an atom. But we still haven’t unlocked the mystery of the three pounds of matter that sits between our ears. [...] As a result, we are still unable to cure diseases like Alzheimer’s or Autism, or fully reverse the effects of a stroke”.*

(Barack Obama announcing BRAIN project, April 2, 2013).

According to A. Paul Alivisatos, member of the Berkeley University and partner of the BRAIN (Brain Research through Advancing Innovative Neurotechnologies) project, understanding how the brain works is arguably one of the greatest scientific challenges of our time. Although there have been piecemeal efforts to explain how different brain regions operate, no general theory of brain function is universally accepted [4]. A fundamental underlying limitation is our ignorance of the brain microcircuitry, which is translated in the difficulty of deeply exploring the function of complex neural circuits: this is an invaluable step towards under-

standing fundamental and pathological brain processes. In fact, since the role of cell structure in regulating cell behaviour and tissue function is well known, investigating the relationship between brain micro-structure and high-level function is a central endeavour for neuroscience research. Yet, the mechanisms shaping this correspondence largely remain to be elucidated and are highly debated [5, 6]. The neuroscience community feels the need for a precise understanding of brain structure, that could help in different fields of research. In particular, new approaches to reconstruct neurons and circuits from empirical data can aid neuro-anatomical mapping, as well as generating models that can be used to make predictions about a higher-level organization where knowledge is poor [7]. Detailed morphological analyses of neurons are also vital for studying the normal development of dendritic and axonal arbours and for documenting neuro-pathological changes. Neurite arborization patterns established during development are characteristic for particular neuronal subtypes and relate to function. Neurite arbour size and shape influence the integration of synaptic inputs [8] and these, in turn, are regulated by both intrinsic developmental programs and external signals [9, 10]. Alterations in neurite arbours have been observed in a number of neuro-pathological conditions including mental retardation syndromes such as Autism Spectrum Disorders [11] and Alzheimers disease [12].

The main roadblocks to a more profound understanding of micro-structure and corresponding function are: i) the lack of standardization and optimization of protocols and procedures, ii) the presence of lipids in brain tissue, that causes scattering and limits the depth of light penetration and iii) the lack of algorithms for single-neuron tracing and morphometric extraction from three-dimensional image datasets.

As regards the first point, there is a huge amount of variability across laboratories in every step of the scientific process. Data is collected with



different brands of equipment and protocols, and the lack of automated algorithms to trace neurons and extract quantitative morphometric leads neuroscientists to manually quantify neuronal morphology, obtaining results prone to human bias [13]. Ignorance of basic methodological principles leads to poorly designed research and misleading conclusions. It undermines the whole point of scientific investigation. All these factors make the notion of any laboratory exactly replicating another' results quite difficult. In addition, the neuroscience literature is often conflicting and does not support the received wisdom because of the dearth of statistical power of many studies, as highlighted by a recent analysis of scientific studies in neuroscience [14].

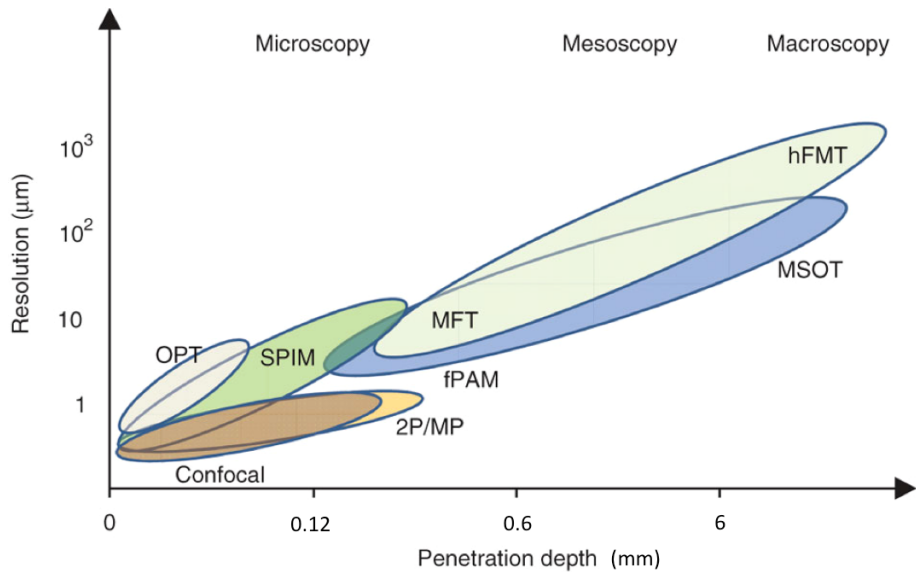
Regarding the second point, the light microscope has long been one of neuroscientists' cardinal tool for studies of cellular morphology and brain cyto-architecture [15]. The imaging limits of conventional microscopy (i.e. scattering and light attenuation) made biological imaging myopic for centuries: for these reasons, traditional 10-20  $\mu\text{m}$  - thickness of tissue slices used for microscopy ensures that only a small fraction of photons are scattered, resulting in high image quality and diffraction-limited resolution, but limiting the understanding of real neuron arrangement within the brain [2]. Ongoing advances have enabled new experimental capabilities using light to inspect systems across multiple spatial scales. Resolution and penetration depth are two important parameters to characterize the performance of the most advanced optical imaging devices. Unfortunately, as shown in Figure 1.1, there are no methods performing high-resolution imaging with high depth penetration. In order to investigate cell morphology, confocal and multi-photon microscopy are the best candidates to image thicker specimens. These methods have revolutionized biological discovery by allowing the non-invasive study of micro-structure because high-resolution images can be formed at depth

of tens to hundreds of micrometers [2].

Although optical imaging is rapidly increasing its performance, providing the high spatial resolution necessary to resolve individual neurons and neuronal processes, acquiring images through significant depths of the brain is no easy task since tissue is extremely heterogeneous. Moreover, the presence of lipids results in strong scattering, which limits the depth of light penetration and constitutes an antibody-impermeable barrier. The traditional approach to image the brain is based on serial mechanical sections of the tissue, but the process is costly, laborious, involves deformation of tissue and bits of tissue can get lost (Figure 1.2).

For this reason, different optical clearing methods have been developed: because scattering occurs when the refractive index of the sample differs from the medium, one approach is to reduce variations of refractive index and light scattering by exchanging the water in the sample with organic solvents or aqueous solutions with the same refractive index as membrane lipids, so that lipids become essentially transparent. Methods based on this principle are: 3DISCO method [16], Scale method [17], ClearT method [18] and SeeDB method [19], summarized in Table 1.1.

However, these clearing techniques are not compatible with molecular phenotyping: only photons can penetrate deep into tissue, while labelled biomolecules, essential for molecular phenotyping, cannot pass through the brain. To overcome this limit, a different approach was developed in 2013, the CLARITY method [20, 21], in which the brain is modified so that it becomes permeable both to macromolecules and photons. In particular, CLARITY enables the transformation of intact biological tissues into an hybrid form in which lipids are removed through solubilization with a ionic detergent (Table 1.1). A simplified diffusion based method, CLARITY2 [22], was successively proposed to clarify 1-1.5 mm thick brain slices: this approach is very useful when there is the need

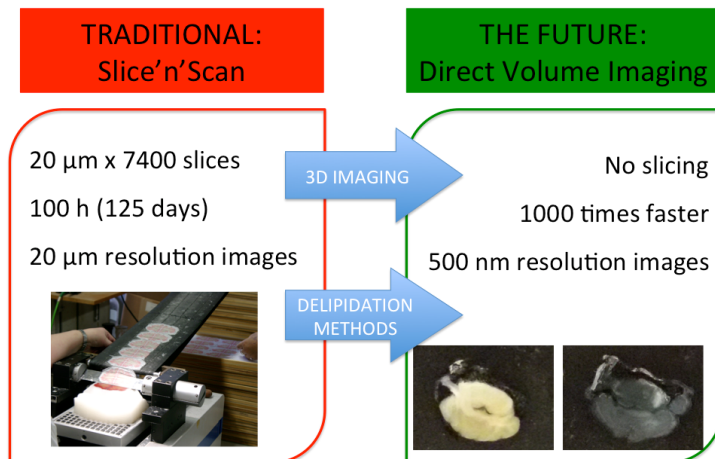


*Figure 1.1: The penetration depth and resolution of modern imaging techniques for brain tissues. The methods on the left are primarily limited by light scattering, whereas methods to the right are limited by light attenuation in tissue, a parameter that depends on both absorption and scattering. Abbreviations: OPT: Optical Projection Tomography, 2P/MP: two-photons/multi-photons, fPAM: functional Photo-Acoustic Microscopy, hFMT: hybrid Fluorescence Molecular Tomography, MSOT: Multi-Spectral Opto-acoustic Tomography, SPIM: Selective Plane Illumination Microscopy, MFT: Mesoscopic Fluorescence Tomography. [2]*

*Table 1.1: State of Art of the principal tissue clarification methods, with their pros and cons.*

Optical Clearing	Advantages	Disadvantages	Imaging techniques available
<b>3DISCO</b> [16] Demonstrated in whole adult mouse, brain and spinal cord segments	<ol style="list-style-type: none"> <li>1. Low duration (2-5 day for clearing a whole adult mouse brain)</li> <li>2. Highly reproducible method</li> <li>3. No tissue expansion</li> <li>4. Versatility (it is applicable on a variety of biological samples including central nervous system organs, immune organs and solid tumors)</li> <li>5. Method compatible with many labeling methods (fluorophores, synthetic dyes and antibody labeling)</li> </ol>	<ol style="list-style-type: none"> <li>1. Changes in chemical nature of the tissue are registered</li> <li>2. Method not compatible with prolonged imaging due to the use of organic solvents, which rapidly quench most fluorescent protein signals</li> <li>3. Because of limited antibody penetration, immunolabeling of large tissue is difficult</li> <li>4. Method incompatible with whole-tissue molecular phenotyping</li> <li>5. Not reversible</li> <li>6. Because optical clearing damages the lipids structures, electron microscopy cannot be used</li> </ol>	<p>Cleared tissue can be imaged using light-sheet laser-scanning ultramicroscope (that costs about half the price of a confocal microscope), two-photon microscopy or confocal microscopy. However, the maximum imaging area and depth of the last two techniques are small if compared with light-sheet microscopy: 0.5-1 mm, versus 10-20mm and 0.2-2.2 versus 10-20 mm respectively.</p>
<b>SCALE</b> [17] Demonstrated in whole young mouse brain, although myelin-rich white matter not completely clear	<ol style="list-style-type: none"> <li>1. Reagent formula is public and easy and inexpensive; researchers can modify its composition according to the nature of the sample that have to be cleared</li> <li>2. Fluorescent signals are preserved</li> </ol>	<ol style="list-style-type: none"> <li>1. Large expansion in tissue volume</li> <li>2. Because of partial denaturation and loss of proteins by urea, samples are soft and fragile</li> <li>3. Method not compatible with lipophilic dyes</li> <li>4. Method not fully reversible because of protein denaturation and tissue deformation</li> <li>5. Myelin-rich brain regions remain opaque</li> <li>6. Long time periods required for clearance (3 weeks for clearing a whole adult mouse brain)</li> <li>7. Changes in chemical nature of the samples are registered</li> <li>8. Method incompatible with whole-tissue molecular phenotyping</li> </ol>	<p>Cleared tissue can be imaged using one- or two-photon microscopy, that allow to achieve a depth of 2 mm. In deep regions, two-photon microscopy shows a better signal-to-noise ratio.</p>
<b>ClearT</b> [18] Demonstrated in whole young mouse brain and in sections from adult mouse brain	<ol style="list-style-type: none"> <li>1. No or mild tissue expansion</li> <li>2. Compatible with lipophilic dye tracing</li> <li>3. Short time incubation (1 day) for clearing an intact mouse embryo (no data available for adult mouse brain)</li> </ol>	<ol style="list-style-type: none"> <li>1. Not compatible with fluorescent proteins</li> <li>2. Formamide is unsuitable for long-term tissue storage</li> <li>3. Method incompatible with whole-tissue molecular phenotyping</li> </ol>	<p>Cleared tissue can be imaged using stereomicroscope or dissecting microscope.</p>

SeeDB [19]	Demonstrated in whole young mouse brain but reported to be difficult in adult mouse	<ol style="list-style-type: none"> <li>1. No tissue expansion</li> <li>2. No fluorescent proteins and lipophilic neuronal tracers quenching observed</li> <li>3. Reversible with PBS multiple times</li> <li>4. Short time incubation for clearing (3 days for immature brain); clearing adult brain reportedly difficult</li> <li>5. No changes in chemical nature of the samples</li> <li>6. It can be combined with immunohistochemistry without loss of antigenicity</li> <li>7. Minimum reagents and efforts required</li> <li>8. Both gray and white matter can be cleared</li> <li>9. Easy and inexpensive method, no special equipment required</li> </ol>	<ol style="list-style-type: none"> <li>1. Clearing of large pieces of tissue such as whole adult mice brain is difficult without sample incubation at high temperature, that causes some fluorescent loss</li> <li>2. Limited penetration of antibodies that can only penetrate a depth of 100-250 <math>\mu\text{m}</math></li> <li>3. Limited penetration of chemical dyes for counterstaining</li> <li>4. Method incompatible with whole-tissue molecular phenotyping</li> </ol>	It is possible to reach >1,000 $\mu\text{m}$ depth with confocal microscopy and to image fixed mouse brain samples at mm-scale level with two-photon microscopy
CLARITY [20]	Demonstrated in whole adult mouse brain, adult zebrafish brain and postmortem human brain tissue	<ol style="list-style-type: none"> <li>1. No fluorophore quenching observed</li> <li>2. Reversible tissue expansion during the process</li> <li>3. Lipids are completely removed without mechanical disassembly the tissue</li> <li>4. Multiple rounds of molecular phenotyping are allowed</li> <li>5. Method compatible with immunostaining</li> <li>6. Versatility</li> </ol>	<ol style="list-style-type: none"> <li>1. Method not compatible with lipophilic dyes</li> <li>2. Not reversible</li> <li>3. Change in chemical nature of the samples are registered</li> <li>4. Technically difficult: method involves custom set-up assembly and many experimental steps with a lot of variables to be controlled</li> <li>5. High start-up and consumable material costs</li> <li>6. Immunostaining is time-consuming</li> <li>7. Long time periods required for clearance (2 weeks)</li> </ol>	Confocal microscopy, by exposing the tissue to excitation light, causes photobleaching of fluorescent molecules. With two-photon microscopy, it is possible to overcome this limit but both single and two-photon imaging techniques are characterized by low image acquisition rate. For imaging large samples at high resolution and high image acquisition rate, selective-plane illumination microscopy is the most effective choice.



*Figure 1.2: From traditional brain imaging to direct volume imaging, thanks to the advance in optical microscopy and delipidation methods.*

to focus the study only on a brain sub-region or on a specific neuronal population. But, like CLARITY, the CLARITY2 also protocol involves numerous variables and tissue transparency is evaluated heuristically: every laboratory has its own protocol, and there is no unique way to define the “goodness” of clarification, leaving much to trial and error.

Even after the clarification steps, three-dimensional confocal datasets representing dense packed neurons within the brains are far from being easily processed. In fact, the intensity values within a confocal image stack vary discontinuously, because of both attenuation/scattering of light and non uniform distribution of the fluorescent signal due to biological heterogeneity. In order to overcome these problems, different algorithms have been developed to trace single-neurons from three-dimensional datasets, using different approaches: segmentation with a

global threshold [23, 24], region growing with active contour techniques [25, 26, 27, 28], fuzzy schemes [29] or 3D wavelet transform [30]. In addition, methods based on prior knowledge (i.e. user aided segmentation [31], atlas-based segmentation [32] or tool partially mimicking human strategies to separate individual neurons [33]) were also presented in the literature, but they are strongly user-dependent. Unfortunately, none of the mentioned algorithms are able to handle stacks with intensity inhomogeneity and noise of spatially varying strength, leaving the challenge still unsolved. Currently, great efforts are being made to address this problem, e.g. BigNeuronLaunch project by Allen Institute for Brain Science) aiming to both standardize the method and mobilize the reconstruction community to generate interest in solving these complex and interesting algorithm problems. In particular, the neuro-informatics community agrees that consider region growing schemes based on histogram local characteristics are a robust approach to segmentation, but in the State of Art only models with local image intensities described by local Gaussian distributions are presented. However, confocal datasets cannot always be described with a set of local Gaussian distributions [34].

An other aspect which needs addressing regards morphometric analysis: most of the tools implemented are dedicated to 2D images [35, 36, 37, 38, 39], so they are developed for *in-vitro* cultured neurons, that cannot represent the real neuron shape within the brain. In addition, although different tools have been developed for morphological analysis [1, 40, 31, 41, 42], it is still not possible to perform a complete analysis using a unique software to consistently quantify neuronal micro-architecture through image processing.

In this context, the aim of this PhD thesis was to develop an innovative and rigorous work-flow for quantitative analysis of brain micro-architecture, that integrates delipidation protocol optimization and imag-

ing algorithms to trace single neurons and to extract morphological parameters of interest from confocal datasets. The work-flow is shown in Figure 1.3.

Subsequently, some or all elements of the workflow were applied to the study of sexual dimorphism in animal models of autism and to investigate the micro-structure of the claustrum.

This PhD thesis is subdivided into five main Chapters.

In Chapter 2, a standardization of the CLARITY2 method is described, to determine the optimum clearing time. In particular, as the main objective of the delipidation treatment is to clarify tissues while limiting loss of proteins linked to specific cell populations (e.g. Tubulin III for neurons in the Central Nervous System of mammals), the goodness of clarification was evaluated by considering the bulk tissue clarification index (BTCi) and the fraction of proteins retained in the slice as easily quantifiable macro-scale parameters. For un-perfusible samples (e.g. from autaptic brains), slice thickness was considered as a further parameter to optimize, since the hydrogel achieves the whole sample only through passive diffusion, limiting the protocol efficacy.

In Chapter 3, to tackle the difficulties of automatically tracing neuronal structures in their native three-dimensional arrangement within the brain, a Smart Region Growing (SmRG) algorithm was developed to trace single neurons from confocal stacks, based on local features of the image intensity value histogram.

The SmRG algorithm was then integrated in the N3MO tool, purposely developed for this thesis and detailed in Chapter 4. N3MO was designed to handle and process confocal stacks representing brain areas with neurons in their own three-dimensional arrangement, in order to automatically run routines to extract the morphometric variables, store the data obtained and classify them using multivariate analysis.



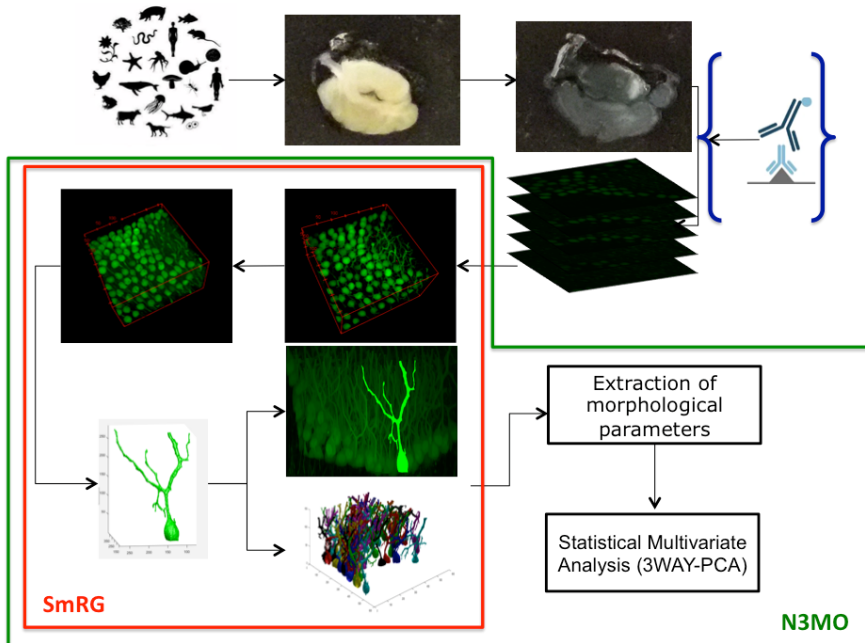


Figure 1.3: The work-flow designed for the study of brain micro-architecture. After brain tissue clarification, standardized and optimized as detailed in Chapter 2, and, if needed, an immuno-labelling procedure to highlight structures of interest (i.e. Tubulin III antibody to label all mammalian neurons), three-dimensional datasets were obtained using a confocal microscope. The stacks were then processed with the SmRG algorithm, described in Chapter 3, for single neuron tracing. Then, each three-dimensional structure obtained was analysed with N3MO, whose features are described in Chapter 4, to extract morphometric variables and store the data obtained; if needed, data can be also analysed using statistical multivariate analysis (i.e. 3-way PCA)

Finally, the work-flow was applied to two case studies.

Firstly, as described in Chapter 5, a study of sexual dimorphism in animal models of autism through the analysis of morphological differences in Purkinje cells (PCs) is presented, because they are known to play an important role in the development of the disorder [36, 43, 44, 45]. Moreover, because of the unbalanced incidence of Autism Spectrum Disorders between males and females (i.e. 4:1 ratio) and the lack of studies in the State of Art proofing any sexual dimorphisms in ASDs at the microstructural level, for each genotype both sexed mice are considered. A proof of concept on 2D images processed with NeMo [36], representing Purkinje cells in thin cerebellum slices, demonstrates that there are statistically relevant morphological differences between wild-type mice and knock-out ones, taking also into account sexual dimorphism. However, since two-dimensional studies cannot give information about the native arrangement of the neurons within the brain, the method designed in this thesis was applied to study morphological alterations in PCs in thick cerebellum slices from males and females wild-type and knock-out mice. The second part of this thesis is dedicated to the study of claustrum micro-architecture. The structure and function of the human claustrum are still a matter of intense debate and investigation [46, 47], but a characterization of the distribution of neurons in their three-dimensional context within this nucleus is still lacking. In fact, few studies about human claustral cells were performed. In particular, Braak et al, (1982) [48], using Golgi-technique on thin slices classified neural claustral cells. However, the study was just based on visual inspection and no quantitative classification based on morphometrics is performed. Moreover, since the Golgi technique randomly stains the neurons inside the nucleus, it just allows the neuronal identification, but not the measure of the cell density. A more recent study, conducted by Hinova-Palova (2013) [49], also aimed

to classify different neuron types demonstrating the presence of an opioid peptide involved in autonomic and neuroendocrine regulation. To this end, in Chapter 6, a preliminary study was performed on 2D histological micrographies of dog claustrum, to classify different neuron types with respect to their shape. Since the results obtained demonstrate that neuron shape can be used to distinguish between different neuron types, and given the advantages of 3D versus 2D, some elements of the work-flow presented in Figure 1.3 were applied to human claustrum. In particular, after the clarification step on thick slices using the optimal parameters identified in the work-flow, a three-dimensional neuron reconstruction was acquired with a confocal microscope. These datasets could represent a first step towards the pursuit of the knowledge of structure-function relationship in this enigmatic nucleus.



# Chapter 2

## Clarifying CLARITY: quantitative optimization of the diffusion-based delipidation protocol

*"The brain micro-circuitry is an impenetrable jungle where many investigators have lost themselves."*

*(Ramon y Cajal)*

### **Abstract**

*Tissue clarification has been recently proposed to allow deep tissue imaging without light scattering. The clarification parameters are somewhat arbitrary and dependent on tissue type, source and dimension: every laboratory has its own protocol, but a quantitative approach to determine the optimum clearing time is still lacking.*

*Moreover, most of the clarification methods are designed for small and perfusable animals (i.e. mice or rats) to achieve all tissue regions through*

blood micro-vessels and enhance protocol efficacy. On the other hand, the study of large animal brains or parts of them (i.e. human claustrum), essential for investigating unknown structures, is limited by passive diffusion of the delipidation reagents in each clarification step, and so it is slice thickness-dependent.

In this context, a quantitative approach using CLARITY2 is described, to determine the optimum clearing time and, for un-perfusable tissues, also the optimum slice thickness. In particular, as the main objective of the delipidation treatment is to clarify tissues, while limiting loss of proteins linked to specific cell populations (e.g. Tubulin III for neurons in the Central Nervous System of mammals) the goodness of clarification was evaluated by considering the bulk tissue clarification index (BTCi) and the fraction of proteins retained in the slice as easily quantifiable macroscale parameters. For un-perfusable samples, slice thickness was considered as a further parameter to optimize.

Here we describe the approach, illustrating three examples of how it can be used to determine the optimum clearing time for i) cerebellar slices from transgenic L7GFP mice, in which Purkinje neurons express the GFP (green fluorescent protein) tag, ii) un-labelled cerebellar slices from CD1 mice and iii) un-labelled and un-perfused slices from human samples. To validate the method, for the transgenic brains we evaluated confocal stacks of our samples using standard image processing indices (i.e. the mean pixel intensity of neurons and the contrast-to-noise ratio) as figures of merit for image quality.

The results show that, while detergent-based delipidation reaches a tissue- and thickness-dependent plateau in time, the fraction of protein in the tissue continues to diminish. The optimum clearing time can be determined as the best compromise between the increase in light penetration depth due to removal of lipids and a decrease in signal as a consequence of protein

*loss: further clearing does not improve tissue transparency, but only leads to more protein removal or degradation.*

*The rigorous quantitative approach described can be generalized to any clarification method to identify the moment when the clearing process should be terminated to avoid useless protein loss.*

## **2.1 From brain tissue to confocal acquisition: tissue clearing protocol standardization and optimization**

One of the challenges of modern neuroscience is to map the architecture of neural circuits in the mammalian brain, in order to delineate the so-called Connectome [50], tracing the information pathways through axons and dendrites of neurons in their native three-dimensional (3D) arrangement. The main obstacle for this kind of study is the presence of lipids, which cause light scattering, limit the depth of light penetration, and constitute an antibody-impermeable barrier. Even using two-photon microscopy, it is impossible to penetrate brain samples more than a few hundred microns [51], which is insufficient for reconstructing large brain projections or complete neural populations [20].

To overcome these limits, a number of optical clearing or delipidation approaches have been developed to render the whole brain transparent so that it can be analysed without sectioning [16, 17, 19, 18, 52]. Among these, the CLARITY method, pioneered and disseminated through forums and Wiki pages by Deisseroth's group (i.e. <http://forum.claritytechniques.org/>), has captured the imagination of many researchers and is currently discussed and debated widely [20, 21, 53]. To date about 20 new papers on CLARITY and its variations have been published and a number of them are dedicated to the optimisation or simplification of

the experimental set up [54, 55, 56, 57]. In fact, despite the plethora of virtual discussion groups, the method remains substantially heuristic due to the large number of steps involved and the ensemble of variables which contribute to the tissue delipidation process. For instance, tissue clearing is evaluated by visible inspection and is thus prone to observer bias. Furthermore, the mechanisms of tissue fixing and clarification remain elusive, making it almost impossible to standardize CLARITY for rigorous quantitative studies.

After Chung et al.'s seminal report [21], a simplified diffusion based method, CLARITY2, was proposed by Poguzhelskaya et al. [22] to clarify 1-1.5 mm-thick slices. CLARITY2 does not necessitate the use of the electrophoretic chamber, probably the most time consuming and difficult step of the whole procedure. The passive clarity technique (PACT) is very similar to CLARITY2 [58]. Both approaches can be very useful when it is not necessary to achieve the full potential of CLARITY to delipidate an intact brain, focusing the study only on a brain sub-region or on a specific neuronal population (i.e. Purkinje cells in the cerebellar layers). Like the CLARITY protocol, CLARITY2 involves protein and structural fixation through the use of formaldehyde and an acrylamide based gel, transcardially perfused into anesthetized animals, followed by solubilisation of lipids using sodium dodecyl sulphate (SDS) in the so-called clearing solution.

However, despite their excellent contribution to brain imaging, even passive clearing methods presents some problems:

1. CLARITY2 is designed for small and perfusable animals. No tips were given to the users in Chung's article to modify the protocol for un-perfusable tissue, such as human brain samples. In the State of Art, Liu et al. (2015) [59] customized the protocol for un-perfusable tissue, but an optimization of the parameters is still lacking;



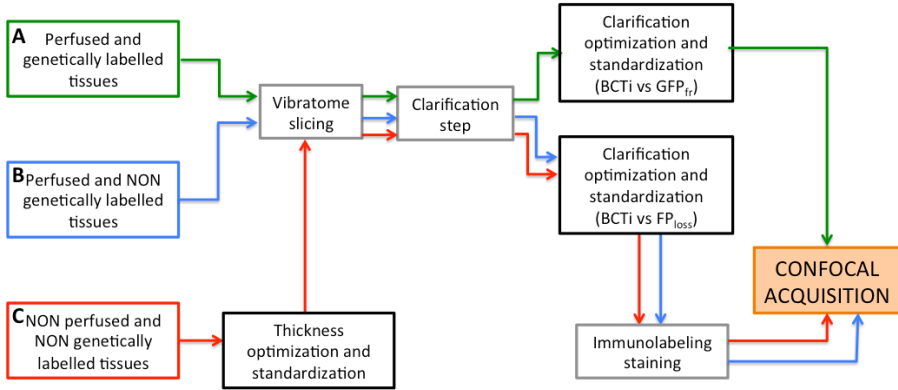


Figure 2.1: Schematic work-flow with the standardization procedures established, from tissue harvesting to confocal acquisition, for **A** perfused and genetically labelled tissues (green path), **B** perfused and non genetically-labelled tissue (blue path) and **C** non perfused and non-genetically labelled tissues (red path).

2. CLARITY2 combines a large number of variables (i.e. slice thickness, reagent concentration, clearing times), leaving much to trial and error;

To address these issues, an experimental method was developed for the optimization and standardization of the clarification protocol. The method designed involves two main steps, summarized in Figure 2.1:

- **Slice thickness optimization and standardization** Since vessels cannot be used to achieve the systemic delivery of hydrogel and the clarification reagents in all the regions of the sample, it is necessary to find a trade-off between tissue thickness and protocol efficacy in case of un-perfusible tissues;
- **Clearing time optimization and standardization.** The removal of tissue lipids reduces tissue opacity, but is inevitably ac-

accompanied by a non-specific loss of inter- and extra-cellular components.

In this context, clarification for imaging the 3D cellular architecture can be regarded as a trade-off between the increase in light penetration depth due to delipidation and a decrease in emission signal as a consequence of protein loss through solubilisation or degradation. Here an approach is defined to macroscopically assess the delipidation efficacy as a function of clearing time. In case of genetically labelled tissue, to double-check the experimental method and validate it, the results were compared with those obtained with indexes usually used in image processing.

## 2.2 Optimization method for perfused and genetically labelled tissues

### 2.2.1 Materials and Methods

**Tissue preparation.** Both CD1 and L7GFP mice were obtained from the Department of Translational Research, New Technologies in Medicine and Surgery of the University of Pisa (Italy). While CD1 mouse brains are not genetically-labelled, in L7GFP ones GFP (green fluorescent protein) expression is driven by the Pcp-2 promoter and is specific for Purkinje cells (PCs) in the cerebellar layers [60]. The experiments were conducted in conformity with the European Communities Council Directive of 24 November 1986 (86/609/EEC and 2010/63/UE) and in agreement with the Italian DM26/14. Experiments were approved by the Italian Ministry of Health and Ethical Committee of the University of Pisa.

Adult mice were anaesthetised with a lethal dose of 7% chloral hydrate and then perfused at a slow flow rate (about 2 minutes for 20 mL of solution) with 20 mL of ice cold Phosphate Buffered Saline (PBS 1X,

Sigma-Aldrich, Milan, Italy) and then 20 mL of ice cold hydrogel solution, containing 4% acrylamide, 0.05% bis-acrylamide (Biorad Lab Inc., California, USA), 4% formaldehyde (PFA, Sigma-Aldrich) and 0.25 % VA-044 thermally triggered initiator (Wako Chemicals, Neuss, Germany) at 4 ° C, as described in Chung et al., 2013 [21].

The brain was immediately extracted and submerged in 20 mL hydrogel solution for 3 days at 4° C in a 50 mL Falcon tube (for L7GFP brains, the tube was covered with aluminium foil to protect samples from direct light exposure) to allow gel diffusion into the tissue. Then the cap was substituted with a modified one with a small hole to which a short piece of silicone tube with an on-off valve was hot-glued. A vacuum was applied to the tube for 10 minutes, after which the valve was closed to enable hydrogel formation in the absence of air (the presence of oxygen impedes gelation of the acrylamide gel). Polymerization of the biomolecule-conjugated monomers in the hydrogel mesh was thermally initiated by incubating the infused tissue overnight at 37° C.

The mouse brain was then isolated by carefully removing the surrounding excess hydrogel, and vertically cut along to the coronal plane with a scalpel to obtain the portion containing the cerebellum.

At this point, in order to establish the most suitable slicing set up for the brains, the effect of two sectioning parameters (i.e. step size and sectioning speed) on resultant slice thickness were investigated, while keeping the oscillation amplitude, 1.5 mm and the blade angle, 18 °, constant, as they are less crucial to the determination of slice thickness.

Given that slicing accuracy is stiffness-dependent (i.e. the more stiff the tissue, the more matching exist between experimental slice thickness and vibratome step size) and that the stiffness of biological tissues is known to increase after fixation through 4% PFA intra-cardiac perfusion, it is reasonable to consider hydrogel-embedded tissue mechanically compara-

ble with those PFA-fixed used to characterize vibratome slicing setup in Mattei et al., (2015) [61]. Taking into account this assumption, mouse cerebella were cut into 1 mm-thick coronal slices using a Leica VT1200S vibratome (Leica Microsystems, Nussloch, Germany) with a stainless steel razor blade (Gillette, Milan, Italy). The cut settings were: blade angle, 18°; sectioning speed, 0.2 mm/s; and oscillating amplitude, 1.5 mm.

**Clarification steps.** Each hydrogel-embedded slice was placed in a 50 mL Falcon tube at 37° C with 10 mL of CLARITY clearing solution, composed of 200 mM Boric Acid (Farmitalia Carlo Erba spa, Italy) and 4 % Sodium Dodecyl Sulphate (SDS, Sigma-Aldrich) [21]. The pH was adjusted to 8.5 by adding 1 M NaOH dropwise.

Cerebellar slices embedded in the hydrogel and immersed in 20 mL of 1X PBS solution were used as controls. Clearing solutions and PBS in the controls were changed at 3, 5 and 7 days.

**Quantitative evaluation of clarification.** At each time point investigated (i.e. day 0-3-5-7-10), the goodness of clarification for both the treated tissue slices and controls was evaluated using two macroscopic approaches: i) a quantification of tissue clarification through image analysis, and ii) an evaluation of the fraction of the GFP lost in the clearing solution.

**Bulk Tissue Clarification Index.** Tissue slices were placed on a white plastic support marked with a black line and photographed using a Nikon D5100 reflex camera (Figure 2.2).

After converting the images into 8-bit grayscale, the clarification was evaluated defining a Bulk Tissue Clarification index (BTC<sub>i</sub>) as:

$$BTC_i = \frac{255 - I_1}{255 - I_s} \quad (2.1)$$

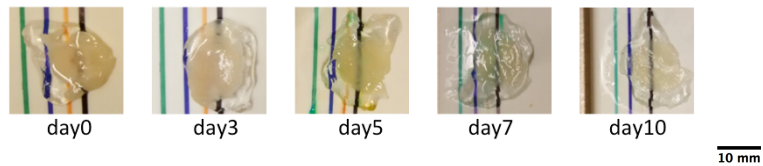


Figure 2.2: Photographs of cerebellar slices at different clearing times. The images were used to calculate  $BTC_i$  through equation 2.1, comparing the intensity of the black line below the slice and in the region without the slice. (pixel size: 0.125 mm)

where  $I_1$  and  $I_s$  are the mean pixel intensities of the black line traced on the support respectively with and without the tissue on it. Averaging the pixel intensities reduces local variations, while the term  $I_s$  in equation 2.1 serves as an internal normalization which eliminates variations due to any differences in environmental light conditions between images. The index so-defined ranges from 0 (i.e. totally opaque white slice) to 1 (i.e. totally transparent slice).

**Quantification of the fluorescent protein loss.** In principle, there are two sources of tissue protein loss: protein denaturation due to the clearing solution and protein release into in the clearing solution. In case of genetically-labelled tissues, since the clearing solution (pH 8.5, containing SDS) is not likely to denature biological fluorophores [62], the loss of fluorescent protein from the slice can be assumed equal to that released in the clearing solution. In this study, to quantify GFP loss,  $n=3$  200  $\mu\text{L}$  samples of the clearing solution were analysed with a plate reader (FLUOstar Omega, BMG Labtech, Ortenberg, Germany, Ex: 485 nm and Em: 544 nm). Fluorescence was read against a blank of fresh clearing solution, keeping the spectrofluorimeter settings (e.g. gain, number of flashes per well) constant over measurements to enable meaningful quantitative analyses of fluorescent protein release over time. Since the

clearing solution was completely refreshed at day 3, 5 and 7, for each brain slice the fluorescence data obtained at different time points were summed and expressed as cumulative fluorescence until day 10. To exclude fluorescent contributions due to tissue degradation or autofluorescence, tissue slices from CD1 mice were also clarified and clearing solution samples were taken at the same time points (i.e. day 3-5-7-10) analysed with the same plate-reader settings.

**Evaluation of image quality using standard indices.** Image stacks of L7GFP mouse slices treated with clearing solution and controls were mounted on a glass slide with FocusClear™ (Celexplorer Labs Co., Hsinchu, Taiwan) and then acquired with a confocal microscope (Nikon A1) at different time points. In particular, a 200  $\mu\text{m}$  z-stack with a step size of 2  $\mu\text{m}$  was acquired using a 10X objective with a pixel-to-micron ratio size of 0.46  $\mu\text{m}/\text{pixel}$  on a 512x512 matrix. The same confocal settings were used for all scans (i.e. 4.84 W laser power, emission and excitation wavelengths of 488 nm and 502 nm respectively). Two widely used indices for quantifying image quality were calculated:

### 1. Mean Pixel Intensity

To quantify tissue clarification as function of time, the Mean Pixel Intensity (MPI) of the objects of interest (PCs) was evaluated using the method described by Gonzalez, 2009 [63]. An automated algorithm was developed in Matlab (The Mathworks Inc.) to estimate the MPI for each of the 100 images in the z-stack. First a global threshold with Otsus method [64] was performed for every plane image of the stack to identify the objects (i.e. the PCs). Then, the MPI of thresholded objects in each plane was calculated using the

equation 2.2:

$$MPI = \frac{\sum_{i=1}^M I_M}{M} \quad (2.2)$$

where  $M$  is the number of object pixels and  $I_M$  their pixel intensity.

## 2. Contrast-to-Noise Ratio

Although the MPI is a measure of the signal, it is not directly linked to the information content of the image, which also depends on contrast between labeled neurons and the background. An alternative parameter for evaluating light scattering through the depth of the slice taking into account the image background is the Contrast-to-Noise (CNR) ratio defined as in equation 2.3:

$$CNR = \frac{MPI - I_b}{\sqrt{\frac{\sigma_m + \sigma_b}{2}}} \quad (2.3)$$

where MPI is as defined previously,  $I_b$  is the mean intensity of the background,  $\sigma_m$  is the standard deviation of the objects and  $\sigma_b$  the standard deviation of the background [65].

Once again, the CNR was calculated using an automated routine in Matlab. For each image in the stack, the Otsu-based thresholding method described was used to identify the objects of interest and discriminate them from the background. Then, assuming  $\sigma_b = \sigma_m$ , as proposed by Song and co-workers [65], the CNR was calculated according to equation 2.3.

**Sample evaluation and statistical analysis.** Five animals were employed for the MPI and CNR analyses, using  $n = 2$  slices per day for both experimental samples and controls. Thus, a total of  $n = 18$  slices were employed, 2 for the time 0 analyses and 16 for the other time-points,

i.e. 2 (replicates) \* 4 (time points) \* 2 (treatments) = 16. Each sample was imaged in 4 different regions, thus averaging 8 datasets from 2 slices per data point. Sample from different animals were pooled together as replicates for the analyses, assuming no inter-animal difference.

Six animals, three L7GFP mice and three CD1, were used for the macroscale BTCi and protein loss experiments, again pooling samples together. Here a total of  $n=10$  slices (5 controls in PBS + 5 samples in clearing solution) were used throughout the 10 days to determine average daily values of BTCi and GFP leakage. Unlike the MPI and CNR analyses, BTCi and GFP loss experiments were performed on the same slice until day 10, obtaining 5 replicates per experiment and time point investigated.

Statistical analyses of BTCi, GFP loss, MPI and CNR data were carried out using ANOVA followed by Tukeys Multiple Comparison Test, setting significance at  $p<0.05$ .

## 2.2.2 Results

**Bulk Tissue Clarification index (BTCi) evaluation.** Assuming no differences in the gross optical properties between cerebellum slices, data from different sections acquired at the same time points were grouped together as sample replicates to evaluate the BTCi.

The initial BTCi for untreated slices (i.e. time 0 in Figure 2.3A) was  $0.43 \pm 0.04$ . For samples immersed in clearing solution, this index increases significantly over time ( $p>0.05$ , one-way ANOVA) until it reaches a plateau at day 5 (BTCi =  $0.88 \pm 0.11$ ). On the other hand, the BTCi does not change significantly over time ( $p>0.05$ , one-way ANOVA) for cerebellar slices immersed in PBS (i.e. the negative control).

**Evaluation of GFP fraction lost.** As fluorescence from un-labelled tissue slices was similar to that of the virgin clearing solution, we can



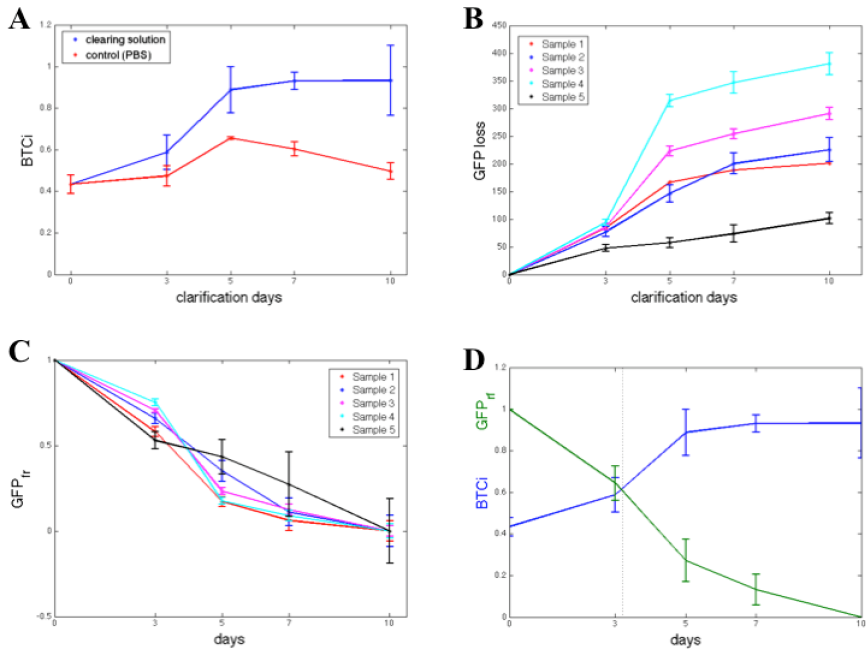


Figure 2.3: **A**  $BTC_i$  as a function of clearing time for control cerebellar slices in PBS ( $n=5$ , red) and in CLARITY clearing solution ( $n=5$ , blue) slices. **B** Cumulative GFP measured in the clearing solution over time ( $n=5$  slices). **C** Fraction of GFP retained ( $GFP_{fr}$ ), expressed as in equation 2.4, showing no significant differences between slices at the same time point. **D**  $BTC_i$  and  $GFP_{fr}$  time series obtained grouping results from the 5 different slices together, showing the relationship between the two parameters.

assume that there are no fluorescent components from tissue degradation or autofluorescence of brain components, and so all the signal detected by the spectrofluorimetric analysis refers to GFP loss in the clearing solution. The cumulative GFP loss from each sample is reported in Figure 2.3 (B). Data for GFP loss in controls are not shown as the values were either negative or close to zero, indicating levels of GFP close to or below the limit of detection. As shown in the figure, the rate of GFP leaked is initially high but tends to decrease with time towards an equilibrium value, typical of passive diffusion.

Although the trend for all slices examined is similar, it is not possible to assume a slice-independency as supposed for the BTCi evaluation. Indeed, the amount of GFP leaked into the clearing solution, expressed as arbitrary fluorescence units, varies from slice to slice because of the heterogeneous distribution of PCs in the cerebellum ( Figure 2.3 (B)). Hence an appropriate normalization is needed to meaningfully compare results from different slices. Assuming that GFP loss is a diffusive process, each sample loses the same fraction of protein at equilibrium. Since the cumulative GFP release did not change significantly between day 7 and 10 (i.e. the release of GFP appears to have reached a plateau and does not increase significantly over time), we assume that day 10 corresponds to the equilibrium state. Therefore, to normalise the loss of fluorescent protein ( $GFP_{loss}$ ) from each slice, the cumulative fluorescence values obtained from the clearing solutions were divided by their respective values at day 10,  $GFP_{loss}(t_{end})$ . A first one-way ANOVA analysis was performed on normalised GFP data obtained at each of the time points investigated to verify that this parameter is not slice-dependent (Figure 2.3 (C)). Then, data from different slices collected at the same time point were grouped together to give the fraction of fluorescent protein retained, expressed as in equation 2.4:

$$GFPfr(t) = 1 - \frac{GFPloss(t)}{GFPloss(t_{end})} \quad (2.4)$$

The fraction of fluorescent protein retained decreases continuously over time, as expected for passive diffusion (Figure 2.3(D)). The corresponding BTCi is plotted in the same graph to highlight the correlation between tissue transparency and GFP specific fluorescence of the sample.

**MPI and CNR evaluation.** The image based MPI and CNR analyses of the confocal z-stack images are reported in Figure 2.4. For the sake of clarity, only the mean values are shown. Although the variations are not statistically significant due to the unavoidable intrinsic variations between slices and the heterogeneous distribution of cells in each region imaged, there is a notable difference in trends between the samples immersed in the CLARITY clearing solution and PBS. The MPI decreases with increasing depth in controls and this trend is fairly independent of the number of days the slice is immersed in PBS (Figure 2.4(B)). On the other hand, in clarified tissues the MPI decreases with depth during the first few days in clearing solution and then increases inside the slices, reaching the highest values at day 5 (Figure 2.4(A)). Similar results are obtained for the CNR (Figure 2.4(C) for the slices immersed in clearing solution and Figure 2.4(D) for the PBS-immersed ones); for a given depth in the sample the highest CNR values are found at day 5 of clarification. To illustrate the power of the clearing method for imaging neural structure, figure 2.5 shows a volume view of a 3D reconstruction from a confocal stack acquired at day 5. This type of image cannot be obtained from 1 mm-thick slices of un-cleared brain tissue because of light scattering.

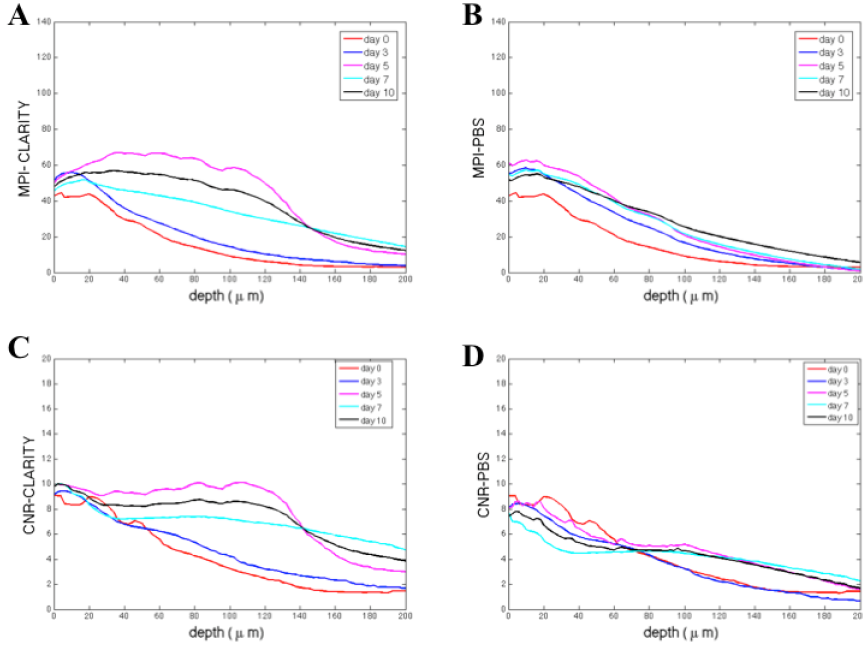


Figure 2.4: (A) Mean pixel intensity (MPI) as a function of stack depth for tissue slices immersed in clearing solution for different times ( $n=2$  slices per line). (B) MPI for controls ( $n=2$  slices per line). (C) CNR (contrast to noise ratio) as a function of stack depth for tissue slices immersed in clearing solution for different times ( $n=2$  slices per line). (D) MPI for controls ( $n=2$  slices per line). For each sample acquired, the MPI and CNR were calculated over 200  $\mu\text{m}$  thick regions from 100 different images spaced 2  $\mu\text{m}$  apart, i.e. a total of 100 data points).

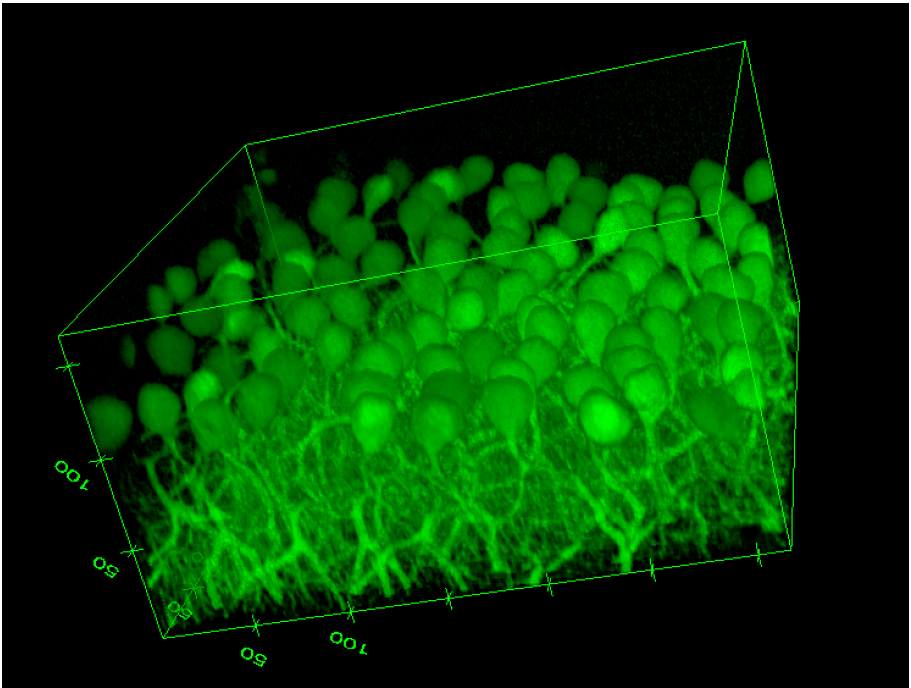


Figure 2.5: Volume view of a confocal stack acquired at day 5 (Ex/Em: 488/502, pixel-to micron ratio size:  $0.62 \mu\text{m}$ , z-resolution:  $1.2 \mu\text{m}$ ). Volume dimensions (w\*l\*h):  $317*317*172 \mu\text{m}$  (numbers in the edges of the box represent distances in microns).

## 2.3 Optimization method for perfused and unlabelled tissues

In the previous sections, it has been demonstrated that the delipidation time for GFP genetically-labelled tissues can be optimised by using two macroscopic parameters, the bulk tissue clarification index (BCTi) and the fraction of GFP lost in clearing solution simultaneously.

In case of non-genetically labelled tissues, since there are no specific fluorescent markers to monitor over time, the optimization method described above has to be modified by evaluating the fraction of protein lost (i.e.  $P_{loss}$ ) in the clearing solution, i.e. using colorimetric assays. In this case, we evaluate the overall protein loss, and assume that all proteins are leaked to the same extent. In fact, several colorimetric, reagent-based protein assay techniques have been developed [66]: the reagent is added to the proteins, producing a colour change in proportion to the amount added. Protein concentration is determined by reference to a standard curve consisting of known concentrations of a purified reference protein. Due to its compatibility with high concentration of SDS and basic pH, the BCA (bicinchoninic acid) protein assay was chosen to estimate the  $P_{loss}$  in the clearing solution.

### 2.3.1 Materials and Methods

To perform the experiments, CD1 mice were sacrificed. While tissue preparation and clarification and BCTi evaluation over time were the same detailed in the Section 2.2.1, clearing solution sampling and processing to evaluate the  $P_{loss}$  are described below.

### 2.3.2 Quantification of the proteins lost in solution

**Clearing solution sampling and BCA assay.** At each clearing time point (i.e. day 3-5-7-10), 1 mL sample of the solution was placed in a 1.5 mL eppendorf tube and stored at  $-20^{\circ}\text{C}$ .

The Pierce<sup>TM</sup> BCA Protein Assay Kit was used (Thermoscientific) for the colorimetric and quantitative detection of total proteins released in the clearing solution at each time point. Briefly, the procedure involves the mixing of 25  $\mu\text{L}$  of each sample with 200  $\mu\text{L}$  of the BCA working reagent (sample to working reagent ratio = 1:8) in a 96-Well Plate. The solution was vortexed for 30 seconds and incubated at  $37^{\circ}\text{C}$  for 30 minutes. Then, the absorbance is measured at 562 nm on a plate reader (FLUOstar Omega, BMG Labtech, Ortenberg, Germany).

Before starting the test, a series of standard solutions, in which the concentration of a given analyte (in this case, albumin) in the clearing solution is accurately known, are prepared to generate a calibration curve. For each of the standard solutions, the absorbance was measured using the same plate reader and the calibration curve was constructed fitting a 4-parameter curve through the experimental points.

The clearing solution samples were defrosted and analysed with the same settings used for the calibration curve to determine the amount of protein loss during clarification. Protein content in solution was read keeping the plate reader settings constant over measurements to enable quantitative measurements over time.

As previously detailed for the GFP fraction lost in solution, since the clearing solution was completely refreshed at day 3, 5 and 7, for each brain slice the data obtained at different time points were summed and expressed as cumulative signal until day 10.

**Sample evaluation and statistical analysis.** Two CD1 mice were employed for estimating the fraction of protein lost in solution. For each mouse, four 500  $\mu\text{m}$ -thick slices were obtained using a vibratome, for a total of eight slices used through the 10 days to determine daily values of proteins lost in solution.

Statistical analysis of the data was carried out using ANOVA followed by Tukey's Multiple Comparison Test, setting significance at  $p < 0.05$ .

### 2.3.3 Results

Although the trend of the proteins lost in clearing solution over time for all the slices is similar, it is not correct to assume a slice-independence. In fact, the amount of protein leaked into the clearing solution varies from slice to slice because of the physiological heterogeneity of the brain samples. Moreover, unlike the cumulative GFP lost, which reaches an equilibrium value, the total protein content lost in solution obtained with the BCA assay continues to increase over time. For this reason, the normalization with respect to the 10 day time point used for the GFP-labelled samples cannot be applied.

Some form of normalization is needed to meaningfully compare results from the different slices. Since the total protein in mouse brain was estimated at 10 % (wt) [67, 68], the slices were weighted and the total protein content in the slices prior to clarification was estimated. Specifically, as reported by Chung et al. 2013 [21], the protein fraction in mouse brain is  $\frac{1}{10}$  of the total wet weight. The value obtained was used to normalize the cumulative protein data at each time point.

A first one-way ANOVA analysis was performed on normalised data at each time point investigated to verify that the parameter calculated is not slice-dependent. Then, data from different slices collected at the same time point can be pooled together to give the fraction of protein



retained  $P_{fr}$  (equation 2.5):

$$P_{fr}(t) = 1 - \frac{P_{loss}(t)}{0.1 * w_{slice}} \quad (2.5)$$

where  $w_{slice}$  is the slice weight before starting the clarification.

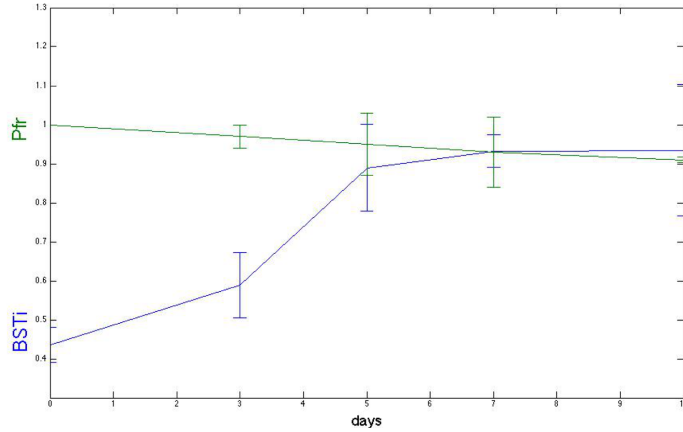


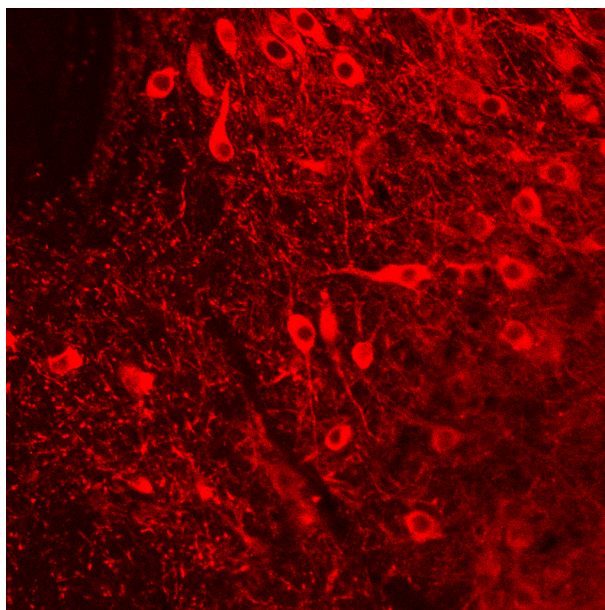
Figure 2.6:  $BCTi$  and  $P_{fr}$  time series obtained grouping results from the 5 different slices together, showing the relationship between the two parameters.

In Figure 2.6  $BCTi$  and  $FP_{fr}$  are plotted in the same graph to highlight the correlation between the two parameters: while the fraction of protein retained decreases continuously over time, the  $BCTi$  follows the same trend as reported in Figure 2.4(D), reaching a plateau at day 5. Although the curves intersect at day 7, the optimum clearing time was identified as day 5, since there are no significant differences in  $BSTi$  between day 5 and day 7.

To show the compatibility of CLARITY with immuno-labelling, clarified murine brain slices were stained with antibodies. Briefly, immunostaining was performed on free-floating slices, incubated in 10 % normal goat serum in 0.1 M PBS for 1 h and then with rabbit anti-SERT (Millipore, USA, 1:200 dilution) antibody to 0.1 M PBS overnight at 4°C. After two

further washes in 0.1 M PBS, the sections were incubated in anti-rabbit Alexa Fluor 561 antibody (1:200 dilution) in 0.1 M PBS overnight.

Figure 2.7 shows a detail from a confocal stack acquired at day 5, representing the *substantia nigra* SERT-positive neurons.



*Figure 2.7: Confocal image acquired at day 5 (Ex/Em: 561/594, pixel-to micron ratio size: 0.31  $\mu\text{m}$ ), representing a detail of substantia nigra SERT-positive neurons.*

## 2.4 Customization of the CLARITY2 protocol for un-perfused tissues

The original CLARITY2 protocol is designed for perfused tissues: in fact, the first steps of the protocol involves the intra-cardiac perfusion of the animal. This procedure is used to wash blood off the vessels as well as to systemically deliver the hydrogel into the whole sample. Therefore,

an alternative to perfusion is required to clarify samples which cannot be perfused, such as human brains.

Although it is important to remove blood, which causes light scattering, the main limitation in the context of un-perfusible tissues is the penetration of the hydrogel through the sample. Hydrogel embedding cannot be performed post-slicing because the gel tends to crumple the slices. Hence the gel monomer has to diffuse through the whole thick tissue, to optimise slice thickness and clearing time for un-perfused tissue, such that gel monomer penetration, tissue handling and clarification without excessive protein loss are guaranteed, a customised protocol was established.

### 2.4.1 Materials and Methods

**Customization of the tissue clarification.** Human samples, consisting in two 5\*2\*3 cm<sup>3</sup>-thick blocks of brain cortex, were obtained from "Santa Chiara" Hospital of the University of Pisa. The samples were removed for routine diagnostic purposes, following a procedure approved by the Local Ethics Committee.

Fresh brain tissue clearing was performed partially following the protocol described in Liu et al., (2015) [59]. Some amendments to the protocol are detailed below. In order to facilitate blood removal through the sample by passive diffusion, samples were washed once a day with 20 mL of PBS enriched with 5000 U/L of nadroparin calcium (i.e. Fraxiparine, Glaxo-SmithKline), an heparin-based anticoagulant usually used for hemodialysis. Then, samples were put in a falcon with 35 mL of hydrogel for 9 days, with fresh solution every three days to allow hydrogel penetration inside the tissue. After that, polymerization was performed as detailed in Section 2.2.1.

**Slice thickness optimization and statistical analysis.** After hydrogel polymerization, tissue blocks were cut in 36 slices using a vibratome. In particular, twelve 250  $\mu\text{m}$ , twelve 500  $\mu\text{m}$ - and twelve 1 mm- thick slices were obtained. Slices were then immersed in 10 mL of clearing solution at 4°C for 11 days. Solution was changed at 3, 5, 7, and 9 days, and 1 mL was sampled at each refreshing.

Since human samples are un-labelled, the procedure for clarification optimization, as well as the statistical analysis, is based on the BCTi as a global clarification index, as verified in any previous analysis.

Two-way ANOVA followed by Tukey's Multiple Comparison Test was performed to evaluate the difference in terms of clarification as a function of both clearing timing and slice thickness, setting significance at  $p < 0.05$ .

## 2.4.2 Results

Assuming no differences in the gross optical properties between human brain slices, as previously assumed for cerebellum slices, data from different sections with the same thickness, acquired at the same time points, were grouped together as sample replicates to evaluate the BTCi. Figure 2.8 shows the BTCi at different time points for 250  $\mu\text{m}$ -, 500  $\mu\text{m}$ - and 1 mm- thick slices respectively.

Although the BTCi for 1 mm-thick slices increases significantly over time reaching a plateau at day 5, the clarification is less efficient than for the cerebellar murine slices: in fact, the BCTi is much lower (BTCi =  $0.57 \pm 0.04$ ).

On the other hand, the BCTi for 250  $\mu\text{m}$ - and 500  $\mu\text{m}$ - thick slices is higher, reaching a plateau respectively at day 7 (BTCi =  $0.73 \pm 0.04$ ) and day 9 (BTCi =  $0.71 \pm 0.01$ ). Since there are no significant differences between day 7 and day 9 (two way ANOVA,  $p > 0.05$ ), the 500-  $\mu\text{m}$  thick slices clarified till day 9 are a better choice for imaging cells and for

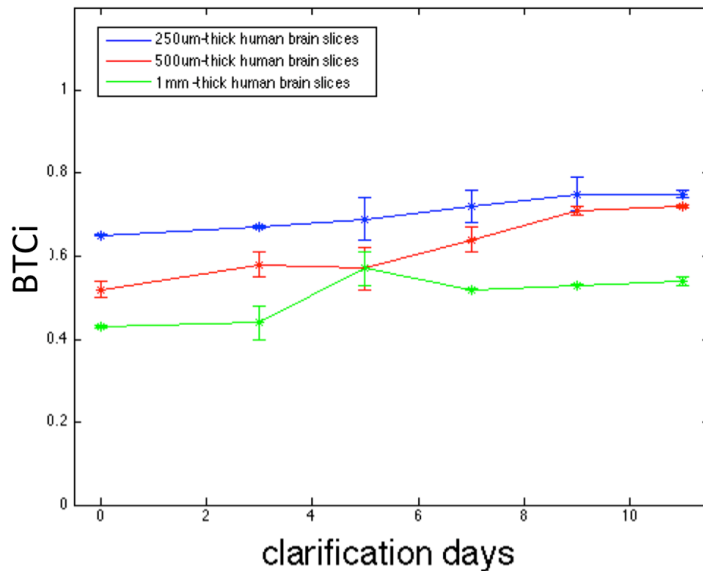


Figure 2.8:  $BCT_i$  as a function of clearing time for 1mm- ( $n=12$ , blue), 500  $\mu\text{m}$ - ( $n=12$ , red) and 250  $\mu\text{m}$ - ( $n=12$ , green) human brain slices.

handling.

The fraction of protein loss in clearing solution is not shown, since its trend decreases continuously over time, similarly with that obtained for the murine slices.

## 2.5 Discussion

Most investigations on the optimization of CLARITY and its variations focus on the composition of the hydrogel embedding and clearing solutions and on design of the electrophoretic chamber. Whatever the method and reagents used, the goodness of any clearing process is essentially the best trade-off between tissue transparency and the presence of molecules of interest to imaging. For a given clearing cocktail, the former increases

with clearing time, while the latter are inevitably lost due to a shift in equilibrium between tissue bound and unbound moieties or protein degradation.

In this light, a method was designed to characterize the clearing process as a function of time and so determine the optimum clearing time for thick brain slices.

The approach described was applied to 1 mm-thick cerebellum slices of L7GFP mice, whose Purkinje neurons are fluorescently labelled, using the diffusion-based CLARITY2 method. The goodness of clarification was quantified by evaluating both the bulk tissue clarification index (BTCi) and the fraction of GFP lost in the clearing solution. Figure 2.3(D) summarizes the main results of the macroscale analyses: BTCi increases with clearing time, reaching a plateau after 5 days, while the fraction of GFP retained decreases rapidly. Protein loss is in fact unavoidable during tissue clarification, for example Chung et al.'s original paper [21] reports an 8% decrease in protein content, albeit some scientists on the CLARITY forum claim complete loss of GFP signal (<http://forum.claritytechniques.org/discussion/-32/loss-of-gfp-signal>). Although light can propagate further into a highly transparent clarified tissue, the effective measured signal, linked to a specific protein of interest, is reduced.

To attest the validity of the approach, brain slices were also imaged using confocal microscopy to calculate the mean pixel intensity (MPI) of neurons and the contrast-to-noise ratio (CNR) as a function of z-stack depth. The results show that slices cleared for 5 days have the highest MPI and CNR for the widest range of depths. This trend is not observed for PBS-immersed slices.

The method can be also used for un-labelled tissues: it has been shown, in fact, that similar results in terms of clarification timing were obtained establishing a trade-off between BCTi and the fraction of protein lost in

the clearing solution evaluated using colorimetric, reagent-based assays (i.e. BCA assay)(Figure 2.6), attesting to the suitability of the BCTi as a global index of goodness of clarification

Finally, in case of un-perfusable tissues, the method designed provides also an optimization of slice thicknesses to maximise the CLARITY efficacy (as shown in Figure 2.8). In this case, the CLARITY protocol customization for human brain tissues used during this PhD thesis was that reported in Liu et al. [59]: the complete the fully penetration of the hydrogel inside the brain through passive diffusion was not assessed.

Thus the delipidation time for perfused tissue slices can be optimised by measuring the bulk tissue clarification index and the fraction of protein lost in clearing solution simultaneously. For all the examples detailed, the optimum clearing time is when tissue clarification just reaches its maximum, as any further clearing leads to excessive and useless signal loss. Prolonging the clarification treatment does not significantly improve tissue transparency and may also be detrimental for the maintenance of the samples architectural and biochemical features.

1

---

<sup>1</sup>Most of the results presented in this chapter have been published in : Magliaro et al., "Clarifying CLARITY: quantitative optimization of the diffusion based delipidation protocol for genetically labelled tissue", *Frontiers in Neuroscience - Brain Imaging Methods*, *in press*.





# Chapter 3

## SmRG: a Smart Region-Growing algorithm for single-neuron tracing

*"Every branch of science seems to intent  
on demonstrating that the world is supported  
by the most minute entities,  
such as the impulse of neurons"*

*(I. Calvino)*

### Abstract

The reconstruction of neuronal populations, a key step in understanding neural circuits, remains a challenge in the presence of densely packed neurites. In fact, to pursue the study of the relationship between neuron morphology and function, an accurate three-dimensional reconstruction of brain cells is needed, in order to facilitate detailed anatomical measurements. Although advances in high-resolution imaging have provided valuable novel insights into brain micro-structural features (e.g. single photon confocal microscopy), currently a technical roadblock for these studies is the inability to automatically trace neuronal structures in their

own three-dimensional arrangement within the brain cortex. To tackle these difficulties, a Smart Region Growing (SmRG) algorithm was developed to trace single neurons from confocal stacks, based on local features of the image intensity value histogram. Here the SmRG algorithm is detailed, demonstrating its performance by comparing it with manual tracing operated by experts, with a gold standard tool (i.e. Tree2Tree tool [23]), with a traditional 3D region growing algorithm and by a “self-validation”.

### **3.1 State of Art of algorithms and tools for neuron 3D tracing from confocal stack acquisitions**

Mapping neural circuits, one of the central tasks in brain studies, is crucial for obtaining the full delineation of the Connectome [21], that requires the identification of individual neurons, their synaptic connections and their cell type from imaging datasets of neuronal populations [69, 70]. These analyses depend largely on digitalization of the morphologies of individual neurons or neuronal trees in a population [13, 71]. The combination of clarification methods, capable of generating transparent tissues preserving the native brain architecture, as detailed in Chapter 2 and advances in imaging techniques, enabling the generation of high-quality population data could be of inspiration for the reconstruction of large neuronal populations.

Current imaging techniques, and in particular confocal microscopy, gives high-resolution data at different depths in a sample ( $<50 \mu\text{m}$ ). Although confocal microscopy allows effective serial optical sectioning of a specimen [72], the intensity values of the voxels constituting a confocal im-

age stack are likely to vary discontinuously, affecting the post-processing and analysis, even acquiring cleared tissues. In particular, two different sources of signal variability can be found in single photon confocal microscopy images:

1. *Light attenuation and scattering across the sample*, that returns different image intensity at different depths in the sample [73, 74, 75] (Figure 3.1);

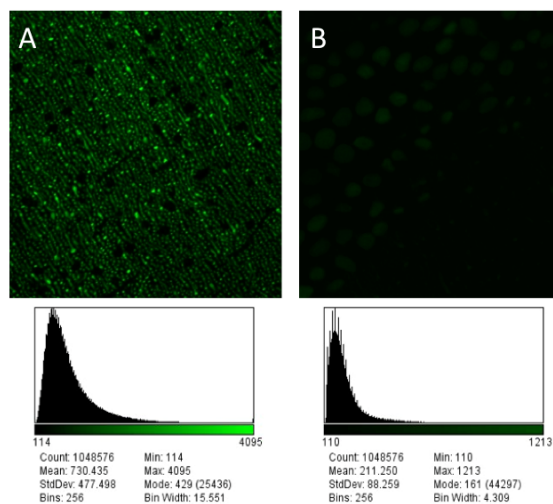
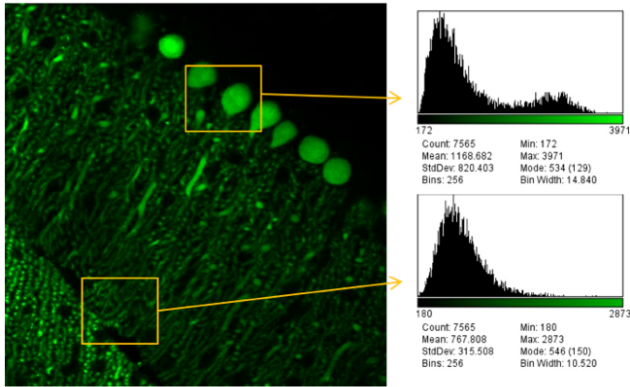


Figure 3.1: Images from the same confocal stack, representing L7GFP clarified murine Purkinje neurons, and relative histogram for (A)  $z = 0 \mu$  and (B)  $z = 100 \mu m$ .

2. *Non-uniform distribution of fluorescent cells through the sample*, which adds in-plane differences to the signal (as shown in Figure 3.2)

In order to facilitate neuron tracing from confocal datasets, different studies on the restoration of intensity of image stacks has been described



*Figure 3.2: Image from a confocal dataset representing L7GFP clarified murine Purkinje cells: in-plane signal differences due to biological variability are evident.*

in the State of Art, also trying to take into account photo-bleaching of the fluorophore [76]. However, none of the methods presented allow a precise correction. In fact the nature of light intensity changes between the adjacent optical sections tends to often be ignored and moreover the mechanisms of photo-bleaching are not well understood.

Manual tracing of neurons has been used to resolve dendritic morphology, as well as to perform geometric reconstructions. This is commonly done manually with programs such as NeuroLucida (MicroBrightField) [31] or Neurozoom (Neurome). The accuracy is however strongly dependent on individual data interpretation to estimate midlines and diameters of dendrites. In addition, it is extremely time consuming and impractical for dense population reconstruction.

For this reason, in the last few decades different tools have been developed, to trace individual branches of neuronal trees [34, 40, 77, 78, 79, 80]. These approaches for the investigation of neural structures at the micro-

structural level are not useful for dense population, in which closely spaced neurites may come into contact, connect or overlap.

Among the various schemes, some of them deserve a brief description. Region growing algorithms with active contour techniques [25, 26, 27, 28], which rely on shrink/expansion operations done by the minimization of an energy function, are sensitive to local minima or noise, and thus inadequate for confocal datasets. On the other hand, global approaches to neuron segmentation, such as the Tree2Tree tool [23, 24] are not valid for our purpose to isolate single neurons due to the local intensity variability of confocal datasets.

The above mentioned segmentation techniques for 3D neuronal tracing are not the only ones available in the literature: different points of view and approaches have been proposed by the scientific community. Wolf et al.(2009) [29] propose a fuzzy scheme to segmentation due to the typical characteristics of neural images. In fact, the structures of interest do not always represent a crisp set which is well distinguished from the background or other structures, thus similarity criteria based on fuzzy logic can be a winning approach for region growing techniques. Another technique which may be robust to low and fluctuating contrast is based on the 3D wavelet transform [30]. In this method, authors use multi-scale edge detection in order to locally segment the structures of interest with less sensitivity to noise. A different kind of approach is to perform an atlas-based segmentation: while segmentation should be fully automated, big data availability and registration methods are a must [32]. Unfortunately, all the techniques described are often useless to trace dense neurons in their own arrangement in the brain.

Recently, a tool partially mimicking human strategies to separate individual neurons was developed, NeuroGFPS-Tree [33]. However, at least in the first tracing phases, it is strongly user-dependent, and so prone to

human bias. An other limitation is due to the fact that most of the tools and algorithms are developed to follow the neurite patterns, tracing the neuron skeleton, so they cannot be used to extract morphological variables, such as the Surface-to-Volume ratio of the structure segmented, which is considered a raw index of neuron arborization complexity.

When it is necessary to handle images with intensity inhomogeneity and noise of spatially varying strength, such as those of confocal acquisitions, region growing schemes could represent a robust approach to segmentation. The region growing -based algorithm, one of the simple region-based image segmentation methods used to separate objects with similar characteristics within images follows two fundamental principles: the selection of a seed and the definition of a homogeneity predicate. The basic idea is to grow a region starting from a "seed" pixel/voxel and labelling each neighbour pixel/voxel of a region-of-interest according to similarity criteria. The process is iterated until there are no more labelable pixels/voxels. The homogeneity criterion can be based on similarity of discontinuity measures. The robustness of seed-based techniques is generally affected by the signal intensity and presence of noise; however, these approaches are computationally efficient, thus encouraging researchers to develop methods to overcome the above mentioned difficulties.

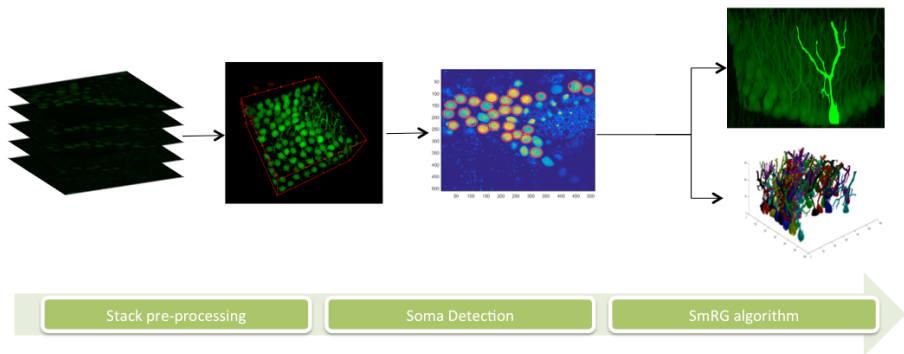
Due to the intensity variability of the confocal datasets, region growing schemes based on histogram local characteristics could represent a robust approach to segmentation. In some models, the local image intensities are described by local Gaussian distributions with different means and variances, in order to distinguish objects from background [34]. However, confocal datasets cannot always be described with a set of local Gaussian distributions, and a different local scheme to isolate neurons from background is a must.

To overcome this limitation, a smart region growing (SmRG) algorithm

operating locally in a 3D scheme was developed in the course of this work to trace and isolate single neurons in their native arrangement within the brain. Here the SmRG work-flow for single-neuron 3D tracing is detailed and validated using different approaches and different confocal datasets.

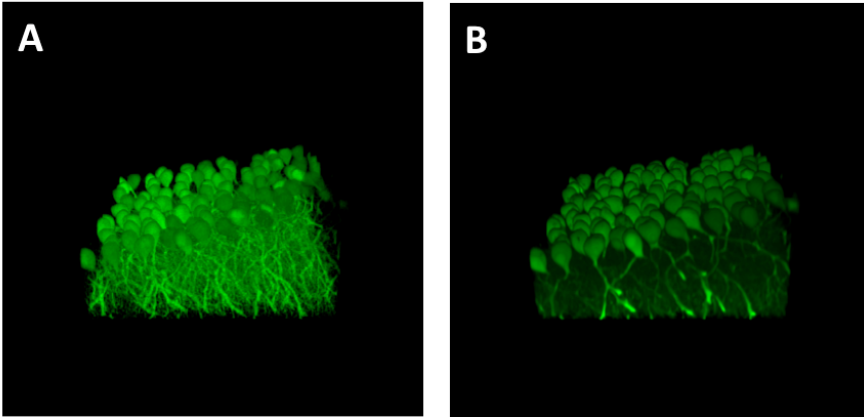
### 3.2 SmRG algorithm description

The SmRG algorithm has been developed in MATLAB<sup>®</sup> (The MathWorks<sup>®</sup>, Inc., Natick, Massachusetts, USA). The SmRG work-flow can be divided in three main steps, as shown in Figure 3.3:



*Figure 3.3: Algorithm work-flow: after a pre-processing step, soma are identified and the SmRG algorithm is run to trace all the neurons in the stack.*

**Stack pre-processing** The image stacks acquired were firstly filtered with a  $3*3*3$  pixel-sized median filter in order to reduce noise, as shown in Figure 3.4. Then, an interpolation to cubic voxels was performed in order to have a more faithful representation of real neuron morphology. The process is necessary in case of different resolution of the stacks. In



*Figure 3.4: Volume rendering of (A) an original stack (Ex/Em: 488/502, pixel-to-micron ratio size:  $0.62 \mu\text{m}$ , z-resolution:  $1.2 \mu\text{m}$ ) and of (B) a  $3*3*3$  median-filtered and interpolated stack.*

fact, in order to minimize signal loss during acquisition due to fluorescent bleaching, z step is usually chosen as double that of the in-plane resolution.

**Soma recognition** After the pre-processing step, neuron somata were semi-automatically recognized. The only inputs the algorithm needs are the z-coordinate of the dataset on which there is at least one soma, and a range of soma diameters of the neurons to be segmented. The range of soma diameters can be chosen from the literature or with preliminary 2D slice imaging. Circle-shaped structures are automatically detected with the Houghs transform [81]. The result is shown in Figure 3.5. The (x, y) center coordinate of the found circles, added to the z-coordinate chosen by the user, are automatically used by the algorithm as initial seed.



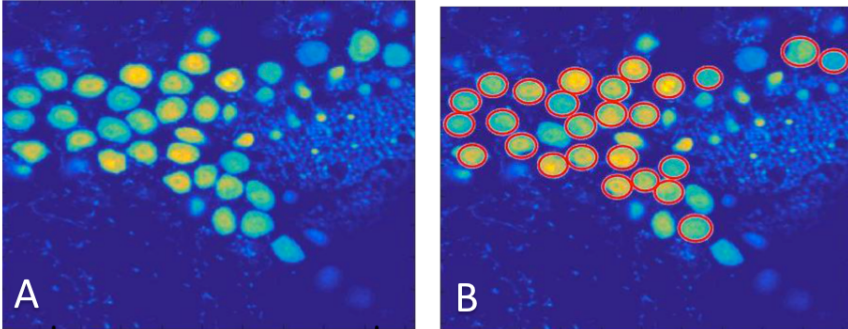


Figure 3.5: (A) 2D image from an original stack chosen by the user (Ex/Em: 488/502, pixel-to micron ratio size:  $0.62 \mu\text{m}$ , z-resolution:  $1.2 \mu\text{m}$ ) and (B) after the Hugh transform, which identifies somata and their relative soma center coordinates. The outputs are subsequently used as initial seed for the SmRG algorithm.

**Single Neuron tracing** This step is a modification of the 2D/3D region growing algorithm by Daniel Kellner, shared on the Matlab File Exchange website (<http://www.mathworks.com/matlabcentral/fileexchange/32532-region-growing--2d-3d-grayscale-/content/regionGrowing.m>). The changes made to the original algorithm are outlined below.

Since the confocal datasets from fluorescent specimens are characterized by a great spatial variability in terms of pixel intensity, as previously highlighted, one approach for facing this issue is the use of a locally adaptive thresholding for the segmentation of neural structures. Here, a local histogram-based region growing was developed.

The background and neuronal tissue-related signals show a bimodal intensity distribution. Specifically, the background signal is characterized by a unimodal distribution with lower signal intensity with respect to neural tissue. The intensity distribution of neural tissue signal shows a

higher dispersion with respect to the background distribution. Moreover, the samples showed a quite flat signal distribution characterized by a low peak. For this reason, the use of model fitting procedures such as Gaussian mixture models is not feasible.

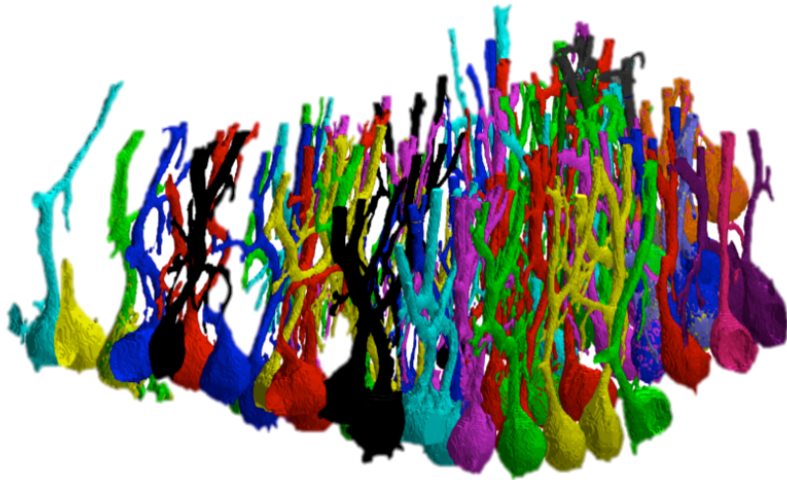
In this light, a local threshold was determined to distinguish background and neurons looking at the derivative of the intensity histogram. A histogram-knee is defined as the first minimum of the histogram, after the first histogram peak and it was estimated locally on a  $16*16*16$  pixel<sup>3</sup> sub-volume. The histogram-knee separates the two classes of pixels within the image (i.e. neuron and background) and therefore represents the homogeneity predicate for the region growing procedure. If a pixel lies on the left of the knee it will be considered as a background pixel, while if it does not it will belong to the neuron pixels.

The region growing process starts by selecting a pixel belonging to a particular soma. A cubic sub-volume is centered around the selected initial seed and the histogram-knee calculation is performed. At this point the 26 neighbour pixels of the seed are classified as background or neuronal tissue. This procedure is repeated for each new pixel belonging to the neural tissue if a condition of distance is met. Specifically, the knee value is calculated if the distance from the pixel of the last knee-estimation is bigger than 5 pixels ( $3 \mu\text{m}$ ). The region growing process ends when there are no more pixels which satisfy the previous conditions.

Note that the region growing algorithm runs as many times as the number of seeds found in a given confocal dataset. An example of SmRG algorithm output is given in Figure 3.6.

### **3.3 SmRG algorithm performance evaluation**

The SmRG algorithm's ability to trace single neurons within their native arrangement in the brain was tested with four different approaches:



*Figure 3.6: An example of SmRG algorithm output. The input confocal dataset represents stacks from clarified L7GFP murine cerebellum slices. Different colours refer to different structures segmented with the SmRG algorithm.*

- A comparison with manual tracing operated by neuro-imaging experts;
- A comparison with a standard 3D region growing algorithm;
- A “Self Validation” approach on segmented somata;
- A comparative analysis with Tree2Tree tool [23], considered a “ground of truth” of 3D neuron tracing.

Moreover, different image stacks, acquired with different confocal settings and representing different types of neurons, were used:

- **Murine clarified cerebellar slices:** cerebellar 1 mm -thick slices of L7GFP mice were prepared and clarified as detailed in Chapter 2. Confocal acquisition settings were shown in Table 3.1;
- **Fruit fly *Drosophila* brain:** image stacks representing neurons from *Drosophila* brains were downloaded from [http://viva-lab.ece.virginia.edu/suvadip\\_docs/Neuron/research\\_neuron.html](http://viva-lab.ece.virginia.edu/suvadip_docs/Neuron/research_neuron.html).

### 3.3.1 SmRG vs manual tracing

Manual segmentation operated by an expert likely results in substantial subjective bias. Moreover, for dense packed cell populations (i.e. Purkinje cells in the cerebellar layers), manual extraction of features from 3D dataset is labour intensive, time-consuming and not always an achievable task, due to the complexity of neuronal structures. Nevertheless, in the field of neuro-imaging, manual tracing is still the gold standard of segmentation procedures.

In this light, a standard validation of the SmRG algorithm through manual segmentation operated with neuro-imaging experts was performed. In

*Table 3.1: Confocal Acquisition settings for 1-mm thick cerebellar slices from L7GFP mice*

<i>Parameter</i>	<i>Value</i>	<i>Units</i>
Magnitude	40x	
Grid	512*512	pixel
Pixel Size	0.62	$\mu\text{m}/\text{pixel}$
Laser Power	4.84	pW
Emission wavelength	488	nm
Excitation wavelength	502	nm
z-step	1.2	$\mu\text{m}$

particular, three neuro-experts were employed to manually trace Purkinje neurons from three different confocal image stacks representing cerebellar L7GFP mice clarified in Chapter 2. Using ImageJ [1], they were asked to scroll down confocal stacks and identify the neurites supposed to belong to a specific neuron using the "flood fill" tool. In parallel, the ImageJ 3D viewer is automatically refreshed to follow the neuron growth within the acquisition, as shown in Figure 3.7. To simplify the task, the images constituting the confocal dataset were previously thresholded using the Otsu method [64]. This step could merge neurites belonging to different neurons: for this reason, touching objects can be separated with the "paintbrush tool", available in ImageJ. The confocal image stacks were then processed with the SmRG algorithm, and the result were compared.

Figure 3.9 shows an example of a Purkinje neuron segmented with both the SmRG algorithm and the manual tracing operated by an expert.

In order to quantitatively evaluate the SmRG accuracy respect to the

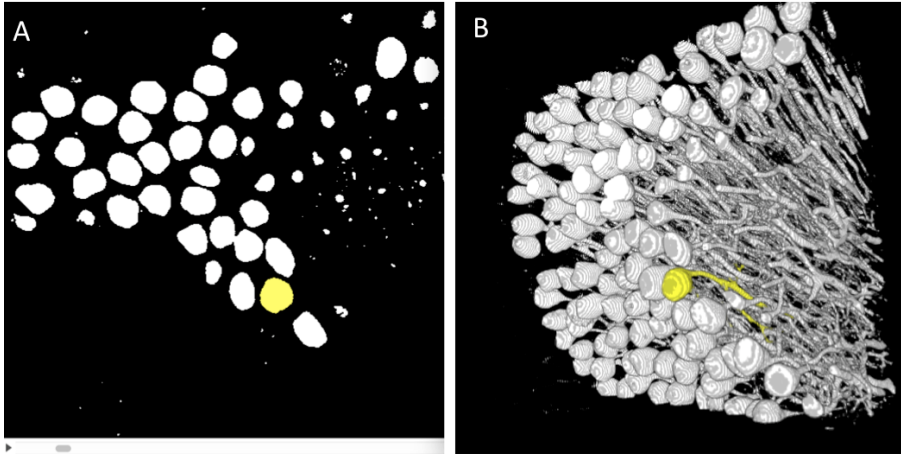


Figure 3.7: (A) The scroll down menu to visualize the images constituting the confocal dataset and to identify the neuron structure manually; (B) ImageJ 3D viewer automatically refreshed.

manual tracing,  $n=20$  neurons segmented with the two different techniques were morphologically characterized (see Chapter 4 for more details). In particular, the *Surface-to-Volume Ratio* was evaluated, as a raw index of neuron complexity. Then, the residual error was calculated as the difference between the Surface-to-Volume ratio of the SmRG traced neurons and the manually traced ones.

In addition, neurons were skeletonized and then the Sholl analysis with a constant number of spheres (see Chapter 4 for more details) was performed, in order to study neural dendritic arborization pattern around the soma.

As regards the first morphological parameter, the residuals from the difference between the Surface-to-Volume ratio of segmented SmRG neurons and manually traced ones are displayed in Figure 3.8. No statistically significant differences were found between the two datasets.

On the other hand, an example of the morphometric Sholl analysis

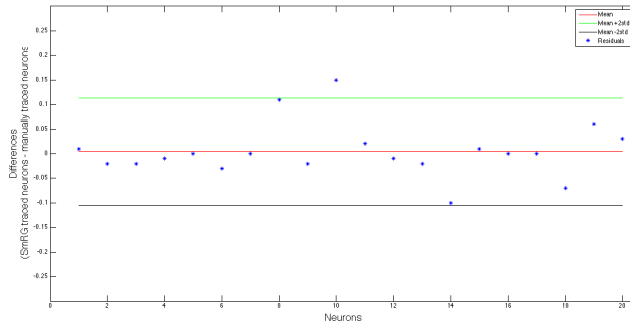


Figure 3.8: The residual error estimation for  $n=20$  neurons. The residuals are the differences between the Surface-to-Volume ratio in the Purkinje cells segmented manually and with the SmRG algorithm.

performed for a Purkinje cell segmented with the SmRG algorithm and with manual tracing is shown in Table 3.2. Here again, some differences were observed, but they were not statistically significant.

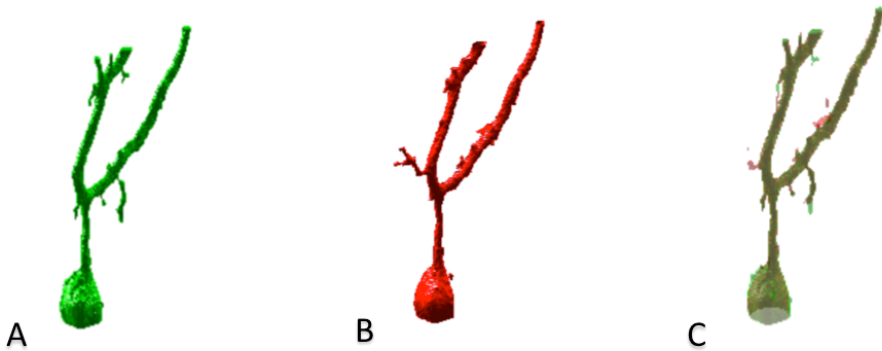
### 3.3.2 SmRG vs standard 3D region growing algorithm

In order to attest that the local thresholding implemented for the SmRG algorithm is better than the global one for the confocal microscopy dataset, image stacks were processed with both SmRG and a standard 3D region growing, available at <http://www.mathworks.com/matlabcentral/fileexchange/32532-region-growing--2d-3d-grayscale-/content/regionGrowing.m>. In particular, the same x-, y- and z- coordinates were used as initial seed; for the standard 3D region growing algorithm, the threshold was set as the first value automatically obtained with the SmRG one.

Table 3.2: Comparative Sholl analysis (with constant number of spheres) for a Purkinje cell segmented with the SmRG algorithm and through manual tracing performed by an expert

Radii ( $\mu\text{m}$ )	Intersections	Radii ( $\mu\text{m}$ )	Intersections
13.64	1	13.64	1
32.12	1	32.28	2
50.61	1	50.93	2
69.09	5	69.58	5
87.58	3	88.23	3
106.06	2	106.88	2
124.05	2	125.53	2
143.04	3	144.18	3
161.53	4	162.83	5
180.02	2	181.48	3
Maximum number of intersections			
5		5	





*Figure 3.9: An example of a neuron segmented with (A) the SmRG algorithm and (B) manually by an experts. For visually comparing the results, a merge of them is shown in (C).*

### 3.3.3 A “Self validation” approach on segmented somata

An internal validation was performed in order to estimate the goodness of the algorithm, using the information of the somata detected with the Hough transform. After the user-operated identification of the plane, the work-flow adopted for the “self-validation” (shown in Figure 3.11) consists of three phases:

1. Measurement of the center and the radius of each circle detected as initial seed position using the Hough transform;
2. Segmentation and new circle-shaped feature detection on the segmented image using the Hough transform;
3. Residual error calculation as the difference between original circle radii and segmented ones.

The Self-validation was conducted on  $n=20$  somata, from different 3D




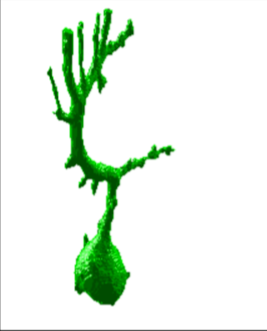

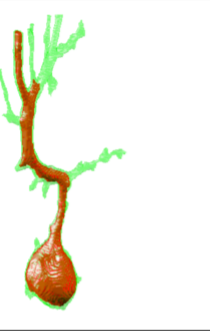
	SmRG	Standard RG	Merge
NEURON 1			
NEURON 2			

Figure 3.10: Two examples of neuron structures segmented with the SmRG algorithm and with a standard 3D region growing algorithm. To highlight the differences between the two techniques, a merge of them is shown in the last column.

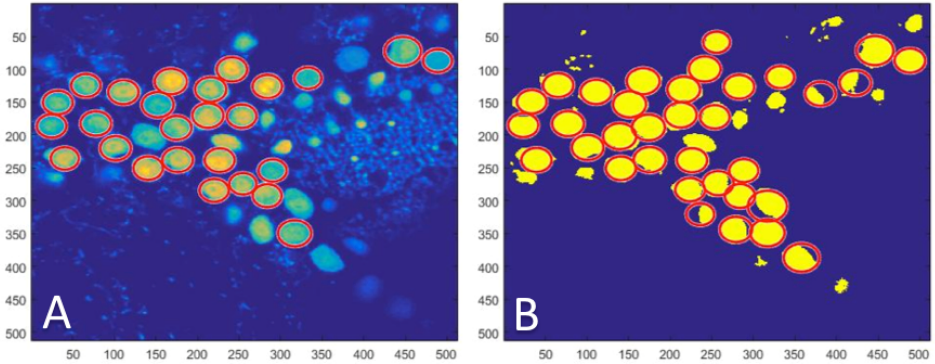


Figure 3.11: Hough transform-based circle detection applied on an specific z-plane of (A) the original stack and (B) the stack segmented with the SmRG algorithm

datasets.

Residuals from the difference between the radii of segmented structures and the original ones are displayed in Figure 3.12. The maximum error detected was  $<2.5$  px ( $1\text{px} = 0.62 \mu\text{m}$ ). This result confirms a good level of segmentation at least on neuron somata. This type of analysis cannot be done on dendritic structures because of the limit of resolution of the Matlab function *imfindcircles*, implementing the Hough transform, which does not allow the detection of circle-shaped structures smaller than a certain number of pixels.

### 3.3.4 SmRG algorithm vs Tree2Tree tools

The fidelity of the SmRG tracing process was also attempted using a tool considered a ground truth in the field of neuro-tracing. In particular, datasets (available on [http://viva-lab.ece.virginia.edu/suvadip\\_docs/Neuron/research\\_neuron.html](http://viva-lab.ece.virginia.edu/suvadip_docs/Neuron/research_neuron.html)) representing *Drosophila* neurons were analysed with both the SmRG algorithm and Tree2Tree tool, pur-

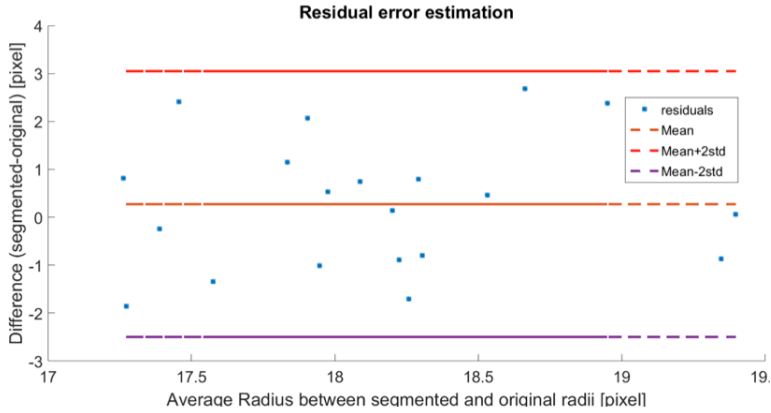


Figure 3.12: Residual error for  $n=20$  soma. The residuals are the difference between soma radii obtained by the SmRG algorithm and by Matlabs `imfindcircles` function.  
Maximum error: 14%

posely developed for these image stacks [23]. Note that the *Drosophila* fly has very few neurons ( $\sim 10^5$ ) with respect to mice ( $\sim 10^7$ ) and humans ( $\sim 10^{11}$ ), so they are simpler to discern than in the mouse. In any case, the reconstructions obtained with the SmRG and Tree2Tree are very similar (see Figure 3.13) in shape. Because of the different outputs of the SmRG algorithm and the Tree2Tree tool, the results (shown in Figure 3.13) can only be compared visually.

On the other hand, Tree2Tree tool did not provide a good quality of segmentation on the datasets representing Purkinje cells in clarified mouse cerebella, so they cannot be used for a further comparison.

### 3.4 Discussion

In this Chapter, the Smart Region Growing (SmRG) algorithm was presented, an innovative method for tracing neuron structures in their native

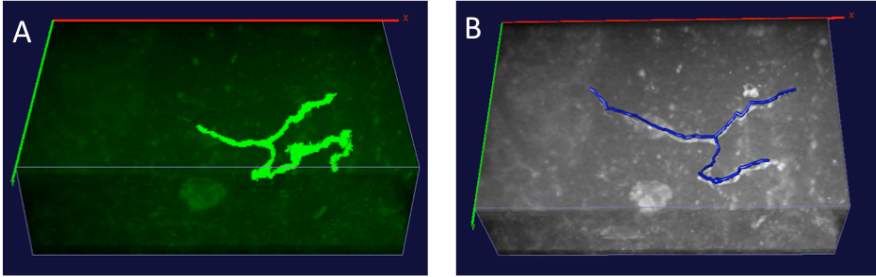


Figure 3.13: Fruit fly *Drosophila* neuron dataset, processed with (A) the SmRG algorithm and (B) Tree2Tree tool.

three-dimensional arrangement. Since the SmRG approach is based on local features of the image intensity value histogram to distinguish the signal (i.e. neurons) from the background, the algorithm is able to satisfactorily trace irregularly shapes neurons in confocal microscopy images. The algorithm works semi-automatically: in fact, the user has only to choose the soma radii range and the z-coordinate where there is at least one soma. After the soma identification, the algorithm is recursive, so it trace all the neurons using the soma center as initial seed. An example of the SmRG algorithm output is shown in Figure 3.6.

Preliminary results showed that the SmRG algorithm can isolate single neurons with their characteristic structure. Future developments should pursue an objective validation of the algorithm in order to test its accuracy. Moreover, an optimization of the confocal acquisition datasets is needed, in order to study the decrease in pixel intensity over sample depth and to improve the efficacy of the SmRG algorithm.

The strengths and limitations of the SmRG algorithm are detailed below:

**Strengths**

1. In contrast to most of the algorithms/tools in the literature, the SmRG algorithm can track neurons with lightly fragmented branches with irregularly shapes;
2. The SmRG algorithm is faster and computationally more efficient than others presented in the State of Art, with equal accuracy;
3. The SmRG algorithm does not return just the neuron skeleton, so it is more suitable to perform morphometric analysis than other tools (i.e. Neuron-GFP [33] or Tree2Tree [13] tools), since it allows the extraction of additional parameters (i.e. Neuron Surface-to-Volume ratio);
4. Since the SmRG algorithm works with a semi-automatic approach to trace neurons, it is also easy to use for non-expert users.

**Limitations**

1. Currently, the SmRG algorithm misses some tips/terminations of the neurites (see SmRG vs manual tracing Section), where the signal-to-noise ratio is too low;
2. An objective validation of the proposed approach is still lacking. Specifically, it was not possible to validate the results against other standard tools (i.e. Tree2Tree [13]), since they did not provide acceptable results on datasets representing L7GFP clarified cerebellar slices. Moreover, the manual tracing was not performed on the original confocal stacks, but on previously thresholded datasets;
3. The SmRG algorithm performance was tested only with two different confocal datasets, the L7GFP clarified murine slices representing Purkinje cells and the *Drosophila* brain datasets. While the

former represent an almost planar distribution of dendritic tree, as described in the literature [82], the latter do not represent a particular challenge due to their low density in the *Drosophila*.

The integration of the SmRG algorithm with tissue clearing techniques, as detailed in Chapter 2, may be helpful for the study of neurological diseases which are associated with neuronal disfunction at the micro-morphological level, such as Parkinson's [83, 84], Alzheimer [85, 86, 87, 88, 89], Huntington's disease [90, 91, 92] and Autism Spectrum Disorders [93, 43]. Moreover, it can be useful in order to simulate neuronal behaviour [94].

An other exciting application of the SmRG algorithm is the 3D printing of the segmented neuronal structures, to provide new approaches for understanding the nature and role of these intricate cells [95]. The use of 3D printing technologies in this field of neuro-imaging can be interesting for students, allowing them to see the full 3D structure, manipulate it, place neurons next to each other to compare structures and see how they overlap. An example of a neuron segmented with the SmRG algorithm and then 3D printed is shown in Figure 3.14.



*Figure 3.14: A Purkinje cell 3D-printed using a Stratasys Fortus 450mc (Stratasys)*



# Chapter 4

## N3MO: a NEuron MORphological analysis tool for 3D morphometrics

*"Software is like entropy. It is difficult to grasp,  
weighs nothing and obeys the Second Law of Thermodynamics:  
i.e. it always increases."*

*(N. R. Augustine)*

### **Abstract**

Morphometric analysis of cells in their own three-dimensional arrangement within the cortex (i.e. neuron and glia cells) is relevant for probing the link between micro-structural morphology and brain function, as well as for the investigation of degenerative diseases. As neural imaging techniques become ever more sophisticated, so does the amount and complexity of data generated. The 3D-NEuron MORphological analysis tool N3MO was purposely developed to handle and process confocal stacks

representing brain areas with neurons in their own three-dimensional arrangement, in order to trace single neurons, automatically run routines to extract the morphometric variables and store the data obtained. Here the software's main features were described, underlining the differences between N3MO and other commercial and open-source tools.

## 4.1 Introduction

It's well known that, even at the microstructural level, neuronal morphology is relevant for high level brain function [6, 96]. Morphometric analysis of neuron arborization structures could be of interest for:

- lifespan alterations in neural structure and neural organization over time during brain development, since the size of neuronal trees depends upon their state of maturation;
- neuronal morphological alterations related to diseases [97];
- morphological implications of neurons under experimental conditions. In fact, many conditions can induce changes in neuronal tree structures, such as learning, "enriched" environments, hormonal fluctuations and level of bioelectric activity.
- study of the structure-function relationship in dendritic trees.

For all these reasons, well-defined metrics are needed for assessing the morphological characteristics of neuronal branching patterns.

Classically, neuron morphology is investigated using stained and fixed dissociated cultures or slices [98, 99, 100]. Most investigators use imaging techniques such as confocal, 2-photon and super-resolution microscopy, and several reports describe neural growth dynamics using fluorophores such as tracker and calcium sensitive dyes [101, 102, 103]. Genetically

encoded probes are also becoming commonplace, and are an extremely useful tool for analysing neural cell morphology, although efforts are also dedicated towards cell signalling particularly at the synaptic level [104]. Several reports use techniques such as 2-photon or confocal microscopy on organotypic brain slices, which enable short term recordings of calcium dynamics through the use of  $\text{Ca}^{2+}$  specific dyes or very high magnification static analysis of dendritic spine distribution [105, 106].

As the spatial resolution of imaging techniques increases, so does the researcher's ability to generate huge quantities of data on neuronal morphometry. However, it is quite often time consuming and difficult to process image files and most of the digital image processing techniques, such as segmentation and features extraction, which have changed little over the past few decades, still require a large degree of pre-processing and image manipulation. Furthermore, the manual quantification of neuronal morphology is very labour-intensive and is prone to observer bias. Not only lack of consistency within an individual observer, but also variance between observers can reduce the level of reproducibility [35]. Computerized analyses of images can overcome the limitations and biases of human assessment.

Many open source or commercial tools have been implemented for automatically and consistently quantifying neuronal morphology through image processing. Most of the software described in the State of Art are designed for 2D images [35, 36, 37, 38, 39], but they cannot be exhaustive for the evaluation of brain micro-structure, since they do not provide information about the native three-dimensional arrangement of neurons. For this reason, in the last few years, different tools have been implemented for 3D metric feature extraction. However, it is not possible to perform complete morphological and automated analyses of a collection of stack images using a unique tool. Moreover, as far as data analysis is

concerned, most studies and software based methods which describe neuron morphometrics use very simple statistical tests (i.e. t-tests), which are often unsuitable for the study and classification of complex multivariate data.

To overcome these limitations, a novel user-friendly software, N3MO was developed, that integrates the SmRG algorithm for 3D neuron tracing, detailed in Chapter 3 with routines to perform morphometric analysis: image stacks from confocal imaging representing neurons can be processed and analysed with automatic data storage in the forms of matrices containing morphometric data. Subsequently, the matrices can be analysed, if is necessary, using 3-way Principal Component analysis (PCA), which enables the organization of multivariate datasets into group, thus facilitating the interpretation of complex and large groups of data.

In this Chapter, N3MO's features are illustrated. In addition, a comparison morphometric analysis was performed using N3MO and an open-source tool, as benchmark of precision.

## 4.2 N3MO development and implementation

N3MO is an open-source software developed in Matlab environment <sup>®</sup>(The MathWorks-sTM, Inc., Natick, Massachussets, USA). N3MO performs micro-structural and quantitative analysis from confocal image stacks representing neurons in their own arrangement within the brain. It has a user-friendly Graphical User Interface (GUI) environment with pull down menus for stack pre-processing, neuron 3D tracing quantitative morphological analysis, and, if needed, statistical analysis by 3-way PCA.

The tools and functions available in N3MO are summarized in Table 4.1

Table 4.1: Tools and functions implemented in N3MO.

Tools	Functions
<b>LOADING IMAGE STACKS</b>	
<i>Stack processing</i>	SmRG algorithm Skeletonization
<i>Morphological analysis</i>	Intersections Critical radius Maximum number of intersections Schoenen ramification index Regression coefficient for LogLog Sholl method Regression coefficient for SemiLog method Correlation coefficient for LogLog method Correlation coefficient for SemiLog method Determination ratio Maximum length vectors Minimum pathway Radial Extension Cone angle Soma Volume Soma Area-to-Volume Ratio Neuron Area-to-Volume Ratio Number of neurite branches Fractal Dimension
<i>3-way PCA</i>	Datamatrix Creation Multivariate analysis

## 4.3 N3MO: an outline

### 4.3.1 Loading an image stack in N3MO

In order to perform batch operations on different neurons, such as morphological analysis of all the cells belonging to a specific group (i.e. male wild-type mice), all the stacks were renamed with appropriate labels. N3MO, exploiting the concept previously implemented in NeMo [36], uses the properties indicated in the name to extract information about the neurons represented in a given stack. In particular, confocal image stacks have to be structured in the following way:

*FileType\_GroupNumber\_AnimalNumber\_SliceNumber*

where:

- *FileType*: "s" for original confocal image stack, in \*.tiff format;
- *GrupNumber*: progressive number identifying a group of interest;
- *AnimalNumber*: progressive number identifying an animal belonging to a specific group. This could be extremely important, i.e. to track the clinical patient history in *post-mortem* studies;
- *SliceNumber*: progressive number identifying the slice acquired or a particular region of the brain.

For example, s\_01\_02\_03 refers to a confocal stack of the second animal belonging to the first group (i.e. a particular mouse strain) and represents neurons of the third region of the brain (i.e. a particular region in the brain). Figure 4.1(A) shows an example of stack renaming. All the stacks from a single experiment are stored in the same folder for batch processing.

### 4.3.2 3D neuron Tracing with SmRG

Image stacks can be processed using the SmRG algorithm, described in Chapter 3. In particular, from the interface environment it is possible to load tiff stack datasets. The stack is visualized on the GUI and the user can scroll through the depth of the dataset in order to find a plane on which somata can be detected, as already detailed in Chapter 3 which describes the SmRG work-flow. The current displayed image corresponds to a certain depth in the sample (z-coordinate). If the current image displays at least one soma, circle-shaped structures can be detected automatically with the "Find seeds" button. The circles detected are automatically plotted on the current image. If the detection is satisfactory, the region growing can be initialized with the "Region Grow" button. This step takes a certain time depending on the number of initial seeds. With the display button it is possible to plot the 3D-segmented structures on new Matlabs figures, in order to examine the region growing result.

If the user is satisfied with the tracing, he/she can use the "Save:" button to store all the neurons segmented in the datamatrix structure. Alternatively, he/she can choose an other z-coordinate where the somata appear and run the "Find seeds" button again.

While 3D binary structures are well plotted in Matlab, 3D datasets like tiff-stacks cannot be visualized. For this reason, a "Merge and out" button was added to the GUI: with this button it is possible to create a new stack in which the segmented structure is highlighted within the original dataset. The visualization of the stack can be performed on ImageJ [1] or other software with a 3D viewer tool.

### 4.3.3 Datamatrix creation

Once an image stack has been loaded and all the neurons have been traced with the SmRG algorithm, an empty datamatrix structure, named as the

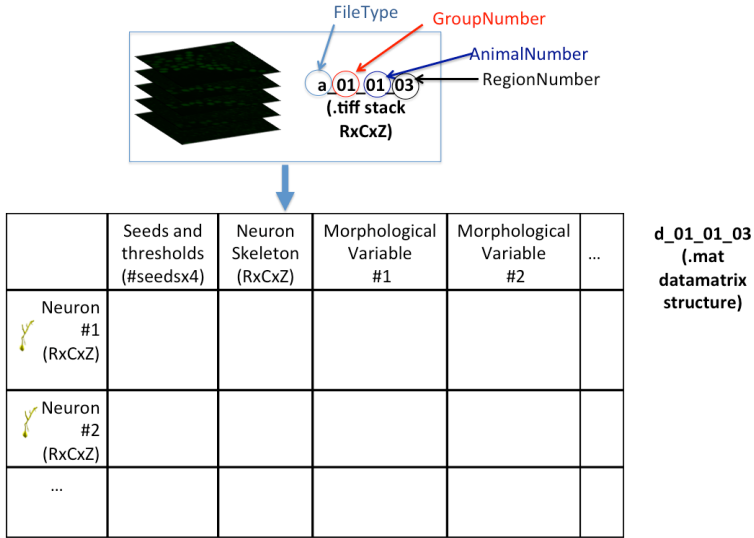


Figure 4.1: (A) Stack renaming and (B) respective datamatrix organization

confocal stack - unless the "d" - (see Figure 4.1(B)) is automatically created and saved in the same folder. It is used to save all the information of the image processing data generated in N3MO. In fact, the datamatrix is organized into  $N*(M+3)$  cells, where  $N$  is the number of neuron segmented in the specific confocal acquisition and  $M$  are the number of variables extracted for each neuron. Three more columns are automatically provided, to store: i) the neuron structure segmented with the SmRG algorithm ii) the three-dimensional coordinates of the voxel belonging to a specific neuron with the respective local threshold values, organized in a  $P*4$  matrix (where  $P$  is the number of voxels) and iii) the neuron skeleton (see Figure 4.1(B)).



### 4.3.4 Neuron Skeletonization

Prior to performing a morphometric analysis, segmented neurons are skeletonized. The skeleton reproduces cell structure, reduced to one pixel-thick. It must have two important characteristics:

1. It must faithfully reproduce the structure of the neuron
2. It must reduce soma to a single pixel, positioned at the centre of the soma.

The algorithm used has been already implemented in Matlab (<http://www.mathworks.com/matlabcentral/fileexchange/43400-skeleton3d>), inspired by Kerschnitzki et al. (2013) [107].

Figure 4.2 represents the algorithm output: the skeleton meets the specifications given, so it is suitable for the extraction of the morphological variables.

The skeletonized neurons are saved in a proper cell of the datamatrix structure as already detailed.

### 4.3.5 3D morphological analysis

Using N3MO, all the metrical features relevant for the the analysis of cell structure and morphology can be directly extracted. Once the neuron skeleton is obtained, the user can run the morphological analysis, which allows the derived metrical features to be investigated quantitatively.

The morphological variables were chosen from those generally adopted in the literature [108, 109], and divided in two groups, local and global variables. While the former variables are referred to the dendritic tree, the latter ones (i.e. radial extension, soma area and volume, cone angle and fractal dimension) are related to the whole neuron structure. A list of variables assessed with N3MO is given in Table 4.1.

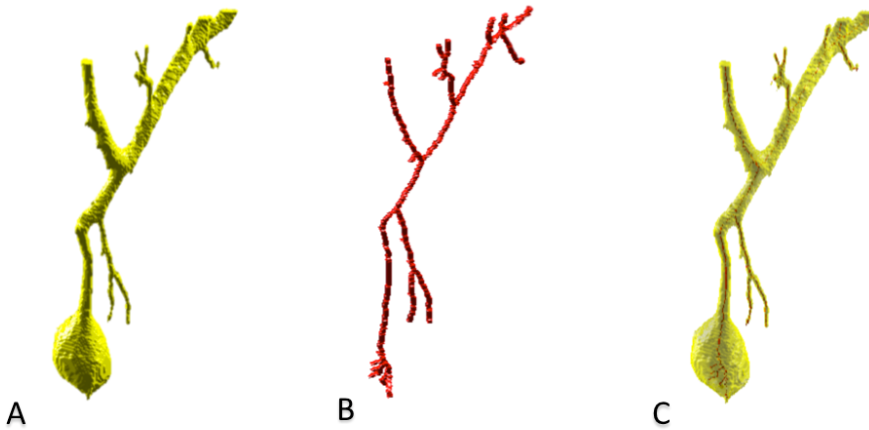
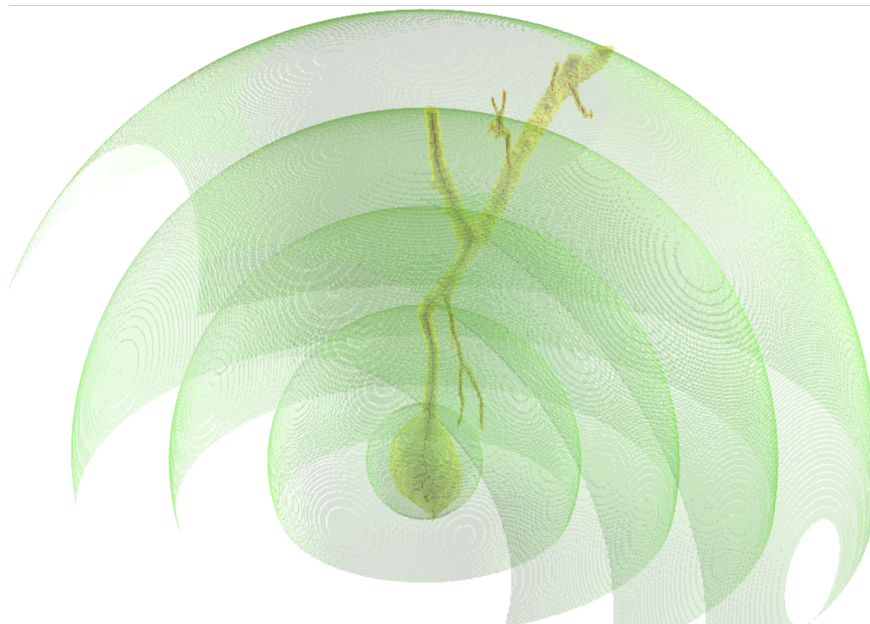


Figure 4.2: (A) An example of Purkinje neuron segmented with the SmRG algorithm, (B) its skeleton and (C) a merge of the two.

**Sholl analysis** The Sholl analysis is a method for quantitatively study of the radial distribution of the neural dendritic arborization pattern around the soma [110]. It allows dendritic geometry, ramification density and dendritic patterns to be evaluated and it is applied to binary structure representing the neuron skeleton.

In particular, following the Sholl method, each neuron skeleton is circumscribed by a coordinate system consisting of a series of concentric spheres centered on the soma, as shown in Figure 4.3. In N3MO, soma center coordinates are calculated using an automatic procedure: in particular, given a neuron, the algorithm firstly identifies a spheroid structure, which is likely to be the soma; then, the centroid of the spheroid obtained is calculated.

Two different coordinate systems were considered: one with a constant number of spheres (i.e. 10 spheres covering all the neuron volume) and the other with a constant inter-sphere distance, established as  $10 \mu\text{m}$ .



*Figure 4.3: An example of a Purkinje cell circumscribed by the coordinate spheric system, centered on the soma.*

The Sholl analysis can be applied in three different graphical modalities, as demonstrated by Milosevic and Ristanovic [111]:

1. *Linear Method*: The plot of the number of dendritic intersections calculated per intersecting sphere area, versus the sphere radius;
2. *Semi-Log Method*: The plot of the logarithm of the number of dendritic intersections per intersecting sphere area, versus the sphere radius;
3. *Log-Log Method*: The plot of the logarithm of the number of dendritic intersections per intersecting sphere area, versus the logarithm of sphere radius;

As demonstrated by Sholl [110] for 2D images representing neurons, at least in the Semi-Log or Log-Log method, a linear behaviour is apparent. The method which better approximates a straight line provides relevant clues about the dendritic structure.

The linear method is characterized by:

- $R_c$  (*critical radius*): the radius of the sphere with the maximum number of intersections;
- $N_m$ : Maximum number of intersections;
- *Schoenen ramification index*: Quotient of the maximum number of intersections and the number of primary dendrites of the neurons (i.e. the branches directly arising from the soma).

On the other hand, the Semi-Log and the Log-Log Method are characterized by:

- $k_{SL}$  (*Semi-Log Sholl regression coefficient*): Slope of the fitted straight line in the semi-log plot. It measures the decay rate of intersection numbers versus the distance from the soma;
- $k_{LL}$  (*Log-Log Sholl regression coefficient*): Slope of the fitted straight line in the Log-Log plot. It measures the decay rate of intersection number versus the distance of the soma;
- $R_{SL}$  (*Semi-Log correlation coefficient*): Degree of data correlation in Semi-Log method;
- $R_{LL}$  (*Log-Log correlation coefficient*): Degree of data correlation in Log-Log method;
- $\Delta$  (*determination ratio*): It is defined as in equation 4.1:



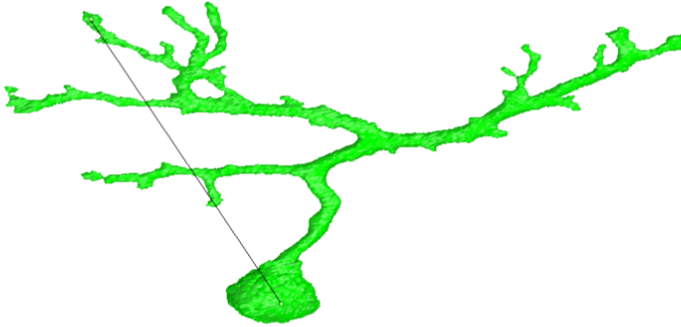
Figure 4.4: Minimum length vectors for a Purkinje cell.

$$\Delta = \frac{(R_{SL})^2}{(R_{LL})^2} \quad (4.1)$$

and it allows appropriate graphical method to be determined. In fact, if  $\Delta < 1$ , the Log-Log Method is preferred, while if  $\Delta > 1$  the Semi-Log method is better.

From the intersections obtained with the Sholl analysis, other variables can be evaluated:

- *Minimum length vectors*, extracted by evaluating the minimum Euclidean distance between the cell intersections on two adjacent spheres (see Figure 4.4);
- *Minimum pathway*: measured as the sum of the magnitudes of the minimum length vectors.



*Figure 4.5: Radial extension of a Purkinje cell.*

#### 4.3.6 Global 3D morphometric parameters

Besides the Sholl analysis, other morphometric variables relative to the neuron can be calculated:

**Radial Extension ( $E$ )** In order to evaluate cell dimensions, the radial extension of the cells can be assessed as the Euclidean Distance from the soma center to the furthest pixel of the cell skeleton, as shown in Figure 4.5. The axis connecting the soma center to the furthest pixel of the cell skeleton is called "principal axis".

**Cone Angle ( $C_a$ )** In order to characterize the neuron extension in the 3D space, the cone angle in which the cell is contained can be automatically extracted. Firstly, the neuron is automatically rotated in the 3D space in order to align the principal axis to  $z$ . Then, a cone, whose apex corresponds to the soma center, previously calculated (see Section 4.3.5), is automatically circumscribed to the neuron.

If the cell is uniformly extended, the cone angle is automatically fixed as  $360^\circ$ .

**Neuron Surface-to-Volume Ratio** Since objects with irregularity have larger surface area for a given volume than regular ones, the Neuron Surface-to-Volume ratio can be used as a raw index of neuron complexity.

**Soma Volume** to quantify soma size, since they seems to change in different neuro-pathological conditions [112, 113, 114].

**Soma Surface-to-Volume Ratio** For a given volume, the object with the smallest surface area (and therefore with the smallest Surface-to-Volume ratio) is the sphere. For this reason, the Soma Surface-to-Volume Ratio was implemented as an index of soma shape.

**Number of neurite branches** considered a further index of neuron complexity [115].

**Fractal Dimension** Fractal dimension is a measure of a feature common to several biological systems, their fractal nature or complexity. An object is fractal if it expresses the property of self-similarity: it is made up of copies of itself at different scales. As argued in several studies, neurons can be represented as fractal or space-filling objects and the fractal dimension represents an important parameter for the characterization of the dendritic structure [116, 117, 118, 119]. In fact, one of the advantages of using fractal analysis (i.e. fractal dimension) is its capacity of differentiate between cells that differ in complexity of their branching patterns. In addition, the fractal dimension is of relevance for intra- and inter-species comparisons of neuronal population [120].

There are several methods to evaluate the fractal dimension; in N3MO,

the box-counting method was used as described in Jelinek and Fernandez [118]. In this method, the segmented neuron is inscribed in a cube of size  $r$ . The size  $r$  of the cube is initially equal to the image stack size and is progressively decreased, while the number of non-empty cubes,  $N(r)$ , is counted. A plot of  $\log(n)$  versus  $n$  is obtained, which can be fitted with a straight line, of slope  $S$ , where  $S$  is an estimation of the fractal dimension ( $F_d$ ):

$$F_d = S \tag{4.2}$$

While a mathematical fractal requires infinite orders of magnitude of power-law scaling and therefore is fractal over all scales, physical, biological and other structures in nature are fractal over a relatively small range [121].

#### 4.3.7 Multivariate analysis

N3MO allows user to perform statistical analysis through the three-way Principal Component Analysis (PCA) multivariate technique [122], operating on the datamatrix. Three-way PCA technique is a generalization of PCA, a popular technique that is often used for the exploratory analysis of a set of variables. While PCA analyses data varying in two dimensions, three-way PCA allows the analysis of sets of variables associated with three-way data sets, the so-called modes: the variables (i.e. the morphological parameters extracted with N3MO), the objects (i.e. the neurons traced) and the conditions (i.e. neurons belonging to mice sacrificed in different time-points). This technique is aimed at transforming data so as to summarize the associated information in a small number of novel variables or principal components able to express as much information as possible. Several models and algorithms implement the three-way PCA methodology [123]. In N3MO the Tucker3 model was implemented, as



described by Leardi et al. [122] and already implemented in NeMo [36]. Briefly, data are firstly pre-processed in order to remove scaling and standardization offsets, then the number of components can be chosen. To obtain principal components the covariance matrix of data is decomposed in a eigenvectors matrix and a eigenvalues matrix. Eigenvectors are the columns of the rotational matrix that is transposed and multiplied for the datamatrix. The multiplication result is the principal components matrix (mathematically it corresponds to performing a series of orthogonal rotations on a cubic core array,  $G$ , expressing the correlations between the data from the “datamatrix” denoted by objects, variables and conditions planes. The orthogonal rotations are iterated until a body-diagonal common orientation is reached). The minimum number of components is selected on the basis of an optimized data fitting and stability and interpretability criteria such that data variance is maximized. In fact, only a small number of principal components are chosen and they constitutes the axes of the plots in which data are reported.

The final transformation is given by the following equation 4.3:

$$x_{ijk} \cong \sum_{p=1}^P \sum_{q=1}^Q \sum_{r=1}^R a_{ip} b_{jq} c_{kr} g_{pqr} \quad (4.3)$$

where  $x_{ijk}$  are the elements of the original datamatrix, while  $a_{ip}$ ,  $b_{jq}$ ,  $c_{kr}$  and  $g_{pqr}$  are the elements of the matrices A, B, C and G. G is the core efficiency describing the main relations in the data. The component matrices A, B, and C describe how the particular subjects, variables and conditions are related to their associated components. The three data modes are plotted in three different graphs whose axes represent the principal components. The meaning of the principal components requires careful interpretation and analysis. Typically after the PCA analysis, objects, variables and conditions are represented in a two-axes plot and

correlations between the two axes and the parameters can be deduced by an analysis of the plots. Each parameter has a specific coordinate according to the weight it bears with respect to the axis. If the coordinate is near 0, then the weight is small, if it is greater or less than 0, the weight is high.

## 4.4 N3MO vs ImageJ [1]

N3MO performance were tested comparing its outputs with those obtained using ImageJ [1]. In particular, the Sholl analysis was performed using both N3MO dedicated routines and an ImageJ plug-in [3] on two different kind of neurons, traced with the SmRG algorithm detailed in 3:

1. Purkinje cells from mouse cerebella optimally clarified as detailed in Chapter 2;
2. *Drosophila* neuron confocal datasets available at [http://viva-lab.ece.virginia.edu/suvadip\\_docs/Neuron/research\\_neuron.html](http://viva-lab.ece.virginia.edu/suvadip_docs/Neuron/research_neuron.html).

The process was faster with N3MO due to the automatic identification of the soma center coordinates and the automatic generation of the spheres. The Sholl parameters measured were similar: in fact, no significant or systematic differences between the two tools were detected. An example of the Sholl analysis outputs for a Purkinje cell and a *Drosophila* neuron is provided in Table 6.1.

## 4.5 Discussion

Morphometric analyses are relevant for the study of alterations in the dendritic/axonal field of neurons or neuronal morphological correlates of diseases [124], as well as the morphological implications of neurons under

Table 4.2: Comparative Sholl analysis using N3MO and the ImageJ plug-in [3]

Purkinje cell from L7GFP mouse			Neuron from Drosophila fruitfly		
Radii ( $\mu\text{m}$ )	N3MO	ImageJ	Radii ( $\mu\text{m}$ )	N3MO	ImageJ
47.43	1	1	0.26	3	3
69.02	1	1	2.34	3	3
90.62	2	2	4.42	3	3
112.72	1	1	6.50	4	3
133.82	3	1	8.58	3	2
155.42	5	1	10.92	1	1
177.02	3	2	13	1	1
198.62	4	4	15.98	2	1
220.21	4	4	17.16	2	2
241.81	2	2	19.50	1	1

experimental conditions or the structure-function relationships in dendritic trees [6, 97, 96]. Moreover, morphological features such as neuron shape, size and branching can elucidate the functional role of different neurons.

In order to analyse microscopic alterations over time in brain tissue slices, it is important to have accurate, reliable and reproducible measurements, which are not prone to human bias. Given that current imaging methods are able to provide high-resolution data, in the last 20 years several commercial and open-source tools for morphological analysis and extraction of quantitative information on neuron in their own native arrangement within the brain cortex have been developed. Table 4.3 lists the features of the principal software available for micro-structural and morphological analysis. From the Table it is clear that not all the software are capable of a complete and exhaustive analysis: in fact, some tools are not dedicated to neuron tracing, or able to extract only few morphological parameters. Furthermore, many routine operations require significant manual intervention and interpretation, such as the 3D tracing of each branch of the neurons with a pencil tool or mouse. In fact, most software do not implement automated or semi-automated 3D neuron tracing. Many of the available tools focus on the analysis of single parameters and many routine operations require significant manual intervention and interpretation. For example, in NeuroLucida (MicroBrightField, Williston, VT) [31], a commercial software for morphometric analysis of neuros used successfully by several investigators [125], the user must trace each neuron branch with a pencil tool or mouse. Moreover, some of the tools are not open-source, so that is impossible to customize them for one's own purpose. Finally, some software require a commercial licence and may be out of reach for neuroscientists in developing and emerging countries.

Table 4.3: Characteristics of the principal software for neuron morphological analysis

	Neurite Tracer	Sholl Analysis	Fractal Dimension	Soma Area & Volume	Neurite Length	Multivariate Analysis	Neuron Area & Volume	<b>PROS</b>	<b>CONS</b>
	<i>NEUROLUCIDA</i> [31]	Yes	Yes	No	No	Yes	No	Accurate	Not Free; Only Windows
	<i>NEURITE TRACER</i> [126]	Yes	No	No	No	Yes	No	Automated; Free	No full analysis
	<i>SHOLL ANALYSIS</i> [110]	No	Yes	No	No	No	No	Automated; Free	No full analysis
IMAGEJ	<i>FRACTAL DIMENSION (BoneJ)</i> [127]	No	No	Yes	No	No	No	Automated; Free	No full analysis
	<i>Macro in METAMORPH</i> [41]	No	Yes	No	Yes	No	No	Accurate	Not free
	<i>IMARIS software</i>	No	No	No	No	Yes	No	4D real time data visualization and analysis	Not specific for neurons
	<i>SAMA</i> [42]	No	No	Yes	Yes	Yes	No	4D real time data visualization and analysis	Not specific for neurons
	<i>TREE toolbox</i> [128]	Yes	No	No	No	Yes	No	good neurite reconstruction	No full analysis
	<i>NEURONSTUDIO</i> [40]	No	Yes	No	No	Yes	No	Free	No full analysis
	<i>N3MO</i>	Yes	Yes	Yes	Yes	Yes	Yes	Free; Accurate; Multi-variate analysis	Preliminary folder organization

## 4.6 Conclusion

During this PhD thesis, N3MO, an open-source software provided with all the tools that can be useful for the analysis of neuron morphology in their own tree-dimensional arrangement, was developed. It consists of a set of computation algorithms written in Matlab and implemented in a GUI framework, in which it is easy to trace neurons, extract morphological features of interest and access the data to have a global view of the results. With respect to the other software, listed in Table 4.3, its unique features are the possibility to perform a complete morphological analysis and the use of the 3-way PCA for data analysis and classification. With the other tools, image stacks need to be opened one at a time, traced and then data are collected and saved separately: when dealing with a given stacks representing different neurons, the procedure takes a considerable amount of effort. On the other hand, N3MO allows all the morphological features of interest to be obtained in a single operation. The 3-way PCA can be used to unravel correlations between significant morphometric variables in neurons and for the classification of cells according to their morphology.

N3MO was developed during the course of this thesis because it is an alternative and novel open-source software for the morphometric characterization and classification of neurons which preserve their native three-dimensional arrangement within the brain. The software was developed as there are currently no tools available for handling and processing large quantities of data on single neurons. N3MO could be of interest and use to neuroscientists involved in morphometric quantification and advanced statistical analyses of neurons in their own three-dimensional arrangement within the brain.

# Chapter 5

## Study of sexual dimorphism in murine models of autism

*"Stupid is as stupid does"*

*(F. Gump)*

### **Abstract**

In this Chapter, the characterization of Purkinje cells micro-structure in murine models of autism is described. Due to unbalanced incidence between males and females in the the Autism Spectrum Disorders, the sexual dimorphism was also taken into account. Firstly, a proof of concept on 2D images representing Purkinje cells in thin cerebellum slices was performed, demonstrating that there are statistically relevant morphological and topological differences between both sexed wild-type mice and knock-out ones. However, two-dimensional images cannot give information about the native arrangement of the neurons within the brain. For this reason, the work-flow detailed in Chapters 2, 3 and 4 in this PhD

thesis was applied to study morphological alterations in Purkinje cells in their own arrangement within the cerebellum using thick slices from both males and females in a murine model of autism, comparing the results with wild-type mice.

## **5.1 A survey on the Autism Spectrum Disorders**

Autism spectrum disorders (ASDs) comprises a collection of heterogeneous neuro-developmental diseases (American Psychiatric Association, 2013), initially described by Kanner in 1943 [129]. By definition, symptoms are manifested by 36 months of age and are characterized by delayed and disordered language, impaired social interaction, abnormal responses to sensory stimuli, events and objects, poor eye contact, an insistence on sameness, an unusual capacity for rote memory, repetitive and stereotypic behaviour and a normal physical appearance [130]. The aetiology of the pathology is complex: genetics, environmental factors, and specific gene-environment interactions are thought to contribute to the pathogenesis of ASD [131]. In fact, autism differs from person to person in severity and combinations of symptoms and several hundreds of genetic variants have been identified [132].

### **5.1.1 The cerebellum and the ASDs**

In the last couple of decades, relatively few neuro-pathological studies have been performed on the brains of autistic subjects. Of those reported, most of the abnormalities have been described in the cerebellum. The mammalian cerebellum comprises more than half of the neurons in the central nervous system, but has only about one-ninth of the volume of the neocortex: it is therefore a very compact structure that poses several problems in terms of accurate structural and functional imaging [133].



The cerebellum has historically been implicated in motor coordination; however, recent findings show that it is also involved in several non-motor functions [134] and has a role in nearly as many separate functions as the neocortex. Like the neocortex, the cerebellar cortex is elaborately folded; there are well-defined lobules and sub-lobules, which are separated by a number of fissures that can be reliably identified across individuals and species. In addition, each lobule display a specific pattern of connectivity with the cortex [135] and is likely associated in its functional role [134]. Finally, like the cerebral cortex, the cerebellar cortex displays a highly ordered and layered structure.

Maybe the most interesting neurons of the cerebellum, both for their elaborate dendritic structure and their role in cerebellum development and function, are the Purkinje cells (PCs). PCs represent the only output of the cerebellar cortex. Moreover, they are involved in the first stage of cerebellar development and it has been suggested that PC electrophysiological and morphological properties may influence the growth and connections of cells which develop successively [136]. In this light, it is clear why the study of PCs is important to understand how they influence the connectivity of the mammalian cerebellum.

Several studies describe PC micro-structural morphology in great detail [82, 100, 137, 138]. The most common methods employed for the analysis of micro-scale neuronal structure are based on optical imaging of *in vitro* PC cultures [36, 139]: in fact, optical images can be analysed with computational methods to quantitatively measure and assess morphological characteristics of neuronal branching patterns [108]. Moreover, several reports describe neural growth dynamics and network organization using specific fluorophores detected with fluorescence microscopy [101, 102, 140]. The limitation of these kind of studies is the use of *in vitro* cultures, which presuppose the assumption of planarity of the PCs.

Although this hypothesis is essentially verified, this kind of study does not allow the evaluation of PCs morphology related to their interactions with the other cells within the cerebellar cortex, in an arrangement close to that *in-vivo*.

As regard the Autism Spectrum Disorders, several studies show abnormalities within the cerebellum: Baumann and Kemper reported a reduction of granular cells and an increase of dimensions of deep cerebellar nuclei neurons [130]. In terms of cerebellar sub-regions, reduced size of one or more regions in the cerebellar vermis, which is predominantly grey matter, is frequently reported in autism MRI studies: Courchesne observed a localised reduction in the size of cerebellar vermis lobule VI-VII, sometimes associated with a reduced size of cerebellar hemispheres, apparently proportionally correlated to the seriousness of the disease [141]. Baumann and Kemper also showed other abnormalities in cerebellum of children and adults in ASDs: a significant decrease in the number of PCs, primarily affecting the postero-lateral neo-cerebellar cortex and adjacent archi-cerebellar cortex of the cerebella hemispheres [130]. On the other hand, Fatemi and colleagues showed that in addition to a reduction of PC number there is also a reduction of their dimensions while density is the same [43]: since PC exhibit excitatory stimuli from the deep cerebellar nucleus, a reduction of their number and dimension cause an abnormal over-connectivity along the cerebellum-thalamus-cortex circuitry.

### **5.1.2 The importance of murine models for the study of neurological disorders and od ASDs**

Despite the decades of research, the aetiology of most of the developmental disorders remains elusive. Thus, it is important to pursue all avenues, in attempting to understand them. Nowadays, much of our current un-

derstanding of the cellular and molecular mechanisms governing neural development and disease derives from animal models [142]. In fact, animals are often used in this kind of research when there is a need to find out what happens in the whole, living body, which is far more complex than the sum of its parts. In addition, humans and animals share hundreds of illnesses, and consequently animals can act as models for the study of human illness [143]. From such models researchers can learn how a given disease affects the body, how the immune system responds, who will be affected, and more.

The most significant contributor to the neuroscience research has been the development of transgenic mouse models. The use of transgenic animals has allowed neuroscientists to decipher the function of particular genes and to create disease models.

As regards neuro-developmental disorders, such as Autism Spectrum Disorders (ASD), there are behavioural characteristics that can be established in animal models. Although the exact nature of the possible environmental contributions remains quite speculative, there is a large body of evidence that indicates that there is a strong genetic component to ASD, since the first epidemiological study on affected twins [144].

Given the multi-factory of aetiology of ASDs, there is no single animal model that captures all the molecular, cellular or behavioural features of ASDs. In this thesis, two genes known to have important functions in cerebellar development were investigated [145]: the reelin (RELN) and the Engrailed-2 (EN2) ones.

**REELER mice and their importance for ASDs** Reelin is one of the molecules that are under examination as a risk factor in autism. It is a protein of the extracellular matrix, with a key role in migration and positioning of neurons [146, 147, 148, 149, 150] .

Reelin was named after the Reeler mutation that arose spontaneously in

mouse, showing autosomic recessive transmission [151]. The homozygous recessive Reeler mouse completely lacks the protein and displays a typical cerebellar phenotype from which it derived its name, characterized by dystonia, ataxia, and tremor. Histologically, these animals have severe alterations in the architecture of the laminar structures of the brain [152, 153, 154] and less clear alterations in other Central Nervous System areas. The mutated gene (*reln*) was discovered by D'Arcangelo et al. [155]; soon after [156], it was discovered that the gene is highly conserved between mice (*reln*) and humans (*RELN*). Then, an autosomal recessive form of lissencephaly (LCH) was described in humans [157] to be associated with two independent mutations in *RELN*. LCH phenotypically demonstrated severe abnormalities of the cerebellum, hippocampus and brain-stem, uncovering an obvious parallelism with the Reeler mutation (*reln* -/-). While *reln* -/- mouse brain has been extensively characterized in structural and functional terms, the heterozygous Reeler mice (*reln* +/-) appear phenotypically normal, but have attracted the interest of neurologists as an animal model for some psychiatric disorders when it was discovered at autopsy that *RELN* is 50 % down-regulated in the brain of psychotic individuals [158, 159], in particular in autism [11, 160]. Notably, cerebral abnormalities observed in the psychotic human brain [11, 43, 160] are similar to those in *reln* +/- mice that include a reduction in glutamic acid decarboxylase 67 (*GAD67*), dendritic arbors and spine density in cortex and hippocampus, and alterations in synaptic function including long-term potentiation [161, 162]. However, the behavioural abnormalities in these mice are subtle and controversial [163, 164, 165]. Few structural studies have focused on the cerebellum of *reln* +/- mice. Heterozygous mice have been reported to show a progressive loss of PCs in the first weeks of life [166], and lower numbers of these neurons were described in a parallel study on psychotic patients and adult *reln* +/- mice

[167]. Notably, it has also been previously shown that PCs in autistic patients have a reduced size in comparison with normal subjects [43].

**Engrailed2 mice: a window into autism** Many mouse mutant models show Purkinje cell deficits, although Engrailed 2 (En2) has been of particular interest for several reasons [168]. In fact, En2 deletion or over-expression produces Purkinje cell deficits; moreover, the diminished posterior cerebellar vermis and lobules in mice are also seen in some human autism neuropathologies, and human En2 localizes close to chromosomal 7 region identified by several ASDs genome linkage scans. Studies on En2 gene over-expression [169, 170] as well as gene deletion have been performed both *in vivo* and *in vitro* [44, 171]. Over-expression of En2 in neural precursors in culture maintains precursor proliferation and reduces neuronal differentiation, mechanisms that could conceivably contribute to ASD cerebellar neuropathology. Both En2 knock-outs and transgenic mice that cause the misexpression of the gene have been generated. Deficits in social behaviour were reported in En2 +/- mice across maturation that included decreased play, reduced social sniffing and allogrooming as well as less aggressive behaviour. Deficits in two spatial learning and memory tasks were also obtained [172]. Adult mice for both mutants are non-ataxic, but their cerebella are hypoplastic, with a reduction in the number of Purkinje neurons and other cortical neurons [44, 45].

This findings correlates with a quantitative study of PCs in culture obtained from En2 +/- mice and wild-type (WT) control mice, performed using NEMO, a tool for the extraction of quantitative morphometrics from microscopy images, which demonstrated that PCs are consistently smaller, less arborized and die earlier than WT ones [36].

### 5.1.3 Sexual Dimorphism in the brain and in ASDs

Although it is well known that specific regions of the brain exhibit sexual dimorphism in a large number of species, ranging from invertebrates to mammals, including humans [173, 174, 175, 176, 177, 178, 179, 180, 181], the functional impact of sex as a basic biologic variable is little understood. Gender bias has also been repeatedly observed in neurodevelopmental and neuro-degenerative disorders, such as ASDs [182], Alzheimer's and Parkinson's [183], including neuropsychiatric disorders, anxiety and depression [184, 185].

In this light, it is important to identify the anatomical differences in male and female brains producing detailed maps and accurate representation of sexual dimorphic areas of mammals. On the other hand, studies on sex differences in sociability have been conducted in order to ascertain whether the sexual dimorphism is a result of biological or socio-cultural differences between the two sexes. In 2000, Connellan et al. [186] studied 102 human neonates, who by definition have not yet been influenced by social and cultural factors, to see if there was a difference in looking time at a face (social object) and a mobile (physical-mechanical object). Their results showed that male infants were strongly interested in the physical-mechanical mobile while the female infants showed a stronger interest in the face.

One of the most well-established facts about autism is that it occurs with much greater frequency in males than in females [187]: various studies have come up with men/women ratios ranging from 2:1 to 16:1. Despite the plethora of studies performed, the nature and meaning of sex differences in the ASDs is still enigmatic. In the last few decades, three main explanations for this unbalanced incidence have been theorized:

1. **Exaggeration of normal gender differences:** This theory is

based on evidence that, in the general population, women and girls have better verbal skills, while men and boys excel in visuo-spatial tasks [187]. There may be a neurological basis for this, so that autism can be interpreted as exaggeration of “normal” sex differences. On the other hand, environmental and social factors may also play a part in differences in ability across men and boys, and women and girls. This means that no direct analogy can be drawn between the poorer verbal skills of boys and the higher incidence of autism in men and boys.

This interesting theory informally suggested for the first time in 1944 by Hans Asperger: *“The autistic personality is an extreme variant of male intelligence. Even within the normal variation, we find typical sex differences in intelligence. In the autistic individual, the male pattern is exaggerated to extreme.”* In support of this theory, Rimland also pointed out that men and boys tend to be more susceptible to organic damage than women and girls, whether through hereditary disease, acquired infection or other conditions. Since it is now almost universally accepted that there is an organic cause for autism, it should therefore not be surprising that men and boys are more vulnerable to it than girls and women [188]. Later, Baron Cohen has developed an “extreme male brain” theory of autism [189]. This relates to thinking about sex differences in general within the dimensions of “empathising” and “systemising” and autism as an extreme of the male ‘systemising’ dimension. This theory has been powerful in shaping public perception of the condition.

2. **Genetic explanation:** According to this theory, there is a genetic explanation to the gender split observed in the ASDs. Skuse [190] has suggested that gene or genes for autism are located on the X

chromosome. Girls inherit chromosomes from both parents, but boys inherit one, from their mothers. Skuse's hypothesis is that the X chromosome which girls inherit from their fathers contains an imprinted gene which protects the carrier from autism, thus making girls less likely to develop the condition than boys. Lord and Schopler [191] have outlined several possible mechanisms for the transmission of autism on the sex-linked X chromosome, and also for autosomal transmission. However, these are merely theoretical models and in fact researchers are still a long way from identifying a simple genetic cause for autism. It is likely that several genes on different chromosomes will be found to be associated with autism. In this light, Skuse's theory may not represent the full picture. In 2014, Jacquemont et al. [192], investigated molecular characteristics associated with the increased male-to-female ratio in individuals referred for neurological disorders. Their findings show that females systematically carry more neuro-developmentally deleterious variants than do males any time that individuals are ascertained for neurological disorders or are parents of a proband referred for those symptoms.

3. **Wrong diagnosis criteria:** Leo Kanner's 1943 study of a small group of children with autism there were four times as many boys as girls [129]. Hans Asperger thought no women or girls were affected by the syndrome he described in Autistic psychopathy in childhood, although clinical evidence later caused him to revise this thinking [193]. On the other hand, Brugha found that 1.8% of men and boys in England had a diagnosis of autism, compared to 0.2% of women and girls [194]. Attwood (2000) [195], Ehlers and Gillberg (1993) [196] and Wing (1981) [187] have all speculated that many girls with Asperger syndrome are never referred for diagnosis, and so are



simply missing from statistics. Lorna Wing found in her paper on sex ratios in early childhood autism that among people with 'high-functioning autism' or Asperger syndrome there were as many as 15 times as many men and boys as women and girls, while in people with learning difficulties as well as autism the ratio of men and boys to women and girls was closer to 2:1 [187]. Women and girls with Asperger syndrome may be better at masking their difficulties in order to fit in with their peers and have a more even profile of social skills in general. Different studies speculated that many women and girls with Asperger syndrome are never referred for diagnosis, and so are simply missing from statistics, even though they are equally in need of diagnosis and support [187, 195, 196]. This might be because the diagnostic criteria for Asperger syndrome are based on the behavioural characteristics of men and boys, who are often more noticeably "different" than women and girls with the same underlying deficits. Gould and Ashton-Smith theorized that because women and girls on the autism spectrum may present differently from men and boys, diagnostic questions should be altered to identify some women and girls with autism who might otherwise be missed [197].

Different centres for the study of ASDs are focusing on the different manifestations of behaviour in autism as seen in women and girls compared with men and boys. In particular, the National Autistic Society's Lorna Wing Centre for Autism has registered a steady increase in the number of women and girls referred for diagnosis, which suggests an historic bias towards men and boys in the diagnostic criteria for autism.

It is clear that the results collected are still inconsistent and confused. In particular, two difficulties quickly become apparent when one

tries to move beyond the sex difference in the incidence of autism to its neuro-biological implications. First, the theoretical links between sex differences, possible aetiology, and organic mechanisms underlying autism are far from straightforward. While there have been numerous failures to confirm specific hypotheses, few positive findings have emerged. Because of small sample sizes, non-epidemiological samples, and difficulties in balancing factors such as sex and degree of mental retardation within autism, negative findings cannot be taken as conclusive [191].

Unravelling the sexual bias in autistic patients could be important in order to design more efficient diagnostic and therapeutic approaches.

Since mice and rats display sexual dimorphism features of their cerebella, similar to humans [198], the study of mouse models of ASD, whose alterations mostly affect cerebellar area, could be of interest to ascertain the effect of gender on the autistic phenotype. This Chapter described the quantitative characterization of alterations in PC morphology in murine models of autism. As ASDs seem to affect males more than females, both sexed mice were considered. The study was conducted in two steps: firstly, a quantitative estimation of soma areas and degree of alignment of CPC along the cerebellar cortex of PCs in normal and *reln* haplo-deficient mice of both sexes was performed, using standard protocols for tissue harvesting, acquisition and processing. Having taken into account the aforementioned heterogeneity of the cerebellar function, the analysis was carried out in five vermal lobules that -in humans- specifically intervene in the processing of different types of functional inputs [199]: the central lobule and culmen (sensory-motor), the tuber (cognitive), the uvula (default mode network) and the nodulus (emotive/vestibular). After that, since the analysis on 2D images is limited and it cannot fully describe PC morphology, the work-flow designed in this thesis (and detailed in Chapters 2, 3 and 4) was applied to the *Engrailed2* murine model of autism, to

characterize PC structure in their native arrangement within the cerebellar cortex, focusing again on morphological abnormalities between males and females.

## 5.2 Sexual dimorphism in REELER model of autism: a proof of concept

### 5.2.1 Materials and Methods

**Tissue preparation and imaging** Studies were performed on twenty-four young adult mice (2 months) of both sexes and different reln genetic backgrounds (reln +/- and WT). Animals were hybrids generated at the Department of Veterinary Medicine of the University of Turin by crossing reln +/- and WT mice with L7GFP WT mice that express the green fluorescent protein (GFP) under the control of the L7 promoter [60], as already detailed in Chapter 2.

The number of animals was kept to a minimum and all efforts were made to minimize their suffering. All experiments were authorized by the Italian Ministry of Health and the Bioethics Committee of the University of Turin. Animal procedures were carried out according to the guidelines and recommendations of the European Union (Directive 2010/63/UE) as implemented by current Italian regulations on animal welfare (DL n. 26-04/03/2014). Before being used in this study, all animals were sexed and genotyped by routine methods to ascertain GFP expression and their appropriate reln genetic background [155].

After deep pentobarbital anesthesia, mice were perfused with 4% PFA in 0.1 M phosphate buffer saline (PBS), pH 7.4-7.6. Following several washes in PBS, the cerebellar vermis was isolated from the remaining parts of the brain, cryoprotected in 30% sucrose, frozen in liquid nitrogen and serially cut in 7  $\mu$ m parasagittal sections. Randomly chosen sections

from series were collected at 100  $\mu\text{M}$  distance along the transverse axis of the vermis, attached on slides and mounted in fluorescence-free medium. For each animal, four to five sections of the entire vermis were observed at a 20x magnification (pixel size: 0.46  $\mu\text{m}/\text{pixel}$ ) with a transmitted fluorescence light microscope (DM6000B, Leica, Germany). For each cerebellum region, i=4-5 images (1392x1040 pixel) of the GFP-tagged PNs from the central lobule (II-III), culmen (IV-V), tuber (VIIb), uvula (IX), and nodulus (X) were acquired and subjected to analysis, as summarized in Figure 5.1(A).

**Image processing and analysis** For all the images acquired, three morphological variables were extracted, using two different software:

1. **Feret's diameter**, which is the longest distance between any two points along the object perimeter. This is a step necessary for the evaluation of the misalignment along the YZ axis;
2. **Soma Area**;
3. **Misalignment along the YZ axis (dorso-ventral)**

While the first two parameters were calculated using the ImageJ software [1], the latter was obtained with NEMO (NEuron MORphological analysis tool), a tool which I purposely developed to handle and quantitatively analyse images representing individual neurons in 2D culture or brain slices [36]. Both software are open-source, so they can be freely downloaded, respectively at <http://rsb.info.nih.gov/ij/download.html> and <https://github.com/CentroEPIaggio/NEMO>.

**ImageJ analysis** After image loading, the work-flow adopted for the analysis using ImageJ is performed in three steps:

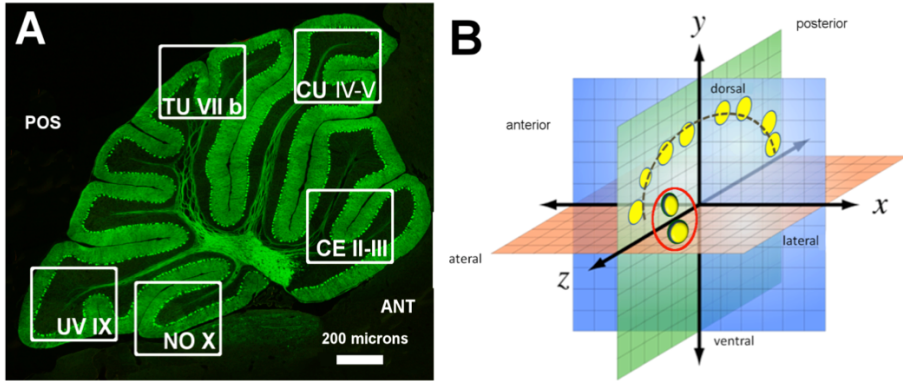


Figure 5.1: (A) Low magnification view of a para-sagittal cryosection of the vermis of a WT male mouse. The piriform layer consisting of the aligned somata of the PCs is clearly visible. Note that the GFP tag is distributed in the entire cytoplasm of the PCs so that their extensive dendritic arborizations appear as an overall diffuse fluorescence of the molecular layer and the axons can easily be seen travelling across the white matter to reach the fastigial nucleus at the basis of cerebellum. The five lobules considered in this study are indicated by their descriptive names and corresponding roman numerals. Abbreviation: CE = lobulus centralis; CU = culmen; NO = nodulus; TU = tuber vermis; UV = uvula; PNs = Purkinje neurons; ANT = anterior; POS = posterior. (B) Diagram showing the 3D planes of the mouse cerebellum. Parasagittal sections are cut along the YZ plane (green). The fluorescent somata of the PNs (yellow ovals) are aligned along a curved dashed line. Displacement of the PNs along the YZ plane (green) is exemplified by the somata that lie above or below the black dashed line of the piriform layer.

1. The image is filtered to reduce noise;
2. A threshold is applied to convert it into a binary image, eliminating the PCs dendritic arbour and just preserving somata;
3. After setting the scale to gather measurement using the real value (i.e.  $\mu\text{m}$ ) and choosing the parameters to extract (i.e. Feret's diameters and area), the "Analyse particles" command is applied.

Data extracted were stored in a Microsoft Excel spreadsheet for subsequent statistical analysis.

**NEMO analysis** NEMO was used to analyse the topological arrangement of the neurons within sections, enabling the extraction of relevant metrical features. In this study, NEMO for the topological analysis was modified as shown in the work-flow in Figure 5.2.

The algorithm works in 5 steps:

1. The image is loaded and automatically segmented using the Otsu thresholding technique [64] in order to identify the Purkinje somata, represented by white pixels, and isolating them from the background, represented by black pixels (Figure 5.2 **(A)**);
2. Three image crops representing an almost -linear segment of the piriform layer (line of the PCs) of the cerebellar cortex are chosen by the user;
3. Using the circular Hough transform [81] on the binary image, only the somata in a specific diameter range are selected. In fact, only somata with a diameter in the range previously evaluated in the Feret's diameter analysis were considered. In this way, only the on-focus PCs are considered, eliminating those from different focal planes (Figure 5.2 **(B)**);

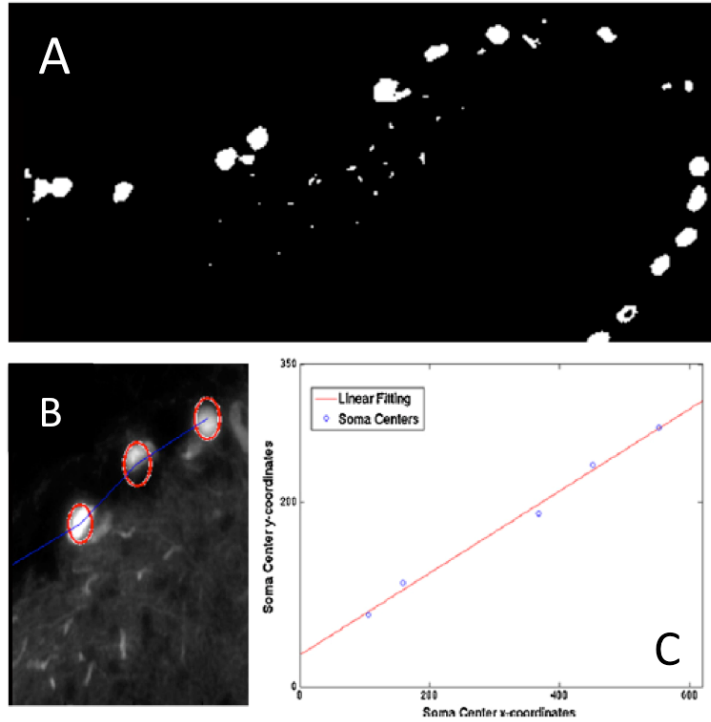


Figure 5.2: Main steps in the NEMO work-flow used to calculate the dispersion of PCs along the YZ cerebellar plane. (A) The effect of image thresholding to separate the fluorescent white pixels from the black background. Thresholding was necessary to eliminate the fluorescent dendritic arbours in the molecular layer. In the example, fluorescent Purkinje axons are still visible in the granular layer. (B) Purkinje somata detected by the Hough transform (C) Plot of X and Y coordinates of five Purkinje somata (blue circles) and the linear fitting line (red) calculated by NEMO.

4. Returning the Hough transform, the (x,y) coordinates of each soma center in the range selected, these data obtained are fitted to a straight line (Figure 5.2 (C));
5. The goodness of fit is finally evaluated through the root mean squared error (RMSE): a more chaotic layer organization reflects a higher value of the RMSE.

All the information extracted for each crop selected is finally stored in a datamatrix.

**Statistical analysis** Using GraphPad Prism v.6 (GraphPad Software, CA, USA), comparisons between the n=4 groups of animals and the r=5 cerebellum regions under study were performed with 1-way ordinary ANOVA or 2-way ANOVA followed by Tukeys Multiple comparison test, in order to highlight differences between the vermal lobules, the genotype and the sex. Difference were considered statistically significant at  $p < 0.001$ .

### 5.2.2 Results

**PCs Feret's diameter** In this analysis we have considered only objects with a Feret's diameter  $> 9$  and  $< 30 \mu\text{m}$ , because smaller diameters likely correspond to the main dendritic trunks that escape thresholding, while larger ones may represent more than one PC clustered together. Using this criteria, the frequency distribution of Feret's diameters of PCs (n. of animals: 24; n. of PCs: 9868) gave the following values of descriptive statistics: mean:  $17.92 \pm 0.05 \mu\text{m}$ , median  $17.79 \mu\text{m}$ , asymmetry: 0.29 (see Figure 5.3 (A))

**PCs area** The mean areas of the PCs were compared between the two sex and genotypes by 2-way ANOVA (see Figure 5.3 (B)). Multiple



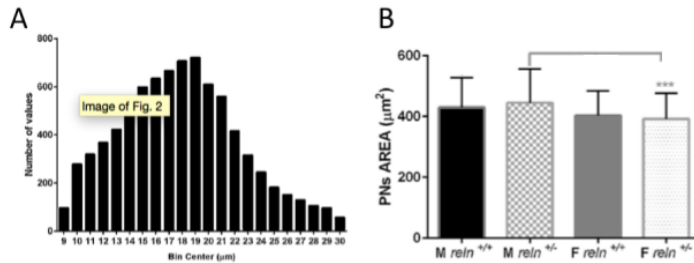


Figure 5.3: (A) Frequency distribution histogram of the size of PCs after exclusion of the 2D objects smaller than  $9 \mu\text{m}$  and larger than  $9 \mu\text{m}$ . Soma size follows a normal distribution. (B) 2-way ANOVA shows that *reln*<sup>+/-</sup> males have larger PC areas than the female genotypes.

comparison tests demonstrated that *reln*<sup>+/-</sup> males have larger PCs than *reln*<sup>+/-</sup> females (mean ( $\mu\text{m}^2$ )  $\pm$  SD: WT males:  $429.74 \mu\text{m}^2 \pm 97.60$ ; *reln*<sup>+/-</sup> males:  $444.53 \mu\text{m}^2 \pm 112.08$ ; WT females:  $402.77 \mu\text{m}^2 \pm 81.72$ ; *reln*<sup>+/-</sup> females:  $392.30 \mu\text{m}^2 \pm 84.18$ ).

Then, the mean values of PC areas were statistically analysed considering the genotype and the cerebellar lobule as variables. After 2-way ANOVA for repeated measurements, and Tukey's multiple comparison test, the source of variation between samples was related to the genotype but not the cerebellar lobules.

**Misalignment of the PCs long the dorso-ventral axis (YZ) of cerebellum** Misalignment of the PCs along the dorso-ventral axis of cerebellum was measured by fitting the (x,y) coordinates of each soma center to a straight line. The goodness of fit was evaluated by calculating RMSE.

After 2-way ANOVA and Tukey's multiple comparison test, *reln*<sup>+/-</sup> males had higher values of RMSE than *reln*<sup>+/+</sup> males and *reln*<sup>+/-</sup> females, but

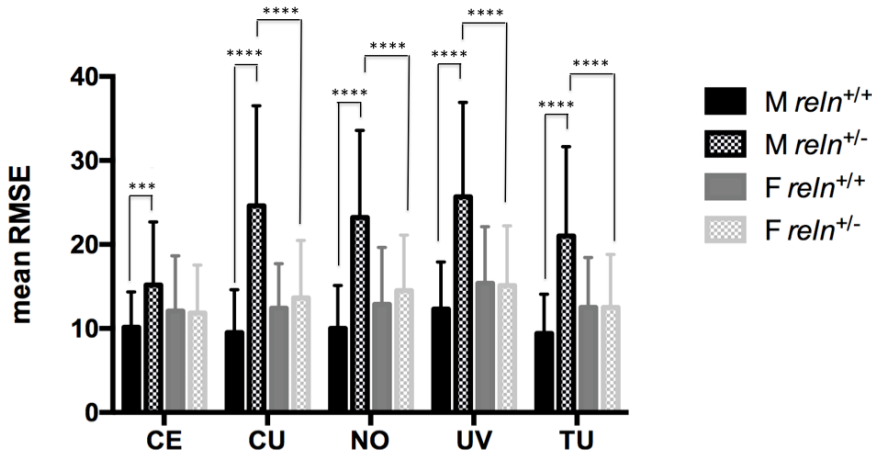


Figure 5.4: 2-way ANOVA with multiple comparison test shows statistically significant differences in the mean RMSE (that measures PC misalignment along the YZ cerebellar axis) between *reln*<sup>+/-</sup> males and *reln*<sup>+/-</sup> females in four of the five cerebellar lobules examined in this study (with the exception of the lobulus centralis) and between *reln*<sup>+/-</sup> and WT males in all lobules considered (\*\*\*) =  $P = 0.001$ ; \*\*\*\* =  $P < 0.001$ ). Error bars in graphs indicate SD. Abbreviation: CE = lobulus centralis; CU = culmen; NO = nodulus; TU = tuber vermis; UV = uvula; PNs = Purkinje neurons; F = female; M = male; RMSE = root mean squared error of linear fit.

not *reln*<sup>+/+</sup> females in all lobules (Figure 5.4). As RMSE is related to the arrangement of the PCs within the dorso-ventral axis of cerebellum (Figure 5.1 (B)), these results show that neurons in heterozygous mutant males are more chaotically arranged than in homozygous normal mice and, with the exception of the central lobulus, heterozygous mutant females. They also indicate a tendency of females to have a more ordered distribution of PCs than males, irrespective of the genotype.

### 5.2.3 Discussion

The role of reelin in controlling neuronal migration and maturation in the mammalian brain is widely established [200]. However, not only is reelin fundamental for normal cerebellar development, but several lines of evidence implicate the protein as an important player in the etiopathology of autism [201]. For this reason, the study of the *reln*-haplodeficient heterozygous mice attracted the attention of the neuroscientists as possible models of neuropsychiatric conditions in translational study [201]. Unfortunately, data about the structural alteration in *reln*+/- mouse cerebellum are fragmentary; moreover, there are limited studies on the existence of sex-related differences in the number and size of PCs in the mutant reelin mice [202, 203].

In this light, the investigation was aimed at morphological and topological characterization of Purkinje neuron micro-structure, in relation to gender and genotype, taking also into account different cerebellar regions.

As regard the size of PCs, the analysis shows that heterozygous mutant males have larger neurons than females.

This preliminary study also demonstrates that topological alterations can be detected in the cerebellar vermis of the *reln* +/- mutants using image processing techniques. Using Cre-Lox recombination, observations in mice genetically engineered to tag the Disabled-1 (*Dab1*) expressing neurons (that potentially respond to Reelin) indicated that positioning errors in the adult mutant-labelled neurons varied from subtle to extensive, and regarded both the latero-lateral and dorso-ventral axes of the developing brain with differences among different neuronal populations [204]. In the present study, *reln* +/- male mice have a more chaotic arrangement of their PCs along the dorso-ventral axis of cerebellum, and the dispersion of the PCs along the YZ axis occurs in all cerebellar lobules. In addition, heterozygous mutant males also display higher RMSE values than mutant

females, with the exception of central lobulus. No statistically relevant differences were found between females  $reln+/-$  and  $reln+/+$ . It is not surprising that in  $reln +/-$  mice misalignment of PCs occurs along the YZ axis of cerebellar laminae, as this axis coincides with the trajectory along which PCs migrate from the cerebellar ventricular zone to constitute the piriform layer, and *reelin* plays a fundamental role in the migration and final alignment of these neurons during cerebellar development [205, 206]. These observations suggest that the *reln* mutation has less severe phenotypic effects on PCs of females.

Although the findings in this preliminary study are a good starting point to clarify the misleading results in neuroscience literature about autism and sexual dimorphism in neuro-developmental disorders, they cannot be exhaustive, since it is not possible to extract information about PCs dendrites and their arborization. A more sophisticated analysis than the one carried out here would be required to fully clarify whether or not the mutant mice are of interest in translational studies. For this reason, the work-flow designed in this PhD thesis was applied to study the sexual dimorphism in a more promising model of autism, the *Engrailed2* ( $En2/-$ ) knock-out mouse.

## 5.3 From NeMo to N3MO: application of the designed work-flow to the *Engrailed* murine model of autism

### 5.3.1 Materials and Methods

**Tissue preparation and confocal imaging** L7GFP WT (wild-type) mice and the homozygote L7GFP/*En2*<sup>-/-</sup> knock-out as animal model of

ASD were considered for the study of PCs in the cerebellum. For each genotype both male and female individuals were studied, for a total of 8 mice sacrificed. Mice were perfused and brains were carefully extracted and treated as detailed in Chapter 2; in particular,  $n=36$  1 mm-thick slices were cut and optimally clarified, following the protocol described in Chapter 2, for 5 days.

For each clarified cerebellum slice, at least 2 confocal stacks were acquired with a Nikon A1 confocal microscope. The acquisition settings are summarised in Table 3.1. During acquisition, no limits were imposed to the depth of the dataset, thus the height of different Z-Stacks is variable for each acquisition and dependent on biological variability (i.e. the different spatial distribution of PCs in different mouse cerebella).

### **Neuron tracing with the SmRG algorithm and N3MO analysis**

The confocal stacks were processed with the SmRG algorithm described in Chapter 3, obtaining about 30 single-traced PCs for each genotype and sex.

The neurons were then analysed using N3MO (see Chapter 4 for more details), in order to obtain the morphological features of interest.

**Statistical analysis** On each morphological variable extracted, statistical analyses were carried out using 2-way ANOVA for repeated-measures analysis followed by Sidaks Multiple Comparison Test, after verifying that the data are normally distributed (i.e. through Kolmogorov-Smirnov Gaussianity test) and setting significance at  $p<0.001$ .

## **5.3.2 Results**

**Sholl Analysis** As already detailed in Chapter 4, the Sholl analysis is a morphometric method to evaluate the neurite architecture of neurons

by drawing a series of concentric spheres around the neuron soma. In particular, two different coordinate systems can be used to evaluate the number of intersections versus the sphere radius: one with a constant number of spheres and the other with a constant inter-sphere distance (established as 10  $\mu\text{m}$ ). In this context, since the results obtained with the two systems were similar, only the one regarding the constant number of spheres coordinate system were showed for its graphical simplicity.

The analysis of the number of intersections vs. sphere radius shows that the best fitting is Gaussian only for L7GFP/ WT mice, as shown in Figure 5.5 (A) and (B), with a peak corresponding to intermediate values of the radius. The goodness of fitting was evaluated through the square of the multiple correlation coefficient (RS), resulting in 0.8942 for L7GFP/WT males and 0.8793 for females. On the other hand, in PCs from L7GFP/En2  $-/-$  mice the peak of intersections is more shifted towards lower values of the radius. Moreover, data show an exponential trend, reported in Figure 5.5 (C) and (D) (RS for L7GFP/En2  $-/-$  males = 0.9729; females = 0.8188).

The plot of Log-Log and Semi-Log methods revealed that both in WT and En2  $-/-$  the Log-Log method is more appropriate as it better approximates the results. In fact, the value of the Determination Ratio is less than 1 for all the neurons analysed.

As regards the Schoenen coefficient, 2-way ANOVA followed by multiple comparison test shows that it decreases significantly in both sexed En2  $-/-$  mice [mean  $\pm$  SD: WT males:  $12.13 \pm 3.39$ ; En2  $-/-$  males:  $7.13 \pm 2.52$ ; WT females:  $13.86 \pm 2.95$ ; En2  $-/-$  females:  $5.60 \pm 1.94$ ], as shown in Figure 5.6: PCs from En2  $-/-$  mice are less branched than the WT ones.

The Sholl regression coefficient analysis (Figure 5.7) shows that the number of intersections versus the distance from the soma center de-

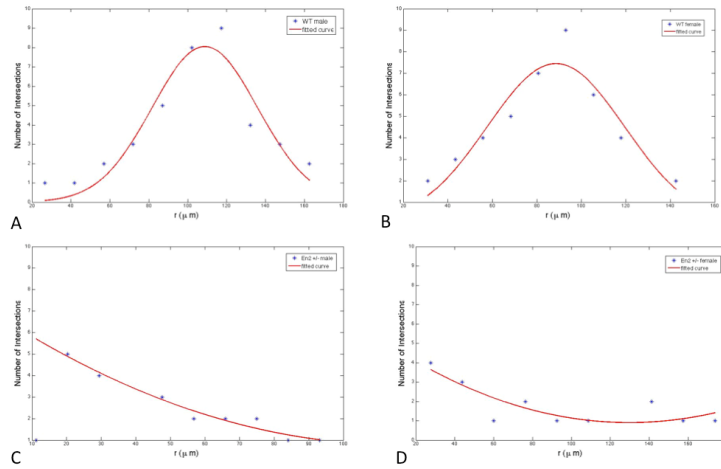


Figure 5.5: Interpolation of the number of intersections as a function of radius for an typical PC from (A) a L7GFP/WT male mice, (B) a L7GFP/WT female mice, (C) a L7GFP/En2 +/- male mice and (D) a L7GFP/En2 -/- female mice.

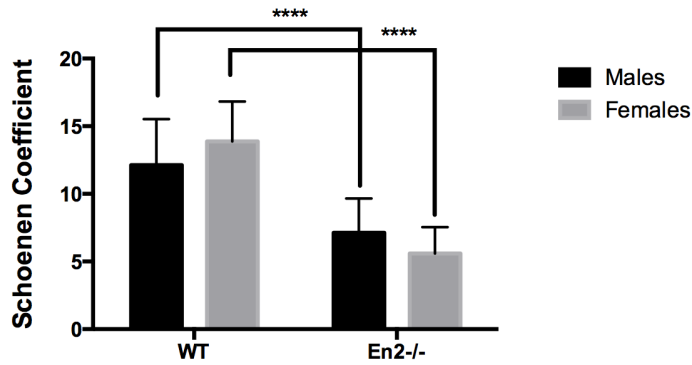


Figure 5.6: 2-way ANOVA for repeated measures with multiple comparison test shows statistically significant differences in the mean values of the Schoenen Coefficient between WT and En2<sup>-/-</sup> mice for both males and females. Error bars in graphs indicate SD. ( $p < 0.001$ )

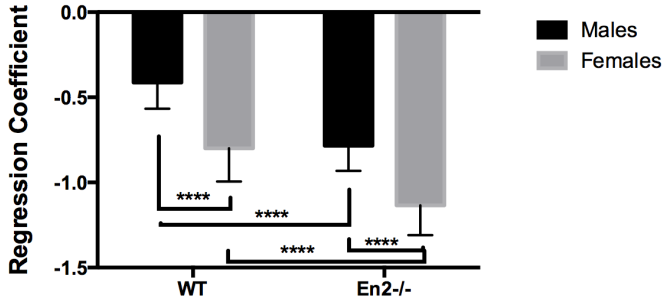


Figure 5.7: 2-way ANOVA for repeated measures with multiple comparison test shows statistically significant differences in the mean values of the Sholl regression coefficient between the four groups analysed. Error bars in graphs indicate SD. ( $p < 0.001$ ).

cays significantly faster in PC from L7GFP/En2 <sup>-/-</sup> mice than from L7GFP/WT ones, for both males and females. Moreover, the coefficient is significantly higher for the females than for the males, for both the genotypes considered [mean ( $\mu\text{m}^3$ )  $\pm$  SD: WT males:  $-0.41 \pm 0.15$ ; En2<sup>-/-</sup> males:  $-0.78 \pm 0.14$ ; WT females:  $-0.79 \pm 0.13$ ; En2<sup>-/-</sup> females:  $1.13 \pm 0.17$ ].

Finally, the observation of the minimum pathway (measured, as described in Chapter 4, as the sum of the magnitudes of the euclidean distance between the cell intersections on two adjacent spheres) reveals no statistically relevant differences in the four mouse groups analysed.

### Other morphometric variables extracted using N3MO

**Soma Volume** The mean values of the Soma Volume were subjected to statistical analysis considering both the genotype and the gen-



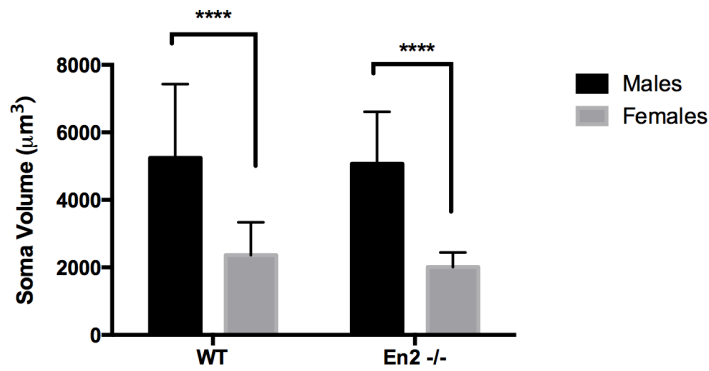


Figure 5.8: 2-way ANOVA for repeated measures with multiple comparison test shows statistically significant differences in the mean values of the Soma Volume between males and females for both WT and *En2* <sup>-/-</sup> mice. Error bars in graphs indicate SD. ( $p < 0.001$ )

der as variables. 2-way ANOVA for repeated measures followed by the Sidak's multiple comparison tests of raw data demonstrated a statistically significant reduction in soma size in female mice with respect to male ones, regardless of genotype, as shown in Figure 5.8 [mean ( $\mu\text{m}^3$ )  $\pm$  SD: WT males:  $5241.35 \pm 2187.54$ ; *En2* <sup>-/-</sup> males:  $5071.04 \pm 1536.43$ ; WT females:  $2365 \pm 969.96$ ; *En2* <sup>-/-</sup> females:  $2011.09 \pm 433.26$ ].

**Neuron Surface-to-Volume ratio** The Surface-Area-to-Volume ratio was evaluated in order to have simple but significant morphological information on PCs, since it can be used as a raw index of neuron complexity, as discussed in Chapter 4.

Multiple comparison tests demonstrated that *En2* <sup>-/-</sup> mice are less complex than WT ones, for both males and females. No significant differences were found between males and females [mean  $\pm$  SD: WT males:  $0.66 \pm$

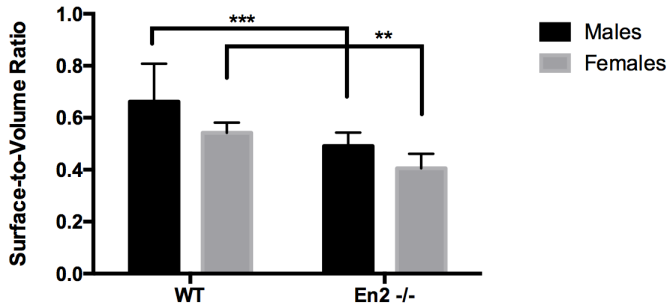


Figure 5.9: 2-way ANOVA for repeated measures with multiple comparison test shows statistically significant differences in the mean values of the Surface-Area-to-Volume ratio between WT and En2<sup>-/-</sup> mice for both males and females. Error bars in graphs indicate SD. ( $p < 0.001$ )

0.14; En2<sup>-/-</sup> males:  $0.49 \pm 0.05$ ; WT females:  $0.54 \pm 0.03$ ; En2<sup>-/-</sup> females:  $0.40 \pm 0.05$ ], as shown in Figure 5.9.

**Branching analysis** As already detailed in Chapter 4, using N3MO, two different parameters can be extracted to evaluate neuron branching, which could be considered a benchmark of neuron arborization: i) Number of Branches and ii) Schoenen Coefficient. A 2-way ANOVA followed by multiple comparison test shows that the number of branches decreases significantly in En2<sup>-/-</sup> mice, in both the gender (Figure 5.10) (A). On the other hand, no statistically relevant differences were obtained between males and females in both the genotypes considered [mean  $\pm$  SD: WT males:  $68.47 \pm 16.39$ ; En2<sup>-/-</sup> males:  $19.14 \pm 8.72$ ; WT females:  $57.40 \pm 22.32$ ; En2<sup>-/-</sup> females:  $21.53 \pm 4.60$ ]. Results agree with those obtained for the Schoenen Coefficient, detailed in the previous paragraph, confirming the results of Garcia et al. (2014) [207].

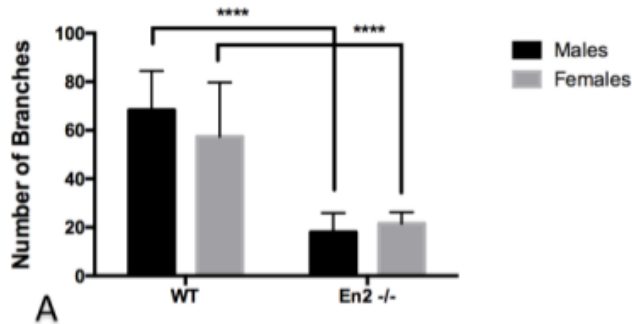


Figure 5.10: 2-way ANOVA for repeated measures with multiple comparison test shows statistically significant differences in the mean values of the Number of Branches between WT and En2 -/- mice for both males and females. Error bars in graphs indicate SD. ( $p < 0.001$ )

**Fractal Dimension** For the fractal analysis, the 3D box-counting method was applied (see Chapter 4 for details). The local slope of the curve versus the box size confirm the presence of fractal properties in a particular range of box size, and the fractal dimension was evaluated in this range. The range of the box size in which the slope of curve is constant is smaller for L7GFP/En2 -/- mice.

As shown in Figure 5.11, the fractal dimension of PCs is significantly smaller for L7GFP/En2 -/- mice, for both sexes; no relevant differences was found between males and females, regardless the genotype [mean  $\pm$  SD: WT males:  $1.40 \pm 0.31$ ; En2-/- males:  $0.95 \pm 0.23$ ; WT females:  $1.42 \pm 0.21$ ; En2-/- females:  $1.14 \pm 0.09$ ].

**Radial Extension** Figure 5.12 shows the mean values of the Radial Extension of PCs from all the groups analysed.

2-way ANOVA with repeated measures followed by Sidak's multiple com-

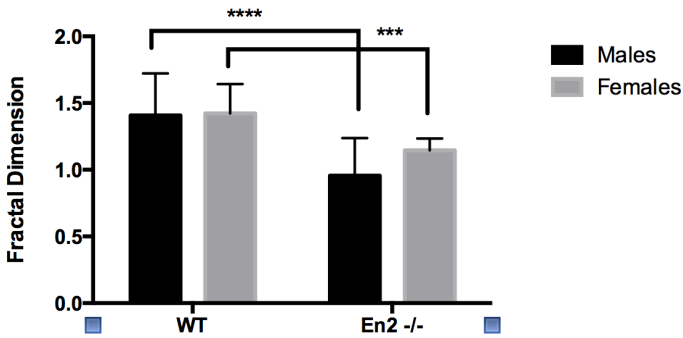


Figure 5.11: 2-way ANOVA for repeated measures with multiple comparison test shows statistically significant differences in the mean values of the Fractal Dimension, measured using the box-counting method, between WT and En2<sup>-/-</sup> mice for both males and females. Error bars in graphs indicate SD. ( $p < 0.001$ )

parison test revealed that the radial extension in PCs from female mice is significantly higher than in males, for both genotypes considered. Moreover, there is a statistical relevant decrease in radial extension in PCs from En2<sup>-/-</sup> male mice with respect to the control ones [mean ( $\mu\text{m}$ )  $\pm$  SD: WT males:  $170.14 \pm 24.38$ ; En2<sup>-/-</sup> males:  $122.22 \pm 32.13$ ; WT females:  $233.03 \pm 40.05$ ; En2<sup>-/-</sup> females:  $236.84 \pm 56.76$ ].

As regards the cone angle, no significant statistical differences were observed between all the groups analysed: in fact, the cone angle is always narrow and about  $50^\circ$ , indicating a preferential direction of extension (as expected for PCs, which are highly oriented in the sagittal plane [208]).

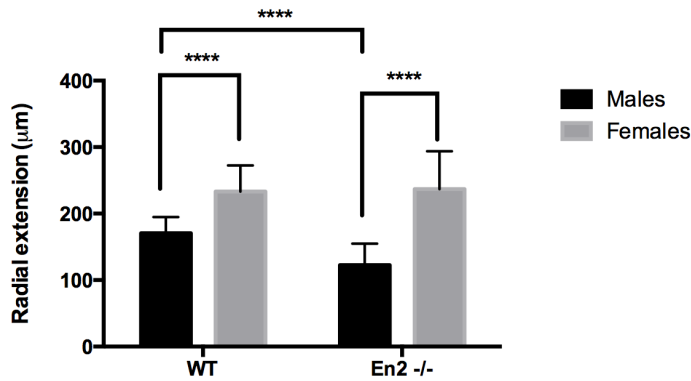


Figure 5.12: 2-way ANOVA for repeated measures with multiple comparison test shows statistically significant differences in the mean values of the Radial Extension between WT and En2 -/- mice for both males and females. Error bars in graphs indicate SD. ( $p < 0.001$ )

### 5.3.3 Discussion

The Engrailed2 knock-out murine model is considered one of the most promising model of autism by the neuroscience community [168], since it shows most of the the anatomical, functional and behavioural characteristics of ASDs in humans. To date, there are no studies in the literature which report a quantitative evaluation of the microstructure abnormalities of the En2 gene.

In this light, the work-flow designed for this PhD thesis was applied to the study of the morphological alterations of Purkinje cells from two different genotypes in their arrangement in the cerebellum. In particular, L7GFP/En2 -/- transgenic mice, homozygote for En2 gene, that displays a phenotype reminiscent of the cerebellar anatomical abnormalities reported in autism, were compared with L7GFP/WT mice. In addition,

since there is an unbalanced of Autism Spectrum Disorders diagnosed between males and females, both sexed mice were considered. In particular, 1 mm -thick cerebellum slices for the four groups analysed were optimally clarified and stacks were acquired with a Nikon confocal microscope. Datasets were then processed and analysed using N3MO, purposely developed to trace single neurons and extract morphological differences between the four groups.

The results show that most of the morphological features extracted with N3MO, summarized in Table 5.1, can be attributed only to gender or to the *En2* gene. For this reason, the variables were classified in gender-related and genotype-related (see Table 5.1): while the former variables are more linked to differences in neuron size (i.e. soma volume and radial extension), the latter ones refer more to the neuron arborization complexity (i.e. number of branches, Schoenen coefficient, fractality and Surface-to-Volume ratio).

As regards gender, PCs from female mice show smaller somata and higher radial extension than male ones. The results are consistent with the findings in Tobet's review, which reported changes in neuron dimensions between males and females in different brain regions [209]. As regards the genotype-related variables, all of them show a decrease of neuron arborization complexity (i.e. reduced neurite branching and fractality) in *En2* +/- mice respect to the WT ones, independent of mouse gender.

Table 5.1: Comparison of features extracted from PCs for the four groups analysed, classified in gender- and genotype related.

Morphological Variables	Gender-Based	Genotype-based
<i>Plot of Log-Log or Semi-Log method</i>		Log-Log method is better for all the group analysed
<i>Number of intersections vs. sphere radius</i>	-	Gaussian distribution for En2+/- mice; Exponential distribution for WT mice.
<i>Maximum number of intersections</i>	-	- Lower for PCs from En2 +/- mice then from WT ones - Maximum at intermediate r for WT mice - Maximum at small r for the En2 +/- ones

Morphological Variables	Gender-Based	Genotype-based
<i>Schoenen Coefficient</i>	-	PCs from En2 +/- mice are less arborized than WT ones
Minimum Pathway	-	-
<i>Regression Coefficient</i>	Number of intersections decreases faster in females	Number of intersections decreases faster in En2 +/-.
<i>Fractality</i>	-	PCs from En2 +/- mice are less fractal than WT ones
<i>Number of Branches</i>	-	PCs from En2 +/- mice are less arborized than WT ones
<i>Radial Extension</i>	PCs from female mice are more elongated than male ones	Only En2 +/- male mice are less elongated than WT males
<i>Cone Angle</i>	-	-



<b>Morphological Variables</b>	<b>Gender-Based</b>	<b>Genotype-based</b>
<i>Surface-to-Volume ratio</i>	-	PCs from En2 +/- mice are less complex than WT ones
Soma Volume	PCs somata from female mice are smaller than those from males.	-

## 5.4 Conclusion

It is well known that at the micro-structural level, neuronal morphology within the brain is important for higher level brain function [6, 96]. Therefore, morphological features (i.e. neuron shape, size and dendritic branching) can elucidate the functional role of different neurons. Moreover, morphometric analyses can be crucial for the study of alterations in the dendritic/axonal field of neurons or neuronal morphology correlates to diseases [108]. On the other hand, according to Dr Judith Gould, Consultant Clinical Psychologist and Director of The Lorna Wing Centre for Autism, *“Autism is more diverse than originally thought, with new ideas being put forward every day. In fact, it’s a case of “the more we know, the less we know”, particularly in how gender affects individuals with autism”*.

The speech highlights the unbalanced incidence of the disorder between males and females as a crucial step to better understand the ASDs.

In this context, the aim of this Chapter was to quantitatively evaluate PC morphology, both in 2D images and 3D stacks, in order to extract discriminating features of both gender and autism. Since both the two murine models of autism and the extraction processing and techniques differ, we cannot directly compare the results obtained in the two studies presented. However, the methods used are efficient for the classification and analysis of neurons. It is clear that in order to obtain faithful information about neuron morphology within the context of their native arrangement within the brain, the three-dimensional evaluation is more physiologically relevant than the two-dimensional study. On the other hand, a comparative study of neurons using standard 2D imaging can represent a starting point for establishing proofs and concepts.

As regards the En2 murine model of autism, although the number of samples analysed was limited, PCs from this model of autism are likely

to be less arborized than the control mice. This result is confirmed by different morphological parameters extracted with N3MO (i.e. fractal dimension, Schoenen index, number of branches). Moreover, in a specific genotype, males and females present the same arborization complexity. This independence from gender is confirmed also by a behavioural study conducted on *Engrailed2* mice, where no sex differences in any of the behavioral abnormalities were detected [210]. These preliminary findings seem to support the "wrong diagnosis criteria" theory. Just as for men and boys, diagnosis is the starting point for providing appropriate support for women and girls on the autism spectrum. A timely diagnosis can avoid many of the difficulties they experience throughout their lives. Further studies on the 3D morphology of PCs in animal models of autism could help to better understand neuronal architecture, to improve the knowledge on the genetic and structural basis of autism and its male bias, to define new diagnostic strategies and could also lead to the development of new therapeutic approaches.

As regard the gender-related differences, PCs from female mice seem to be characterized by smaller somata and higher radial extension than males ones. These findings have implications for developmental studies that could directly test hypotheses about mechanisms relating sex steroid hormones to sexual dimorphisms.

1

---

<sup>1</sup>Some of the results presented in this chapter have been published in : Magliaro et al., "The number of Purkinje neurons and their topology in the cerebellar vermis of normal and *reln* haplodeficient mouse" , *Annals of Anatomy- Anatomischer Anzeiger* (2016), doi:10.1016/j.aanat.2016.02.009, *in press*.



# Chapter 6

## A starting point for the study of claustral organization

*"We think that a more appropriate analogy for the claustrum is that of a conductor coordinating a group of players in the orchestra, the various cortical regions. Without the conductor, the players can still play but they fall increasingly out of synchrony with each other. The result is a cacophony of sounds."*

*(F. C. Crick, C. Koch)*

### Abstract

The structure and function of the claustrum are still a matter of intense debate and investigation, since a characterization of the distribution of neurons in their three-dimensional context within this nucleus is still lacking. In fact, few studies about claustral neurons have been performed. To this end, in this Chapter a preliminary study was performed on 2D histological micrographs of dog claustrum, to classify different neuron types with respect to their soma shape. Since the results obtained demonstrate that soma shape can be used to distinguish between different neuron

types, but the classification cannot be fully exhaustive because neuron arborization cannot be taken into account, some elements of the workflow designed during this PhD thesis were applied to human claustrum samples. In particular, 500  $\mu\text{m}$ -thick slices were clarified using the procedures and the optimal parameters identified in Chapter 2 for un-perfused and un-labelled tissues. Then, slices were immuno-labelled and three-dimensional datasets were acquired using a confocal microscope. These volumetric datasets may represent a starting point to pursue the knowledge of structure-function relationship in this enigmatic nucleus.

## 6.1 What is the function of the claustrum?

The claustrum is a sub-cortical structure located in the baso-lateral telencephalon, one on each side of the head, of all the mammalian brains [211]. It has been a subject of inquiry since its first identification, by A. Kappers (1936), as a thin strip of grey matter enclosed between stretches of neighbouring fiber bundles. Though much has been learned since this time through the application of modern neuroscience techniques, several problems still persist. In fact, due to its modest size, intricate shape and deep internal location, it is difficult to study using many modern techniques that need a certain roominess of tissue to their application [212]. For these limits, despite the fact that its structure, physiology, connections and neuro-chemistry have been studied in multiple species, its function in humans is still matter of debate [211].

The function of the claustrum has proven to be hard to unlock for different reasons. In particular, the shape of the nucleus has made complete and discrete claustrum lesions impossible to achieve using conventional chemical or mechanical means. Clinical pathological correlation studies have yielded extraordinary information about the function of many brain sites, but no convincing selective claustral lesions have been reported in

humans following cerebral haemorrhage or ischemia. Without the ability to generate reproducible, discrete lesions of the claustrum in animals, the functional roles of this nucleus remain a mystery. In this light, despite waves of interest in the claustrum over the century, two main controversial hypotheses on its functional attributes exist [213]:

1. **Multi-sensory integration:** based on bidirectional cortical connectivity, the claustrum has been proposed to function as a multi-sensory integrator, serving to bind information from disparate sensory cortices. Two different theories for multi-sensory integration have been proposed. The first theory states that multi-sensory integration occurs in polymodal sites that only process specific sensory combinations. Because the claustrum appears to have multisensory-responsive cells, the claustrum may serve to bind some types of sensory modalities [214]. The second theory, proposed by Ettliger and Wilson (1990) [215], states that no one structure in brain executes the processes required for cross-modal performance. Instead, only a sub-cortical relay nucleus is required through which different sensory cortices can access each other in order to associate modalities. This sub-cortical relay nucleus was proposed to be the claustrum. In this way, the claustrum theoretically synchronizes cortical areas to accomplish the feat of crossing modalities. They did not state, however, how this may be accomplished or where the binding of multi-modal information would occur.

Despite *in vivo* functional imaging studies exploring multi-sensory integration largely support the second theory, the imaging studies that do support a role of the claustrum in multi-sensory integration do not address the question of where polymodal information is being bound exactly, and suffer from the inability to discriminate claustral vs. insular activation.

2. **Crick and Koch's hypothesis:** Crick and Koch [46] hypothesized that the claustrum is where sensory information is bound, functioning as a generator of the unified perception of a multitude of sensory stimuli in one's environment (i.e. conscious percepts). That is, putting individual stimuli together, one is able to recognize an object as a whole rather than experiencing each stimulus as a separate sensory entity. Crick and Koch argued that since almost all theories attempting to explain the neural correlate of such an experience (consciousness) require a need to rapidly integrate and bind information in neurons that are situated across distinct cortical and thalamic regions, that the claustrum may be perfectly suited to subserve such a function due to its unique feature of reciprocal connectivity with the cortex, its central positioning in the brain and its connections with the thalamus. Crick and Koch proposed that the binding of multi-sensory information in the claustrum underlies the unification of sensory experiences. This hypothesis has supported by Smythies et al. (2015) studies [216], who proposed that the claustrum functions as a detector, modulator and integrator of synchronous oscillations for the purpose of subserving cognitive processes such as consciousness.

Though the claustrum does appear to have many of the attributes required of a sensory binding site, some problems exist with this concept. Firstly, a well-recognized physiological trait of claustral cells consistently found across functional studies is their quiescent nature. The spontaneous firing rate is quite low: if the claustrum is binding sensory stimuli for the purpose of generating conscious percepts, one would predict that the claustrum would display near constant activation during awake, behaving conditions. In addition, the Crick and Koch model places the high computational load re-



quirement of binding in a structure that is not layered, or at least not organized.

Other “minor” hypotheses presented in the literature propose a role for the claustrum in saliency detection [47], active sensing [217] and segregation of attention [218, 213]. Interestingly, all these hypotheses revolve around a common theme, that of enabling the formation of an accurate and cohesive representation of the world around us.

### 6.1.1 Neuron cell types in mammalian claustrum

A striking feature of the claustrum is the few neuronal types it has compared with those of the cerebral cortex. Moreover, while the latter is clearly laminated, the former is not [46]. There is general agreement that the most common cell type, called type I, is a large cell whose dendrites are covered by spines [48, 219]. The axons of these type I cells, after throwing off local collaterals, often leave the claustrum either medially or laterally. They are the principal cells of the claustrum in that they can both receive an input from the cortex and project back. Their shape varies considerably, the soma of some being pyramidal, some fusiform and others with more spherical somata. All authors agree that they cannot find discontinuous sub-groups of type I neurons and have therefore lumped them together under one heading. The dendrites of these cells do not have a preferred orientation (unlike, for example, the apical dendrites of cortical pyramidal cells).

**Claustral interneurons** Other claustral neurons lack spines and so have largely smooth dendrites. There appear to be two types of aspiny neurons, one with large and the other with small cell bodies. The latter are fairly compact cells, whereas the dendrites and axons of the large type are more extensive. The axon of these cells does not leave the claustrum,

so they are both classed as interneurons.

The claustral interneurons, as in the cortex [220], seem to play a crucial role in the inhibitory circuits providing a substrate for local information processing [46]. Calcium-binding proteins (i.e. calretinin, calbindin and parvalbumin) are considered markers of three non-overlapping interneuronal populations [220]. Moreover, a recent study indicates that cortical interneurons can also be classified by their expression of parvalbumin, somatostatin, and vasointestinal peptide [221].

In particular, parvalbumin is a marker of a specific class of interneurons, the category of fast-spiking neurons, involved in the generation of gamma oscillations which have an important role in the transmission of information between cortical and hippocampal areas [222, 223, 224, 225, 226, 227, 228, 229, 230, 231]. The presence of parvalbumin-immunoreactive interneurons, with gap junctions along their dendrites, was described in the cerebral cortex supra-granular layer [232]. Moreover, many immunohistochemical studies have shown the presence of parvalbumin in the claustrum of different animals [233, 234, 235, 236, 237], and a recent detailed study also describes the distribution of parvalbumin in the human claustrum [238].

In order to characterize claustrum micro-structure, this Chapter aims to analyse the morphology of parvalbumin -immunoreactive neurons. This type of neurons lends themselves to the analysis for two main reasons: firstly, interneurons have an important role in integration of the information, that seems to be one of candidate function of the claustrum. On the other hand, their neurite do not leave the claustrum, so it is possible to image them entirely.

In this Chapter, I firstly evaluate parvalbumin-immunoreactive neurons in dog claustrum thin slices, using standard histological and image process-

ing techniques. Since 2D images does not allow the fully reconstruction of neuron arborization, some elements of the work-flow designed in this PhD thesis were then applied to human claustrum thick slices.

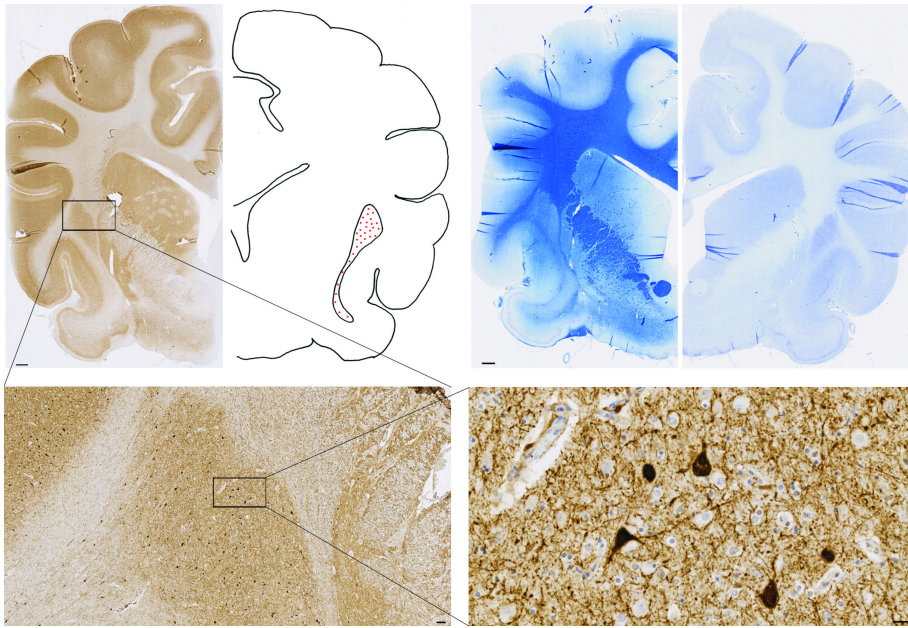
## 6.2 Parvalbumin-immunoreactive neuron classification in dog claustrum histological sections: a proof of concept

### 6.2.1 Materials and Methods

**Animal harvesting and tissue processing.** Claustrum samples were obtained from necropsy of four dogs referred to the Department of Veterinary Science of the University of Pisa for post-mortem examination. Central Nervous System abnormalities were excluded by histopathological examination.

The brains were cut in coronal slabs (0.5 mm thick), fixed by immersion in buffered formalin and processed for paraffin embedding. Each slab, containing both cerebral emispheres wew cut in half following the sagittal medial plane and embedded in serial paraffin blocks. To recognize claustra, transverse sections cut with a microtome (5  $\mu\text{m}$ ) from the left hemisphere were stained with Luxol Fast Blue (for myelin) while sections from the right hemisphere were used for Nissl staining (Figure 6.1(B)). Immunohistochemistry was then performed on serial sections using a mouse monoclonal anti-parvalbumin antibody (1:5000, cod. no. 235, lot. no.10-11 F, Swant, Bellinzona, Switzerland). inobenzidine (DAB) (sk-4105, Vector, Burlingame, CA) solution (Figure 6.1(A)-(C)-(D)).

**Image acquisition and processing and statistical analysis.** As neurons have a three-dimensional structure, it is not possible to track all the neurites constituting a neuron on a single histological slice. For this



*Figure 6.1: Microphotographs of immunohistochemical and histological staining of coronal brain sections. (A) Low magnification image (left side) of the anti-parvalbumin antibody distribution in the left hemisphere including the claustrum; schematic draw (right side) with charting representing the distribution of the PV labeled somata (red dots) in the claustrum. Scalebar: 1 mm. (B) Low magnification image of a Luxol Fast Blue (left side) and Nissl (right side) stained sections. Scalebar: 1 mm (C) Detail of A and (D) detail of C showing anti-parvalbumin labelled neurons in the ventral claustrum. Scale bars: C = 10 mm and D = 20 mm.*

reason, rather than tracing and quantifying neurites, we quantified shape parameters of 200 parvalbumin stained somata for each of the 4 dogs, in order to classify neurons according to soma shape and size.

In this optics, images were acquired with the light microscope using a 25x objective and processed with the Nikon NIS-Elements BR-4.13.00 software, which allows the measurement of different morphological features. In particular, the parameters extracted are soma area and perimeter as benchmarks of size, and circularity as shape descriptor.

In order to classify neuron somata, the dataset obtained was analysed using the k-means clustering algorithm [239]. This technique enables data clusters minimizing the sum of distances from each object to its cluster centroid.

To assess the goodness of the clustering, we verified that the sets of data obtained were significantly different through a t-test analysis, setting significance at  $p < 0.05$  and high significance at  $p > 0.01$ .

### 6.2.2 Results

Image analysis enables the identification of the main morphological features of neuron somata. A k-means clustering was performed on the morphometric dataset so as to group neurons on the basis of the measured variables. To identify the right number of clusters and establish how well-separated the groups are, we measure how close each point in one cluster is to points in the other clusters through the so-called silhouette value. In our case, two clusters were identified. In fact, the silhouette plot in Figure 6.2, which represents each neuron as a pixel-thick horizontal line with a length corresponding to its silhouette value, shows that most points in both clusters have a large silhouette value, greater than 0.8, indicating that those points are well-separated from neighbouring clusters.

The t-test analysis confirms that the two groups are characterized by

a highly significantly different soma radius ( $p = 1.58 * 10^{-5}$ ) and a similar circularity ( $p = 0.987$ ). In fact only few very small neuron somata are badly matched to the others belonging to the same cluster (*silhouettevalue* < 0). On the basis of the soma features extracted, the k-means analysis allows the classification of neurons by soma radius: in one group the soma are big ( $11.42 \pm 1.99 \mu m$ ), while in the other they are small ( $6.33 \pm 1.08 \mu m$ ). No difference was observed in soma shape, indeed the circularity value for cluster 1 was  $0.70 \pm 0.14$  while for cluster 2 was  $0.75 \pm 0.12$ .

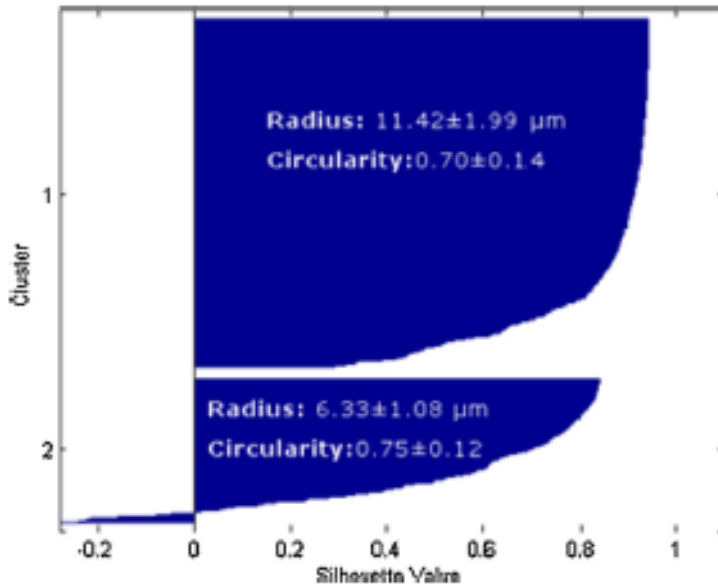


Figure 6.2: Silhouette plot showing how soma size and shape form 2 unique and tightly grouped clusters with very few outliers. Within each cluster, the high silhouette values suggest that the objects are well-matched

### 6.2.3 Discussion

In this study, a classification of neurons in dog claustrum samples according to their soma size and shape was performed. In particular, the variability of parvalbumin-immunoreactive somata shape is consistent with that already reported in other species such as: mouse [233], rat [240], rabbit [234], cat [235, 241], monkey [242], chimpanzee [237] and human [237, 238]. In particular, the shapes of parvalbumin-immunoreactive somata in the dog are analogous to the findings reported in the cat claustrum [235] which, among the above mentioned species, is phylogenetically closer to the dog.

To classify somata on the basis of their shape and size, statistical methods were used to cluster the data acquired from image analysis. This method is more objective than the commonly used method of arbitrarily defining a series of radius limits to define cell size. The main morphological features of the immuno-stained somata regarding both size and shape are summarized in Figure 6.2. k-Means clustering analysis identified two well-separated groups. A recent study in the human claustrum classified parvalbumin-immunoreactive neurons in spiny and aspiny each further arbitrarily divided according to the soma radius in large, medium and small [238]. Similar findings on soma radius have been described in the cat claustrum [235, 238]. In particular, the clusters we found according to the radius were in line with the categories of small (13 to 15  $\mu\text{m}$  in diameter) and medium (15 to 20  $\mu\text{m}$  up to 25  $\mu\text{m}$  in diameter) somata observed by [241]. LeVay and Sherk (1981) using Golgi preparations described in the cat visual claustrum large spiny (15 to 29  $\mu\text{m}$  in diameter) and small aspiny (10 to 15  $\mu\text{m}$  in diameter) neurons.

Although it is difficult to compare an immunohistochemical study to a Golgi study, it is possible to note some similar aspects. The radius values of the two clusters we found was in agreement with those reported in the

cat visual claustrum [219]. Moreover, these authors described the large spiny as the most frequent type.

Although this study on parvalbumin-immunoreactive neurons may help in the understanding the physiology of claustrum, further data are needed to better characterize the populations of interneurons of the claustrum as well as the circuitry it contributes to. In particular, information about the three-dimensional arrangement of neuron arborization within the claustrum is needed to better classify neurons on the basis of their shape. In this light, some elements of the work-flow designed in this PhD thesis was adopted to clarify human claustrum thick slices, as a starting point to unravel the micro-circuitry of the human claustrum.

## **6.3 A starting point to unravel the mystery of the human claustrum**

### **6.3.1 Materials and Methods**

**Tissue harvesting and treatment** Brain samples (i.e. both left and right claustra) were taken from a male patient, who did not suffered from any type of neurological or psychiatric illness. The samples consisted of approximately 5 cm-thick blocks which included both the insular and temporal subunits of the claustrum, surrounded by portions of the adjoining structures (extreme and external capsules, insular cortex and putamen). The samples were identified by qualified pathologists at the "Santa Chiara" Hospital of the University of Pisa. The brain was removed for routine diagnostic purposes, following a procedure approved by the Local Ethics Committee.

The blocks were optimally clarified as detailed in Chapter 2. In particular, the blocks were washed once a day with 20 mL of PBS enriched



with nadroparin calcium. Then, samples were put in a falcon with 35 mL of hydrogel for 9 days, with fresh solution every three days to allow hydrogel penetration inside the tissue. After hydrogel polymerization, n=20 500  $\mu\text{m}$ -thick slices per claustrum were obtained using a vibratome. As demonstrated in Chapter 2, in order to reach the best trade-off between protein loss and tissue clarification, slices were immersed in 10mL clearing solution for 9 days, with solution refreshed every 3 days.

**Immunostaining procedures and confocal acquisition** After the clarification step, claustrum slices were immersed in PBS 1X for 3 days, in order to remove the clearing solution residuals, gently shaking and refreshing the solution every 12 hours. Subsequently, n=10 claustrum samples were incubated with 10% of blocking solution, constituted by normal donkey serum with 0.1% of Triton-x, for 1 day at 37°C. Then, n=10 slices were incubated with mouse anti-calretinin monoclonal primary antibody (ABcam, Cambridge, UK) at 1:1000 dilution with 2% of normal donkey serum and 0.05% of Triton-x for 5 days at 37°C. Since calretinin is also a marker of small vessel endothelium, and the brain is highly vascularized, this was identified as a good benchmark assessing the antibody penetration into the sample. Primary antibody was washed off with PBS (2 x 24h at 37°C). Alexa Fluor 568 donkey anti-mouse secondary antibody was applied at a concentration of 1:500 and incubated at 37° for 2 days.

The remaining slices were incubated with 10% of blocking solution, constituted by normal goat serum with 0.1% of Triton-x, for 1 day at 37°C. Then, the slices were incubated with mouse anti-parvalbumin monoclonal primary antibody (ABcam, Cambridge, UK) at 1:1000 dilution with 2% of normal goat serum and 0.05% of Triton-x for 5 days at 37°C. Primary antibody was washed off with PBS (2 x 24h at 37°C). Alexa Fluor 488 anti-mouse secondary antibody was applied at a concentration of 1:500

Table 6.1: Confocal acquisition settings for 500 $\mu\text{m}$  thick claustrum slices, immuno-stained with anti-calretinin and anti-parvalbumin antibodies.

<i>Parameters [Units]</i>	<i>Values for slices immuno-stained with anti-calretinin</i>	<i>Values for slices immuno-stained with anti-parvalbumin</i>
Magnitude	10 x	20 x
Grid [pixel x pixel]	512 x 512	512 x 512
Pixel size [ $\mu\text{m}/\text{pixel}$ ]	2.46	1.24
Laser Power [pW]	15.1	21.9
Emission Wavelength [nm]	561	488
z-step [ $\mu\text{m}$ ]	5	2.5

and incubated at 37° for 2 days. Tissue was finally washed with PBS (2 x 24h at 37°C) to remove secondary antibody excess.

For each clarified slice, m=3 confocal stacks were acquired with a Nikon A1 confocal microscope. The acquisition settings for both the immuno-staining are summarised in Table 6.1.

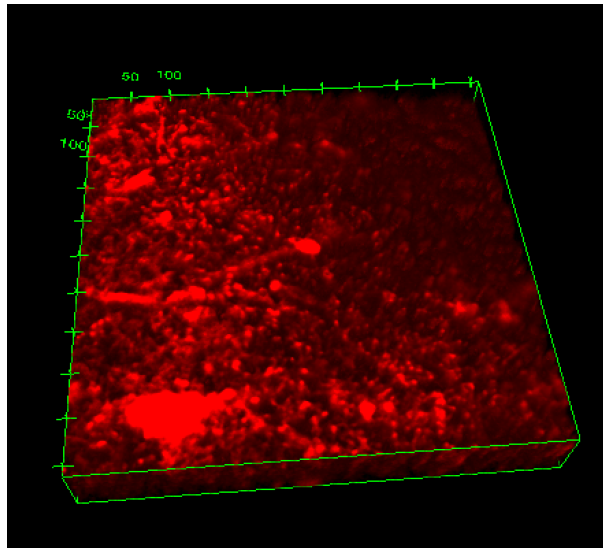
During acquisition, no limits were imposed to the depth of the datasets, thus the height of different Z-Stacks is variable for each acquisition and dependent on biological variability (i.e. the different spatial distribution of the neurons in the claustrum sections).

**Neuron tracing** The SmRG algorithm was used to trace single interneurons from the confocal slices immuno-stained with the anti-parvalbumin antibody. The range of radii (i.e. the first step of the SmRG algorithm, to find the soma and start the Smart Region Growing procedures using the soma center as seed) was obtained manually from the 2D images with ImageJ [1]. In particular, the image processing work-flow explained in

the Section 5.2.1 for the Feret's diameter evaluation was performed. As only one human sample was harvested, statistically relevant analyses about interneuron classification on the basis of their shape cannot be made. For this reason, the last step of the work-flow designed during this PhD thesis (i.e. the morphometric analysis using N3MO) was not performed.

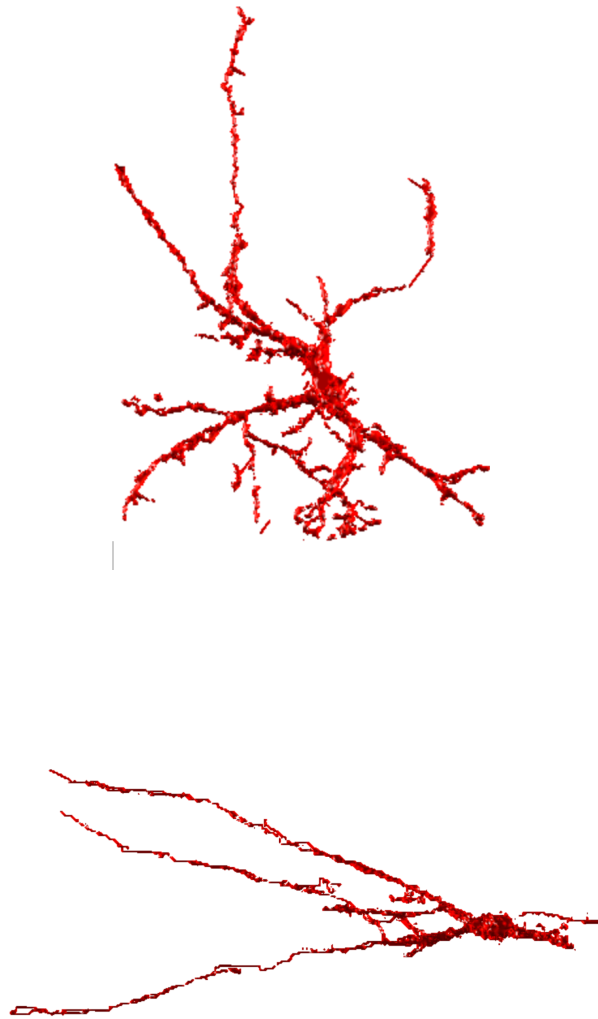
### 6.3.2 Results

An example of confocal datasets representing calretinin positive components is shown in Figure 6.3. Although the whole thickness of the slices cannot be acquired with a confocal microscope, the heights of the volumes acquired are about 200  $\mu\text{m}$ , which is higher than the penetration depth usually obtained with confocal microscopy techniques [21].



*Figure 6.3: Volume view of a confocal stack representing calretinin positive components (Em/Ex: 568/603 pixel-to micron ratio size: 2.46  $\mu\text{m}$ , z-resolution: 5  $\mu\text{m}$ ). Volume dimensions (w\*t\*h): 1259\*1259\*196  $\mu\text{m}$ .*

As regards the parvalbumin positive interneurons, Figure 6.4 shows two examples of parvalbumin-immunoreactive interneurons traced with the SmRG algorithm.



*Figure 6.4: Two examples of parvalbumin-immunoreactive interneuron traced with the SmRG algorithm.*

### 6.3.3 Discussion

This study aimed to proof the feasibility of applying the work-flow designed in this thesis on autoptic human brain samples. As discussed in Chapter 2, the main roadblocks for this study are linked to the impossibility to perfuse an entire human brain, to remove blood and to allow the hydrogel penetration through the samples, and the need of immunolabelling thick clarified brain slices. In fact, as demonstrated in Chapter 2, the clarification efficacy is lower than for slices from perfused animals. Moreover, since immunolabelling is performed through passive diffusion, the process depends strongly on antibody dimension (according to the Stoke-Einstein equation). A further obstacle is the difficulty in obtaining autoptic samples for clarification.

Results show that the passive CLARITY technique together with the image processing algorithms implemented during this thesis could be useful tools for the study of claustral micro-architecture. However, different parts of the work-flow customized for un-perfusable tissues have to be improved:

1. **Hydrogel diffusion through the tissue:** as discussed in Chapter 2, the incubation timing for the hydrogel embedding used during this PhD thesis is that reported in Liu et al. [59]. There are no studies assessing the fully penetration of the hydrogel inside the brain.
2. **Immuno-labelling protocol:** although CLARITY is compatible with immuno-fluorescence labelling procedures, in the literature there are no protocols customized for staining clarified thick slices. Future developments could include the measure of the diffusion coefficient of an antibody through a clarified brain sections, to calculate the characteristic time for diffusion, so as to be sure that the

immuno-staining involved the whole slice. Moreover, an immuno-labelling protocol optimization could be important to increase both Signal-to-Noise and Contrast-to-noise ratio.

3. **Confocal acquisition settings:** as discussed in Chapter 3, a standardization of the confocal acquisition may help a better neuron reconstruction with the SmRG algorithm developed during this thesis, since the neuron discrimination is pixel intensity-based.

In addition, future developments could include the increasing of the number of samples, in order to obtain statistically relevant results on neuron classification on the basis of their native shape inside the claustrum.

## 6.4 Conclusion

There are many reasons why investigators have decided to expend their energy on studying a particular nucleus in the brain. Sometimes the choice of structures has little to do with new insights that may be gleaned but is more attributable to the tractability of the site to experimental manipulation. However, some sites remain relatively obscure because their structure almost seems designed to impede research. The claustrum belongs to the latter group. Over the past decade there has been a resurgence in interest in the claustrum. This renewed attention is in large part attributable to a paper by Crick and Koch [243], which advanced the hypothesis that the claustrum plays a central role in binding and consciousness. After this review, a wealth of data has amassed on this nucleus and a huge number of papers has been published over the years (see Figure 6.5).

However, much of this data is disparate and contentious; conflicting views regarding the claustrum's structural definition and possible function abound, so its role in the brain is still enigmatic. Since it is crucial

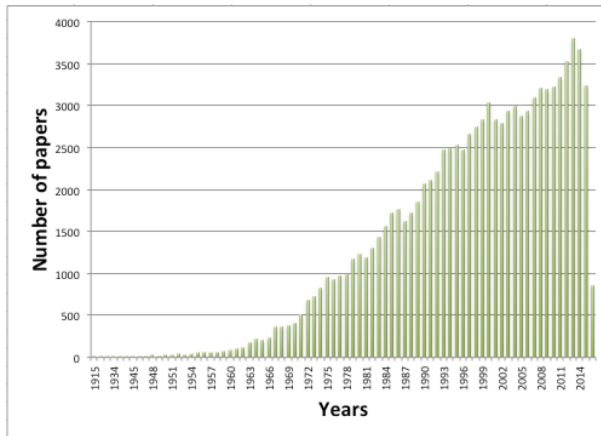


Figure 6.5: Number of publications by year on the claustrum (according to PUBMED <http://www.ncbi.nlm.nih.gov/pubmed>)

to understand the topological and morphological organization of the nucleus for unravelling claustrum function, this Chapter would be a starting point to characterize claustrum micro-structure. In particular, the morphology of parvalbumin-immunoreactive neurons was firstly analysed in dog claustrum thin slices, using standard histological and imaging techniques, to demonstrate the possibility to classify neurons on the basis of their shape. Since 2D images do not allow the reconstruction of the neurites, some elements of the work-flow designed in this PhD thesis were applied to autaptic human claustrum thick slices. Despite the gaps to be filled regarding immuno-staining procedures and datasets acquisitions, the method presented seem to be more objective than those commonly used to classify neurons, which are prone to human bias since they just use visual inspection. For this reason, the method presented in this thesis may be useful to collect further data to quantitatively characterize the population of neurons of the claustrum.



---

<sup>1</sup>Some of the results presented in this chapter have been published in :  
Pirone et al., "Parvalbumin expression in the claustrum of the adult dog. An immunohistochemical and topographical study with comparative notes on the structure of the nucleus" , *Journal of Chemical Neuroanatomy* (2015), doi:10.1016/j.aanat.2016.02.009







# Conclusions

The aim of my thesis was to develop an innovative and rigorous work-flow for the quantitative analysis of brain micro-architecture, that integrates optimization of delipidation protocols and imaging algorithms to trace single neurons and to extract morphological parameters of interest from confocal datasets. Since it is well known that neuronal morphology at the micro-structural level is important for higher level brain function, the designed work-flow could be relevant for the study of diseases correlated to neuronal abnormalities, as well as the structure-function relationship in dendritic trees.

The work-flow operates in three main steps: i) CLARITY protocol optimization for thick brain slices, ii) implementation of a Smart Region Growing algorithm to trace single neurons from clarified slices and iii) development of a tool, N3MO, for the automatic extraction of morphological variables characterizing neuron shape and complexity in their native arrangement within the brain.

As regards the first step, it was demonstrated in this thesis that the trade-off between tissue transparency and the presence of molecules of interest to imaging could be considered a good index of clarification efficacy. For a given clearing cocktail, the former increases with clearing time, while the latter are inevitably lost due to a shift in equilibrium between tissue bound and unbound moieties or protein degradation.

After identifying the best clarification time, an innovative method for tracing neuron structures in confocal datasets from clarified slices was developed. Since the SmRG approach is based on local features of the image intensity value histogram to distinguish the signal (i.e. neurons) from the background, the algorithm is able to satisfactorily trace neurons in confocal microscopy images. Preliminary results showed that the SmRG algorithm can isolate single neurons with their characteristic structure.

The tracing algorithm was then integrated in N3MO, an open-source tool implemented during this PhD thesis, which analyses three-dimensional morphology of neurons within the brain. It consists of a set of computation algorithms written in Matlab and implemented in a GUI framework, in which it is easy to trace neurons, extract morphological features of interest and access the data to have a global view of the results. To test the performance of the work-flow, two cases studies were analysed.

Firstly, the sexual dimorphism in animal models of autism (i.e. REELER and Engrailed2 mouse strains) was investigated. In particular, a quantitative characterization of Purkinje cell morphology within the cerebellar cortex was performed, in order to extract discriminating features of both gender and autism. As a starting point, standard protocols for tissue treatment and imaging were used to assess the feasibility of the study. The results suggested that there is a more chaotic topological organization of Purkinje cells within the cerebellum in autistic RELN+/- male individuals. However, the 2D investigation may be flawed because it cannot faithfully represent neuron morphology. For this reason, the work-flow designed in this PhD thesis was applied to a more promising model of autism, the Engrailed2 mouse. Although the number of samples analysed was limited, the data demonstrated that PCs from this model of autism

were likely to be less arborized than the control mice. Moreover, within a specific genotype, males and females present the same arborization complexity. Further studies on the 3D morphology of PCs in animal models of autism could help to better understand their micro-structure, to improve the knowledge of autism and its presumed male bias, to define new diagnostic strategies as well as to develop new therapeutic approaches. As regards the gender difference, PCs from female individuals were characterized by smaller somata and higher radial extension than male ones. These findings could have implications for developmental studies that could directly test hypotheses about mechanisms relating sex steroid hormones to sexual dimorphisms.

Some of the elements of the work-flow were also applied to characterize human claustrum micro-structure: understanding the topological arrangement of the neurons, as well as classifying the neurons on the basis of their shape, could be crucial for unravelling the function of this enigmatic nucleus. I focused the study on the evaluation of parvalbumin-immunoreactive interneurons, since they seem to play a crucial role in the inhibitory circuits providing a substrate for local information processing. After a proof of concept, demonstrating that it is possible to classify interneurons in thin slices of dog claustrum on the basis of soma shape and size, human thick sections were clarified and immuno-stained to fully evaluate their morphology. For this thesis only an autoptic sample was available, so the number of replies for a statistically relevant study cannot be guaranteed. In further studies, the number of claustra analysed will be increased, in order to classify parvalbumin-immuno-reactive neurons. Moreover, the characterization of the human claustrum could also include the study of glia cells or vessels, in order to fully delineate the micro-structure of the nucleus.

In conclusion, this thesis constitutes a framework for a rigorous and quantitative approach to study brain micro-architecture. The approach described can be used to better understand lifespan alterations in neural structure in neuro-developmental disorders, as well as to study the brain structure-function relationship.



# List of Publications

## Peer reviewed papers

L Billeci, C Magliaro, G Pioggia, A Ahluwalia, *NEuron MORphological analysis tool: open-source software for quantitative morphometrics*, *Frontiers in Neuroinformatics* (2013) 7: 2. doi: 10.3389/fninf.2013.00002

A Tirella, C Magliaro, M Penta, M Troncone, R Pimentel, A Ahluwalia, *Sphyga: a multiparameter open-source tool for fabricating smart and tunable hydrogel microbeads*, *Biofabrication* (2014) 6(2) doi: 10.1088/1758-5082/6/2/025009

C Magliaro, A Tirella, G Mattei, A Pirone, A Ahluwalia, *HisTOOLogy: an open source tool for quantitative analysis of histological sections*, *Journal of Microscopy* (2015) 60(3):260-7. doi: 10.1111/jmi.12292

G Mattei, I Cristiani, C Magliaro, A Ahluwalia, *Profile analysis of hepatic porcine and murine brain tissue slices obtained with a vibratome*, *PeerJ* (2015) 3:e932. doi: 10.7717/peerj.932

A Pirone, C Magliaro, E Giannessi, A Ahluwalia, *Parvalbumin expression in the claustrum of the adult dog. An immunohistochemical and topographical study with comparative notes on the structure of the nucleus*, *Journal of Chemical*

Neuroanatomy (2015) 64-65:33-42. doi: 10.1016/j.jchemneu.2015.02.004.

C Magliaro, C Cocito, S Bagatella, A Merighi, A Ahluwalia, L Lossi, *The number of Purkinje neurons and their topology in the cerebellar vermis of normal and reln haplodeficient mouse*, Annals of Anatomy- Anatomischer Anzeiger (2016), doi:10.1016/j.aanat.2016.02.009.

C Magliaro, A L Callara, G Mattei, M Morcinelli, C Viaggi, F Vaglini, A Ahluwalia, *Clarifying CLARITY: optimization of the delipidation protocol for labelled tissue*, Frontiers in Neuroscience - Brain Imaging Methods, April 2016, <http://dx.doi.org/10.3389/fnins.2016.00179>.

## Conference Proceedings

C Magliaro, T Sbrana, J Spencer-Fry, T Toimela, A. Ahluwalia, *Integration of a fluidic system with an imaging platform: image quality analysis and real time monitoring of cell morphology*, TERMIS-EU 2014, Genova, Italy (poster session)

C Magliaro, A Tirella, A Ahluwalia, *HisTOOLogy: an user-friendly tool for quantitative stain detection in histological slices*, Congresso del Gruppo Nazionale di Bioingegneria (GNB2014), Pavia, Italy (poster session)

C Magliaro, S Giusti, V Di Patria, A Ahluwalia, *Observing a Biological Hypercube: a preliminary study*, Bioimaging Symposium 2014, Porto, Portugal (oral presentation)

C Magliaro, S Giusti, V Di Patria, A Ahluwalia, *Observing a Biological Hypercube: a preliminary study*, Bioimaging Symposium 2014, Porto, Portugal (oral presentation)

C Magliaro, S Giusti, V Di Patria, A Ahluwalia, *Journey to the center of a biological hypercube*, Kirkstall conference on in-vivo alternatives 2015, Pisa, Italy (oral presentation)

A L Callara, M Morcinelli, C Magliaro, G Mattei, C Viaggi, F Vaglini, A Ahluwalia, *Optimization of the Clarity clarifying protocol for L7GFP mice cerebellum*, Kirkstall conference on in-vivo alternatives 2015, Pisa, Italy (poster session)

A L Callara, C Magliaro, V Positano, N Vanello, A Ahluwalia, *Tracing single neurons from mouse cerebellum clarified tissue*, Congresso del Gruppo Nazionale di Bioingegneria (GNB2016), Naples, Italy (poster session)

G Mattei, C Magliaro, S D Ramachandran, B Muenst, J Braspenning, A. Ahluwalia, *Liver organoid formation in-vitro: what triggers cell self-assembly?*, TERMIS-EU 2016, Uppsala, Sweden (poster session)



# Bibliography

- [1] Caroline A Schneider, Wayne S Rasband, Kevin W Eliceiri, et al. Nih image to imagej: 25 years of image analysis. *Nat methods*, 9(7):671–675, 2012.
- [2] Vasilis Ntziachristos. Going deeper than microscopy: the optical imaging frontier in biology. *Nature methods*, 7(8):603–614, 2010.
- [3] Tiago A Ferreira, Arne V Blackman, Julia Oyrer, Sriram Jayabal, Andrew J Chung, Alanna J Watt, P Jesper Sjöström, and Donald J van Meyel. Neuronal morphometry directly from bitmap images. *Nature methods*, 11(10):982–984, 2014.
- [4] A Paul Alivisatos, Miyoung Chun, George M Church, Ralph J Greenspan, Michael L Roukes, and Rafael Yuste. The brain activity map project and the challenge of functional connectomics. *Neuron*, 74(6):970–974, 2012.
- [5] Arnaud Messé, David Rudrauf, Habib Benali, and Guillaume Marrelec. Relating structure and function in the human brain: relative contributions of anatomy, stationary dynamics, and non-stationarities. *PLoS Comput Biol*, 10(3):e1003530, 2014.
- [6] Edward L White. Reflections on the specificity of synaptic connections. *Brain research reviews*, 55(2):422–429, 2007.
- [7] Julian ML Budd, Hermann Cuntz, Stephen J Eglon, and Patrik Krieger. Editorial: Quantitative analysis of neuroanatomy. *Frontiers in neuroanatomy*, 9, 2015.
- [8] Allan T Gullledge, Björn M Kampa, and Greg J Stuart. Synaptic integration in dendritic trees. *Journal of neurobiology*, 64(1):75–90, 2005.
- [9] Yuh-Nung Jan and Lily Yeh Jan. The control of dendrite development. *Neuron*, 40(2):229–242, 2003.
- [10] Rachel OL Wong and Anirvan Ghosh. Activity-dependent regulation of dendritic growth and patterning. *Nature reviews neuroscience*, 3(10):803–812, 2002.
- [11] S Hossein Fatemi, Amy R Halt, Joel M Stary, Reena Kanodia, S Charles Schulz, and George R Realmutto. Glutamic acid decarboxylase 65 and 67 kda proteins are reduced in autistic parietal and cerebellar cortices. *Biological psychiatry*, 52(8):805–810, 2002.

- [12] Brian H Anderton, Linda Callahan, Paul Coleman, Peter Davies, Dorothy Flood, Gregory A Jicha, Thomas Ohm, and Charles Weaver. Dendritic changes in alzheimer's disease and factors that may underlie these changes. *Progress in neurobiology*, 55(6):595–609, 1998.
- [13] Erik Meijering. Neuron tracing in perspective. *Cytometry Part A*, 77(7):693–704, 2010.
- [14] Katherine S Button, John PA Ioannidis, Claire Mokrysz, Brian A Nosek, Jonathan Flint, Emma SJ Robinson, and Marcus R Munafò. Power failure: why small sample size undermines the reliability of neuroscience. *Nature Reviews Neuroscience*, 14(5):365–376, 2013.
- [15] Brian A Wilt, Laurie D Burns, Eric Tatt Wei Ho, Kunal K Ghosh, Eran A Mukamel, and Mark J Schnitzer. Advances in light microscopy for neuroscience. *Annual review of neuroscience*, 32:435, 2009.
- [16] Ali Ertürk, Klaus Becker, Nina Jährling, Christoph P Mauch, Caroline D Hojer, Jackson G Egen, Farida Hellal, Frank Bradke, Morgan Sheng, and Hans-Ulrich Dodt. Three-dimensional imaging of solvent-cleared organs using 3disco. *Nature protocols*, 7(11):1983–1995, 2012.
- [17] Hiroshi Hama, Hiroshi Kurokawa, Hiroyuki Kawano, Ryoko Ando, Tomomi Shimogori, Hisayori Noda, Kiyoko Fukami, Asako Sakaue-Sawano, and Atsushi Miyawaki. Scale: a chemical approach for fluorescence imaging and reconstruction of transparent mouse brain. *Nature neuroscience*, 14(11):1481–1488, 2011.
- [18] Takaaki Kuwajima, Austen A Sitko, Punita Bhansali, Chris Jurgens, William Guido, and Carol Mason. Clear: a detergent-and solvent-free clearing method for neuronal and non-neuronal tissue. *Development*, 140(6):1364–1368, 2013.
- [19] Meng-Tsen Ke, Satoshi Fujimoto, and Takeshi Imai. Seedb: a simple and morphology-preserving optical clearing agent for neuronal circuit reconstruction. *Nature neuroscience*, 16(8):1154–1161, 2013.
- [20] Kwanghun Chung and Karl Deisseroth. Clarity for mapping the nervous system. *Nature methods*, 10(6):508–513, 2013.
- [21] Kwanghun Chung, Jenelle Wallace, Sung-Yon Kim, Sandhiya Kalyanasundaram, Aaron S Andalman, Thomas J Davidson, Julie J Mirzabekov, Kelly A Zalocusky, Joanna Mattis, Aleksandra K Denisin, et al. Structural and molecular interrogation of intact biological systems. *Nature*, 497(7449):332–337, 2013.
- [22] Ekaterina Poguzhelskaya, Dmitry Artamonov, Anastasia Bolshakova, Olga Vlasova, and Ilya Bezprozvanny. Simplified method to perform clarity imaging. *Molecular neurodegeneration*, 9(1):1–5, 2014.
- [23] Sayan Mukherjee, Barry Condrón, and Scott T Acton. Chasing the neurome: Segmentation and comparison of neurons. In *Signal Processing Conference (EUSIPCO), 2013 Proceedings of the 21st European*, pages 1–4. IEEE, 2013.
- [24] Sreetama Basu, Barry Condrón, Alla Aksel, and Scott T Acton. Segmentation and tracing of single neurons from 3d confocal microscope images. *Biomedical and Health Informatics, IEEE Journal of*, 17(2):319–335, 2013.
- [25] Michael Kass, Andrew Witkin, and Demetri Terzopoulos. Snakes: Active contour models. *International journal of computer vision*, 1(4):321–331, 1988.
- [26] Stanley Osher and James A Sethian. Fronts propagating with curvature-dependent speed: algorithms based on hamilton-jacobi formulations. *Journal of computational physics*, 79(1):12–49, 1988.
- [27] Luminita A Vese and Tony F Chan. A multiphase level set framework for image segmentation using the mumford and shah model. *International journal of computer vision*, 50(3):271–293, 2002.

- [28] Nikos Paragios, Olivier Mellina-Gottardo, and Visvanathan Ramesh. Gradient vector flow fast geodesic active contours. In *Computer Vision, 2001. ICCV 2001. Proceedings. Eighth IEEE International Conference on*, volume 1, pages 67–73. IEEE, 2001.
- [29] Andreas Wolf, Andreas Herzog, Soeren Westerholz, Bernd Michaelis, and T Voigt. Improving fuzzy-based axon segmentation with genetic algorithms: the ieee congress on evolutionary computation. In *Evolutionary Computation, 2009. CEC'09. IEEE Congress on*, pages 1025–1031. IEEE, 2009.
- [30] Anca Dima, Michael Scholz, and Klaus Obermayer. Automatic segmentation and skeletonization of neurons from confocal microscopy images based on the 3-d wavelet transform. *Image Processing, IEEE Transactions on*, 11(7):790–801, 2002.
- [31] Jacob R Glaser and Edmund M Glaser. Neuron imaging with neuroLucida: a pc-based system for image combining microscopy. *Computerized Medical Imaging and Graphics*, 14(5):307–317, 1990.
- [32] Torsten Rohlfing, Robert Brandt, Randolph Menzel, and Calvin R Maurer. Evaluation of atlas selection strategies for atlas-based image segmentation with application to confocal microscopy images of bee brains. *NeuroImage*, 21(4):1428–1442, 2004.
- [33] Tingwei Quan, Hang Zhou, Jing Li, Shiwei Li, Anan Li, Yuxin Li, Xiaohua Lv, Qingming Luo, Hui Gong, and Shaoqun Zeng. NeuroGPS-tree: automatic reconstruction of large-scale neuronal populations with dense neurites. *Nature methods*, 13(1):51–54, 2016.
- [34] Li Wang, Lei He, Arabinda Mishra, and Chunming Li. Active contours driven by local gaussian distribution fitting energy. *Signal Processing*, 89(12):2435–2447, 2009.
- [35] Sabine K Schmitz, JJ Johannes Hjorth, Raoul MS Joemai, Rick Wijntjes, Susanne Eijgenraam, Petra de Bruijn, Christina Georgiou, Arthur PH de Jong, Arjen van Ooyen, Matthijs Verhage, et al. Automated analysis of neuronal morphology, synapse number and synaptic recruitment. *Journal of neuroscience methods*, 195(2):185–193, 2011.
- [36] Lucia Billeci, Chiara Magliaro, Giovanni Pioggia, and Arti Ahluwalia. Neuronmorphological analysis tool: open-source software for quantitative morphometrics. *Frontiers in neuroinformatics*, 7(2), 2013.
- [37] E Meijering, M Jacob, J-CF Sarria, PI Steiner, H Hirling, and M Unser. Design and validation of a tool for neurite tracing and analysis in fluorescence microscopy images. *Cytometry Part A*, 58(2):167–176, 2004.
- [38] Shinn-Ying Ho, Chih-Yuan Chao, Hui-Ling Huang, Tzai-Wen Chiu, Phasit Charoenkwan, and Eric Hwang. Neurphologyj: an automatic neuronal morphology quantification method and its application in pharmacological discovery. *Bmc Bioinformatics*, 12(1):230, 2011.
- [39] Martha L Narro, Fan Yang, Robert Kraft, Carola Wenk, Alon Efrat, and Linda L Restifo. Neuronmetrics: software for semi-automated processing of cultured neuron images. *Brain research*, 1138:57–75, 2007.
- [40] SL Wearne, A Rodriguez, DB Ehlenberger, AB Rocher, SC Henderson, and PR Hof. New techniques for imaging, digitization and analysis of three-dimensional neural morphology on multiple scales. *Neuroscience*, 136(3):661–680, 2005.
- [41] John C Gensel, David L Schonberg, Jessica K Alexander, Dana M McTigue, and Phillip G Popovich. Semi-automated sholl analysis for quantifying changes in growth and differentiation of neurons and glia. *Journal of neuroscience methods*, 190(1):71–79, 2010.
- [42] Tessie Paulose, Maël Montévil, Lucia Speroni, Florent Cerruti, Carlos Sonnenschein, and Ana M Soto. Sama: A method for 3d morphological analysis. *PLoS one*, 11(4):e0153022, 2016.

- [43] S Hossein Fatemi, Amy R Halt, George Realmuto, Julie Earle, David A Kist, Paul Thuras, and Amelia Merz. Purkinje cell size is reduced in cerebellum of patients with autism. *Cellular and molecular neurobiology*, 22(2):171–175, 2002.
- [44] Kathleen J Millen, Wolfgang Wurst, Karl Herrup, and Alexandra L Joyner. Abnormal embryonic cerebellar development and patterning of postnatal foliation in two mouse engrailed-2 mutants. *DEVELOPMENT-CAMBRIDGE-*, 120:695–695, 1994.
- [45] Barbara Kuemerle, Hadi Zanjani, Alexandra Joyner, and Karl Herrup. Pattern deformities and cell loss in engrailed-2mutant mice suggest two separate patterning events during cerebellar development. *The Journal of neuroscience*, 17(20):7881–7889, 1997.
- [46] Francis C Crick and Christof Koch. What is the function of the claustrum? *Philosophical Transactions of the Royal Society of London B: Biological Sciences*, 360(1458):1271–1279, 2005.
- [47] Ryan Remedios, Nikos K Logothetis, and Christoph Kayser. Unimodal responses prevail within the multisensory claustrum. *The Journal of Neuroscience*, 30(39):12902–12907, 2010.
- [48] Heiko Braak and Eva Braak. Neuronal types in the claustrum of man. *Anatomy and embryology*, 163(4):447–460, 1982.
- [49] Dimka V Hinova-Palova, Lawrence Edelstein, Boycho V Landzhov, Minko Minkov, Lina G Malinova, Alexandar Alexandrov, Stanislav Hristov, Adrian M Paloff, and Wladimir A Ovtcharoff. Light microscopic immunocytochemical identification of leucine enkephalin. *Scripta Scientifica Medica*, 45:23–28, 2013.
- [50] David C Van Essen and Kamil Ugurbil. The future of the human connectome. *Neuroimage*, 62(2):1299–1310, 2012.
- [51] Martin Oheim, Emmanuel Beaufrepaire, Emmanuelle Chaigneau, Jerome Mertz, and Serge Charpak. Two-photon microscopy in brain tissue: parameters influencing the imaging depth. *Journal of neuroscience methods*, 111(1):29–37, 2001.
- [52] Douglas S Richardson and Jeff W Lichtman. Clarifying tissue clearing. *Cell*, 162(2):246–257, 2015.
- [53] Raju Tomer, Li Ye, Brian Hsueh, and Karl Deisseroth. Advanced clarity for rapid and high-resolution imaging of intact tissues. *Nature protocols*, 9(7):1682–1697, 2014.
- [54] Jonathan R Epp, Yosuke Niibori, Hwa-Lin Liz Hsiang, Valentina Mercaldo, Karl Deisseroth, Sheena A Josselyn, and Paul W Frankland. Optimization of clarity for clearing whole-brain and other intact organs. *eneuro*, 2(3):ENEURO-0022, 2015.
- [55] Angela dEsposito, Daniil Nikitichev, Adrien Desjardins, Simon Walker-Samuel, and Mark F Lythgoe. Quantification of light attenuation in optically cleared mouse brains. *Journal of biomedical optics*, 20(8):080503–080503, 2015.
- [56] Hyunsu Lee, Jae-Hyung Park, Incheol Seo, Sun-Hyun Park, and Shin Kim. Improved application of the electrophoretic tissue clearing technology, clarity, to intact solid organs including brain, pancreas, liver, kidney, lung, and intestine. *BMC developmental biology*, 14(1):1, 2014.
- [57] Huiyuan Zheng and Linda Rinaman. Simplified clarity for visualizing immunofluorescence labeling in the developing rat brain. *Brain Structure and Function*, pages 1–9, 2015.
- [58] Bin Yang, Jennifer B Treweek, Rajan P Kulkarni, Benjamin E Deverman, Chun-Kan Chen, Eric Lubeck, Sheel Shah, Long Cai, and Viviana Gradinaru. Single-cell phenotyping within transparent intact tissue through whole-body clearing. *Cell*, 158(4):945–958, 2014.



- [59] Alan King Lun Liu, Madeleine ED Hurry, Olivia Tsz-Wa Ng, John DeFelice, HM Lai, RKB Pearce, G Wong, R Chang, SM Gentleman, et al. Bringing clarity to the human brain: visualization of lewy pathology in three dimensions. *Neuropathology and applied neurobiology*, 2015.
- [60] Xulun Zhang, Stephan L Baader, Feng Bian, Wolfgang Müller, and John Oberdick. High level purkinje cell specific expression of green fluorescent protein in transgenic mice. *Histochemistry and cell biology*, 115(6):455–464, 2001.
- [61] Giorgio Mattei, Irene Cristiani, Chiara Magliaro, and Arti Ahluwalia. Profile analysis of hepatic porcine and murine brain tissue slices obtained with a vibratome. *PeerJ*, 3:e932, 2015.
- [62] Ibtesam A Saeed and S Salman Ashraf. Denaturation studies reveal significant differences between gfp and blue fluorescent protein. *International journal of biological macromolecules*, 45(3):236–241, 2009.
- [63] Ralph Gonzalez and Richard Woods. *RTF] Digital Image Processing Using Matlab*. 2009.
- [64] Nobuyuki Otsu. A threshold selection method from gray-level histograms. *Automatica*, 11(285-296):23–27, 1975.
- [65] Xiaomei Song, Brian W Pogue, Shudong Jiang, Marvin M Doyley, Hamid Dehghani, Tor D Tosteson, and Keith D Paulsen. Automated region detection based on the contrast-to-noise ratio in near-infrared tomography. *Applied optics*, 43(5):1053–1062, 2004.
- [66] Christine V Sapan, Roger L Lundblad, and Nicholas C Price. Colorimetric protein assay techniques. *Biotechnology and applied Biochemistry*, 29(2):99–108, 1999.
- [67] Clara M Cheng, George Joncas, Rickey R Reinhardt, Robert Farrer, Richard Quarles, Jeremy Janssen, Michael P McDonald, Jacqueline N Crawley, Lynn Powell-Braxton, and Carolyn A Bondy. Biochemical and morphometric analyses show that myelination in the insulin-like growth factor 1 null brain is proportionate to its neuronal composition. *The Journal of neuroscience*, 18(15):5673–5681, 1998.
- [68] RM Grossfeld and EM Shooter. A study of the changes in protein composition of mouse brain during ontogenetic development1. *Journal of neurochemistry*, 18(12):2265–2277, 1971.
- [69] Jeff W Lichtman and Winfried Denk. The big and the small: challenges of imaging the brains circuits. *Science*, 334(6056):618–623, 2011.
- [70] Moritz Helmstaedter and Partha P Mitra. Computational methods and challenges for large-scale circuit mapping. *Current opinion in neurobiology*, 22(1):162–169, 2012.
- [71] Duncan E Donohue and Giorgio A Ascoli. Automated reconstruction of neuronal morphology: an overview. *Brain research reviews*, 67(1):94–102, 2011.
- [72] Michel Laurent, Georges Johannin, Nathalie Gilbert, Laurent Lucas, Doris Cassio, Patrice X Petit, and Anne Fleury. Power and limits of laser scanning confocal microscopy. *Biology of the Cell*, 80(2-3):229–240, 1994.
- [73] Wai-Fung Cheong, Scott A Prahl, Ashley J Welch, et al. A review of the optical properties of biological tissues. *IEEE journal of quantum electronics*, 26(12):2166–2185, 1990.
- [74] Jurek W Dobrucki. Confocal microscopy: quantitative analytical capabilities. *Cytometry: New Developments*, 75:41, 2004.
- [75] Jurek W Dobrucki, Dorota Feret, and Anna Noatynska. Scattering of exciting light by live cells in fluorescence confocal imaging: phototoxic effects and relevance for frap studies. *Biophysical journal*, 93(5):1778–1786, 2007.

- [76] YQ Guan, YY Cai, X Zhang, YT Lee, and M Opas. Adaptive correction technique for 3d reconstruction of fluorescence microscopy images. *Microscopy Research and Technique*, 71(2):146–157, 2008.
- [77] Hanchuan Peng, Zongcai Ruan, Fuhui Long, Julie H Simpson, and Eugene W Myers. V3d enables real-time 3d visualization and quantitative analysis of large-scale biological image data sets. *Nature biotechnology*, 28(4):348–353, 2010.
- [78] Engin Türetken, Germán González, Christian Blum, and Pascal Fua. Automated reconstruction of dendritic and axonal trees by global optimization with geometric priors. *Neuroinformatics*, 9(2-3):279–302, 2011.
- [79] Ting Zhao, Jun Xie, Fernando Amat, Nathan Clack, Parvez Ahammad, Hanchuan Peng, Fuhui Long, and Eugene Myers. Automated reconstruction of neuronal morphology based on local geometrical and global structural models. *Neuroinformatics*, 9(2-3):247–261, 2011.
- [80] Paarth Chothani, Vivek Mehta, and Armen Stepanyants. Automated tracing of neurites from light microscopy stacks of images. *Neuroinformatics*, 9(2-3):263–278, 2011.
- [81] Tim J Atherton and Darren J Kerbyson. Size invariant circle detection. *Image and Vision computing*, 17(11):795–803, 1999.
- [82] Michelle E Dunn, Karl Schilling, and E Mugnaini. Development and fine structure of murine purkinje cells in dissociated cerebellar cultures: dendritic differentiation, synaptic maturation, and formation of cell-class specific features. *Anatomy and embryology*, 197(1):31–50, 1997.
- [83] V Chan-Palay and E Asan. Alterations in catecholamine neurons of the locus coeruleus in senile dementia of the alzheimer type and in parkinson’s disease with and without dementia and depression. *Journal of comparative neurology*, 287(3):373–392, 1989.
- [84] Oscar Solis, Daniel I Limón, Jorge Flores-Hernández, and Gonzalo Flores. Alterations in dendritic morphology of the prefrontal cortical and striatum neurons in the unilateral 6-ohda-rat model of parkinson’s disease. *Synapse*, 61(6):450–458, 2007.
- [85] Clifford B Saper, Dwight C German, and Charles L White. Neuronal pathology in the nucleus basalis and associated cell groups in senile dementia of the alzheimer’s type possible role in cell loss. *Neurology*, 35(8):1089–1089, 1985.
- [86] SJ Allen, D Dawbarn, and GK Wilcock. Morphometric immunochemical analysis of neurons in the nucleus basalis of meynert in alzheimer’s disease. *Brain research*, 454(1-2):275–281, 1988.
- [87] Paul D Coleman and Dorothy G Flood. Neuron numbers and dendritic extent in normal aging and alzheimer’s disease. *Neurobiology of aging*, 8(6):521–545, 1987.
- [88] Shira Knafo, Cesar Venero, Paula Merino-Serrais, Isabel Fernaud-Espinosa, Juncal Gonzalez-Soriano, Isidro Ferrer, Gabriel Santpere, and Javier DeFelipe. Morphological alterations to neurons of the amygdala and impaired fear conditioning in a transgenic mouse model of alzheimer’s disease. *The Journal of pathology*, 219(1):41–51, 2009.
- [89] Jingru Hu, Keith T Akama, Grant A Krafft, Brett A Chromy, and Linda J Van Eldik. Amyloid- $\beta$  peptide activates cultured astrocytes: morphological alterations, cytokine induction and nitric oxide release. *Brain research*, 785(2):195–206, 1998.
- [90] Grazyna Rajkowska, Lynn D Selemon, and Patricia S Goldman-Rakic. Neuronal and glial somal size in the prefrontal cortex: a postmortem morphometric study of schizophrenia and huntington disease. *Archives of General Psychiatry*, 55(3):215–224, 1998.

- [91] Gloria J Klapstein, Robin S Fisher, Hadi Zanjani, Carlos Cepeda, Eve S Jokel, Marie-Françoise Chesselet, and Michael S Levine. Electrophysiological and morphological changes in striatal spiny neurons in r6/2 huntington's disease transgenic mice. *Journal of neurophysiology*, 86(6):2667–2677, 2001.
- [92] Renata P Lerner, G Luz del Carmen, Chundi Zhu, Marie-Françoise Chesselet, and Miriam A Hickey. Striatal atrophy and dendritic alterations in a knock-in mouse model of huntington's disease. *Brain research bulletin*, 87(6):571–578, 2012.
- [93] Taihung Duong, Harold Robinson, Donald Guthrie BA, and Anne Ritvo. Lower purkinje cell counts in the cerebella of four autistic subjects: initial findings of the ucla-nsac autopsy research report. *Am J Psychiatry*, 143(7):862–866, 1986.
- [94] Konstantinos Xylouris, Gillian Queisser, and Gabriel Wittum. A three-dimensional mathematical model of active signal processing in axons. *Computing and visualization in science*, 13(8):409–418, 2010.
- [95] Robert A McDougal and Gordon M Shepherd. 3d-printer visualization of neuron models. *Frontiers in neuroinformatics*, 9, 2015.
- [96] Kerry M Brown, Todd A Gillette, and Giorgio A Ascoli. Quantifying neuronal size: summing up trees and splitting the branch difference. In *Seminars in cell & developmental biology*, volume 19, pages 485–493. Elsevier, 2008.
- [97] Xinyu Zhao, ChangHui Pak, Richard D Smrt, and Peng Jin. Epigenetics and neural developmental disorders. *Epigenetics*, 2(2):126–134, 2007.
- [98] Y CAJAL S RAMON. Structure and connections of neurons. *Bulletin of the Los Angeles Neurological Society*, 17(1-2):5, 1952.
- [99] C Golgi and Naomi Geller Lipsky. On the structure of nerve cells. *Journal of microscopy*, 155(1):3–7, 1989.
- [100] Josef P Kapfhammer. Cellular and molecular control of dendritic growth and development of cerebellar purkinje cells. *Progress in histochemistry and cytochemistry*, 39(3):131–182, 2004.
- [101] Yoshiyasu Arai, Yoko Momose-Sato, Katsushige Sato, and Kohtarō Kamino. Optical mapping of neural network activity in chick spinal cord at an intermediate stage of embryonic development. *Journal of neurophysiology*, 81(4):1889–1902, 1999.
- [102] Pablo Blinder, Itay Baruchi, Vladislav Volman, Herbert Levine, Danny Baranes, and Eshel Ben Jacob. Functional topology classification of biological computing networks. *Natural Computing*, 4(4):339–361, 2005.
- [103] Vladislav Volman, Itay Baruchi, and Eshel Ben-Jacob. Manifestation of function-follow-form in cultured neuronal networks. *Physical biology*, 2(2):98, 2005.
- [104] Thomas Knöpfel, Javier Díez-García, and Walther Akemann. Optical probing of neuronal circuit dynamics: genetically encoded versus classical fluorescent sensors. *Trends in neurosciences*, 29(3):160–166, 2006.
- [105] John O'Brien and Nigel Unwin. Organization of spines on the dendrites of purkinje cells. *Proceedings of the National Academy of Sciences*, 103(5):1575–1580, 2006.
- [106] Kyle P Lillis, Alfred Eng, John A White, and Jerome Mertz. Two-photon imaging of spatially extended neuronal network dynamics with high temporal resolution. *Journal of neuroscience methods*, 172(2):178–184, 2008.

- [107] Michael Kerschnitzki, Philip Kollmannsberger, Manfred Burghammer, Georg N Duda, Richard Weinkamer, Wolfgang Wagermaier, and Peter Fratzl. Architecture of the osteocyte network correlates with bone material quality. *Journal of bone and mineral research*, 28(8):1837–1845, 2013.
- [108] Harry BM Uylings and Jaap van Pelt. Measures for quantifying dendritic arborizations. *Network: Computation in Neural Systems*, 13(3):397–414, 2002.
- [109] Orit Shefi, Sharon Golebowicz, Eshel Ben-Jacob, and Amir Ayali. A two-phase growth strategy in cultured neuronal networks as reflected by the distribution of neurite branching angles. *Journal of neurobiology*, 62(3):361–368, 2005.
- [110] D A Sholl. Dendritic arborization in the neurons of the visual and motor cortices of the cat. *Journal of Anatomy*, 87(4):387–406, 1953.
- [111] The sholl analysis of neuronal cell images: Semi-log or log-log method? *Journal of Theoretical Biology*, 245(1):130 – 140, 2007.
- [112] Peter T Tsai, Court Hull, YunXiang Chu, Emily Greene-Colozzi, Abbey R Sadowski, Jarrett M Leech, Jason Steinberg, Jacqueline N Crawley, Wade G Regehr, Mustafa Sahin, et al. Autistic-like behaviour and cerebellar dysfunction in purkinje cell tsc1 mutant mice. *Nature*, 488(7413):647–651, 2012.
- [113] MF Papia, MW Burke, S Zangenehpour, RM Palmour, FR Ervin, and Maurice Ptito. Reduced soma size of the m-neurons in the lateral geniculate nucleus following foetal alcohol exposure in non-human primates. *Experimental brain research*, 205(2):263–271, 2010.
- [114] Thanathom Chailangkarn, Allan Acab, and Alysson Renato Muotri. Modeling neurodevelopmental disorders using human neurons. *Current opinion in neurobiology*, 22(5):785–790, 2012.
- [115] Pascal Vallotton, Ryan Lagerstrom, Changming Sun, Michael Buckley, Dadong Wang, Melanie De Silva, Seong-Seng Tan, and Jenny M Gunnarsen. Automated analysis of neurite branching in cultured cortical neurons using hca-vision. *Cytometry Part A*, 71(10):889–895, 2007.
- [116] Toshiaki Takeda, Atsushi Ishikawa, Katsuhiko Ohtomo, Yukio Kobayashi, and Takahide Matsuoka. Fractal dimension of dendritic tree of cerebellar purkinje cell during onto-and phylogenetic development. *Neuroscience research*, 13(1):19–31, 1992.
- [117] Sidiney G Alves, Marcelo L Martins, Paula A Fernandes, and JoséE H Pittella. Fractal patterns for dendrites and axon terminals. *Physica A: Statistical Mechanics and its Applications*, 232(1):51–60, 1996.
- [118] Herbert F Jelinek and Eduardo Fernandez. Neurons and fractals: how reliable and useful are calculations of fractal dimensions? *Journal of neuroscience methods*, 81(1):9–18, 1998.
- [119] F Caserta, WD Eldred, E Fernandez, RE Hausman, LR Stanford, SV Bulderev, S Schwarzer, and HE Stanley. Determination of fractal dimension of physiologically characterized neurons in two and three dimensions. *Journal of neuroscience methods*, 56(2):133–144, 1995.
- [120] Dusica L Maric, Herbert F Jelinek, Nebojsa T Milosevic, and Katarina Rajkovic. Neurons of the human dentate nucleus: box-count method in the quantitative analysis of cell morphology. In *Control Systems and Computer Science (CSCS), 2013 19th International Conference on*, pages 319–324. IEEE, 2013.
- [121] Benoit B Mandelbrot. *The fractal geometry of nature*, volume 173. Macmillan, 1983.
- [122] Riccardo Leardi, Carla Armanino, Silvia Lanteri, and Luigi Alberotanza. Three-mode principal component analysis of monitoring data from venice lagoon. *Journal of Chemometrics*, 14(3):187–195, 2000.

- [123] Henk AL Kiers and Iven Van Mechelen. Three-way component analysis: Principles and illustrative application. *Psychological methods*, 6(1):84, 2001.
- [124] Jaap van Pelt, Arjen van Ooyen, and Harry BM Uylings. The need for integrating neuronal morphology databases and computational environments in exploring neuronal structure and function. *Anatomy and embryology*, 204(4):255–265, 2001.
- [125] Sara Gianola and Ferdinando Rossi. Evolution of the purkinje cell response to injury and regenerative potential during postnatal development of the rat cerebellum. *Journal of Comparative Neurology*, 430(1):101–117, 2001.
- [126] Madeline Pool, Joachim Thiemann, Amit Bar-Or, and Alyson E Fournier. Neuritracer: a novel imagej plugin for automated quantification of neurite outgrowth. *Journal of neuroscience methods*, 168(1):134–139, 2008.
- [127] NL Fazzalari and IH Parkinson. Fractal dimension and architecture of trabecular bone. *The Journal of pathology*, 178(1):100–105, 1996.
- [128] Hermann Cuntz, Friedrich Forstner, Alexander Borst, and Michael Häusser. One rule to grow them all: a general theory of neuronal branching and its practical application. *PLoS Comput Biol*, 6(8):e1000877, 2010.
- [129] Leo Kanner et al. *Autistic disturbances of affective contact*. publisher not identified, 1943.
- [130] Margaret L Bauman and Thomas L Kemper. Neuroanatomic observations of the brain in autism: a review and future directions. *International journal of developmental neuroscience*, 23(2):183–187, 2005.
- [131] Joachim Hallmayer, Sue Cleveland, Andrea Torres, Jennifer Phillips, Brianne Cohen, Tiffany Torigoe, Janet Miller, Angie Fedele, Jack Collins, Karen Smith, et al. Genetic heritability and shared environmental factors among twin pairs with autism. *Archives of general psychiatry*, 68(11):1095–1102, 2011.
- [132] Jamee M Berg and Daniel H Geschwind. Autism genetics: searching for specificity and convergence. *Genome Biol*, 13(7):247, 2012.
- [133] John E Schlerf, Joseph M Galea, Danny Spampinato, and Pablo A Celnik. Laterality differences in cerebellar–motor cortex connectivity. *Cerebral Cortex*, page bht422, 2014.
- [134] Catherine J Stoodley and Jeremy D Schmahmann. Functional topography in the human cerebellum: a meta-analysis of neuroimaging studies. *Neuroimage*, 44(2):489–501, 2009.
- [135] Roberta M Kelly and Peter L Strick. Cerebellar loops with motor cortex and prefrontal cortex of a nonhuman primate. *The Journal of Neuroscience*, 23(23):8432–8444, 2003.
- [136] Bruce E McKay and Ray W Turner. Physiological and morphological development of the rat cerebellar purkinje cell. *The Journal of physiology*, 567(3):829–850, 2005.
- [137] T Hollingworth and M Berry. Network analysis of dendritic fields of pyramidal cells in neocortex and purkinje cells in the cerebellum of the rat. *Philosophical Transactions of the Royal Society of London B: Biological Sciences*, 270(906):227–264, 1975.
- [138] Makoto Mori and Toshiya Matsushima. Post-hatch development of dendritic arborization in cerebellar purkinje neurons of quail chicks: a morphometric study. *Neuroscience letters*, 329(1):73–76, 2002.
- [139] Cristopher M Niell and Stephen J Smith. Live optical imaging of nervous system development. *Annu. Rev. Physiol.*, 66:771–798, 2004.

- [140] Gabriel A Silva and Brad Culp. High throughput algorithms for mapping the topology of neuronal and glial networks. In *Neural Engineering, 2005. Conference Proceedings. 2nd International IEEE EMBS Conference on*, pages 344–347. IEEE, 2005.
- [141] Eric COURCHESNE, Ruth CARPER, Natacha AKSHOOMOFF, and Janet E LAINHART. Evidence of brain overgrowth in the first year of life in autism. editorial. *JAMA, the journal of the American Medical Association*, 290(3):393–394, 2003.
- [142] Carl A Pinkert. *Transgenic animal technology: a laboratory handbook*. Newnes, 2014.
- [143] Manfred Zimmermann. Ethical principles for the maintenance and use of animals in neuroscience research. *Neuroscience letters*, 73(1):1, 1987.
- [144] Susan Folstein and Michael Rutter. Genetic influences and infantile autism. *Nature*, 1977.
- [145] Christopher W Bartlett, Neda Gharani, James H Millonig, and Linda M Brzustowicz. Three autism candidate genes: a synthesis of human genetic analysis with other disciplines. *International Journal of developmental neuroscience*, 23(2):221–234, 2005.
- [146] E Costa, Y Chen, J Davis, E Dong, JS Noh, L Tremolizzo, M Veldic, DR Grayson, and A Guidotti. Reelin and schizophrenia. *Molecular interventions*, 2(1):47, 2002.
- [147] Tom E Andersen, Bente Finsen, Andre M Goffinet, Olaf-Georg Issinger, and Brigitte Boldyreff. A reeler mutant mouse with a new, spontaneous mutation in the reelin gene. *Molecular brain research*, 105(1):153–156, 2002.
- [148] Yves Jossin, Masuhara Ogawa, Christine Metin, Fadel Tissir, and André M Goffinet. Inhibition of src family kinases and non-classical protein kinases c induce a reeler-like malformation of cortical plate development. *The Journal of neuroscience*, 23(30):9953–9959, 2003.
- [149] Flavio Keller and Antonio M Persico. The neurobiological context of autism. *Molecular neurobiology*, 28(1):1–22, 2003.
- [150] Fadel Tissir and André M Goffinet. Reelin and brain development. *Nature Reviews Neuroscience*, 4(6):496–505, 2003.
- [151] DS Falconer. Two new mutants, trembler and reeler, with neurological actions in the house mouse (*mus musculus* l.). *Journal of genetics*, 50(2):192–205, 1951.
- [152] Verne S Caviness Jr and Pasko Rakic. Mechanisms of cortical development: a view from mutations in mice. *Annual review of neuroscience*, 1(1):297–326, 1978.
- [153] AM Goffinet. Events governing organization of postmigratory neurons: studies on brain development in normal and reeler mice. *Brain Research Reviews*, 7(3):261–296, 1984.
- [154] AM Goffinet. Determinants of nerve cell patterns during development: a review. *European journal of morphology*, 28(2-4):149–168, 1989.
- [155] Gabriella D’Arcangelo, Graham G Miao, Shu-Cheng Chen, Holly D Scares, James I Morgan, and Tom Curran. A protein related to extracellular matrix proteins deleted in the mouse mutant reeler. 1995.
- [156] Udaya DeSilva, Gabriella D’Arcangelo, Valerie V Braden, June Chen, Graham G Miao, Tom Curran, and Eric D Green. The human reelin gene: isolation, sequencing, and mapping on chromosome 7. *Genome research*, 7(2):157–164, 1997.

- [157] Susan E Hong, Yin Yao Shugart, David T Huang, Saad Al Shahwan, P Ellen Grant, Jonathan O'B Hourihane, Neil DT Martin, and Christopher A Walsh. Autosomal recessive lissencephaly with cerebellar hypoplasia is associated with human *reln* mutations. *Nature genetics*, 26(1):93–96, 2000.
- [158] Francesco Impagnatiello, Alessandro R Guidotti, Christine Pesold, Yogesh Dwivedi, Hector Caruncho, Maria G Pisu, Doncho P Uzunov, Neil R Smalheiser, John M Davis, Ghanshyam N Pandey, et al. A decrease of *reelin* expression as a putative vulnerability factor in schizophrenia. *Proceedings of the National Academy of Sciences*, 95(26):15718–15723, 1998.
- [159] Alessandro Guidotti, James Auta, John M Davis, Valeria DiGiorgi Gerevini, Yogesh Dwivedi, Dennis R Grayson, Francesco Impagnatiello, Ghanshyam Pandey, Christine Pesold, Rajiv Sharma, et al. Decrease in *reelin* and glutamic acid decarboxylase67 (*gad67*) expression in schizophrenia and bipolar disorder: a postmortem brain study. *Archives of general psychiatry*, 57(11):1061–1069, 2000.
- [160] SH Fatemi. *Reelin* mutations in mouse and man: from reeler mouse to schizophrenia, mood disorders, autism and lissencephaly. *Molecular psychiatry*, 2001.
- [161] Patricia Tueting, Erminio Costa, Yogesh Dwivedi, Alessandro Guidotti, Francesco Impagnatiello, Radmila Manev, and Christine Pesold. The phenotypic characteristics of heterozygous reeler mouse. *Neuroreport*, 10(6):1329–1334, 1999.
- [162] Wen Sheng Liu, Christine Pesold, Miguel A Rodriguez, Giovanni Carboni, James Auta, Pascal Lacor, John Larson, Brian G Condie, Alessandro Guidotti, and Erminio Costa. Down-regulation of dendritic spine and glutamic acid decarboxylase 67 expressions in the *reelin* haploinsufficient heterozygous reeler mouse. *Proceedings of the National Academy of Sciences*, 98(6):3477–3482, 2001.
- [163] Walter L Salinger, Pamela Ladrow, and Catherine Wheeler. Behavioral phenotype of the reeler mutant mouse: effects of *reln* gene dosage and social isolation. *Behavioral neuroscience*, 117(6):1257, 2003.
- [164] Elisa Ognibene, Walter Adriani, Oleg Granstrem, Stefano Pieretti, and Giovanni Laviola. Impulsivity–anxiety-related behavior and profiles of morphine-induced analgesia in heterozygous reeler mice. *Brain research*, 1131:173–180, 2007.
- [165] Elisa Ognibene, Walter Adriani, Simone Macri, and Giovanni Laviola. Neurobehavioural disorders in the infant reeler mouse model: interaction of genetic vulnerability and consequences of maternal separation. *Behavioural brain research*, 177(1):142–149, 2007.
- [166] Maria Cristina Marrone, Silvia Marinelli, Filippo Biamonte, Flavio Keller, Carmelo Alessio Sgobio, Martine Ammassari-Teule, Giorgio Bernardi, and Nicola B Mercuri. Altered cortico-striatal synaptic plasticity and related behavioural impairments in reeler mice. *European Journal of Neuroscience*, 24(7):2061–2070, 2006.
- [167] Ekrem Maloku, Ignacio R Covelo, Ingeborg Hanbauer, Alessandro Guidotti, Bashkim Kadriu, Qiaoyan Hu, John M Davis, and Erminio Costa. Lower number of cerebellar purkinje neurons in psychosis is associated with reduced *reelin* expression. *Proceedings of the National Academy of Sciences*, 107(9):4407–4411, 2010.
- [168] Barbara Kuemerle, Forrest Gulden, Natalie Cherosky, Elizabeth Williams, and Karl Herrup. The mouse engrailed genes: a window into autism. *Behavioural brain research*, 176(1):121–132, 2007.
- [169] Stephan L Baader, Salih Sanlioglu, Albert S Berrebi, Jan Parker-Thornburg, and John Oberdick. Ectopic overexpression of engrailed-2 in cerebellar purkinje cells causes restricted cell loss and retarded external germinal layer development at lobule junctions. *The Journal of neuroscience*, 18(5):1763–1773, 1998.

- [170] Rym Benayed, Neda Gharani, Ian Rossman, Vincent Mancuso, Gloria Lazar, Silky Kamdar, Shannon E Bruse, Samuel Tischfield, Brett J Smith, Raymond A Zimmerman, et al. Support for the homeobox transcription factor gene engrailed 2 as an autism spectrum disorder susceptibility locus. *The American Journal of Human Genetics*, 77(5):851–868, 2005.
- [171] Ian T Rossman, Lulu Lin, Katherine M Morgan, Marissa DiGiovine, Elise K Van Buskirk, Silky Kamdar, James H Millonig, and Emanuel DiCicco-Bloom. Engrailed2 modulates cerebellar granule neuron precursor proliferation, differentiation and insulin-like growth factor 1 signaling during postnatal development. *Molecular autism*, 5(1):1, 2014.
- [172] Michelle A Cheh, James H Millonig, Lauren M Roselli, Xue Ming, Erin Jacobsen, Silky Kamdar, and George C Wagner. En2 knockout mice display neurobehavioral and neurochemical alterations relevant to autism spectrum disorder. *Brain research*, 1116(1):166–176, 2006.
- [173] Roger A Gorski, John H Gordon, James E Shryne, and Arthur M Southam. Evidence for a morphological sex difference within the medial preoptic area of the rat brain. *Brain research*, 148(2):333–346, 1978.
- [174] GC Panzica, C Viglietti-Panzica, M Calagni, GC Anselmetti, M Schumacher, and Jacques Balthazart. Sexual differentiation and hormonal control of the sexually dimorphic medial preoptic nucleus in the quail. *Brain research*, 416(1):59–68, 1987.
- [175] Shoshana Spring, Jason P Lerch, and R Mark Henkelman. Sexual dimorphism revealed in the structure of the mouse brain using three-dimensional magnetic resonance imaging. *Neuroimage*, 35(4):1424–1433, 2007.
- [176] Bradley Cooke, Carol D Hegstrom, Loic S Villeneuve, and S Marc Breedlove. Sexual differentiation of the vertebrate brain: principles and mechanisms. *Frontiers in neuroendocrinology*, 19(4):323–362, 1998.
- [177] Jill M Goldstein, Larry J Seidman, Nicholas J Horton, Nikos Makris, David N Kennedy, Verne S Caviness, Stephen V Faraone, and Ming T Tsuang. Normal sexual dimorphism of the adult human brain assessed by in vivo magnetic resonance imaging. *Cerebral cortex*, 11(6):490–497, 2001.
- [178] Laura S Allen and Roger A Gorski. Sexual dimorphism of the anterior commissure and massa intermedia of the human brain. *Journal of Comparative Neurology*, 312(1):97–104, 1991.
- [179] John H Gilmore, Weili Lin, Marcel W Prastawa, Christopher B Looney, Y Sampath K Vetsa, Rebecca C Knickmeyer, Dianne D Evans, J Keith Smith, Robert M Hamer, Jeffrey A Lieberman, et al. Regional gray matter growth, sexual dimorphism, and cerebral asymmetry in the neonatal brain. *The Journal of neuroscience*, 27(6):1255–1260, 2007.
- [180] Jay N Giedd, F Xavier Castellanos, Jagath C Rajapakse, A Catherine Vaituzis, and Judith L Rapoport. Sexual dimorphism of the developing human brain. *Progress in Neuro-Psychopharmacology and Biological Psychiatry*, 21(8):1185–1201, 1997.
- [181] Peg Nopoulos, Michael Flaum, Dan OLeary, and Nancy C Andreasen. Sexual dimorphism in the human brain: evaluation of tissue volume, tissue composition and surface anatomy using magnetic resonance imaging. *Psychiatry Research: Neuroimaging*, 98(1):1–13, 2000.
- [182] Simon Baron-Cohen, Rebecca C Knickmeyer, and Matthew K Belmonte. Sex differences in the brain: implications for explaining autism. *Science*, 310(5749):819–823, 2005.
- [183] Naftali Raz, Faith Gunning-Dixon, Denise Head, Karen M Rodrigue, Adrienne Williamson, and James D Acker. Aging, sexual dimorphism, and hemispheric asymmetry of the cerebral cortex: replicability of regional differences in volume. *Neurobiology of aging*, 25(3):377–396, 2004.



- [184] Sergio Mora, Nelson Dussaubat, and Gabriela Díaz-Véliz. Effects of the estrous cycle and ovarian hormones on behavioral indices of anxiety in female rats. *Psychoneuroendocrinology*, 21(7):609–620, 1996.
- [185] Paola Palanza. Animal models of anxiety and depression: how are females different? *Neuroscience & Biobehavioral Reviews*, 25(3):219–233, 2001.
- [186] Jennifer Connellan, Simon Baron-Cohen, Sally Wheelwright, Anna Batki, and Jag Ahluwalia. Sex differences in human neonatal social perception. *Infant Behavior and Development*, 23(1):113–118, 2000.
- [187] Lorna Wing. Sex ratios in early childhood autism and related conditions. *Psychiatry research*, 5(2):129–137, 1981.
- [188] Bernard Rimland. Infantile autism. 1964.
- [189] Simon Baron-Cohen. The extreme male brain theory of autism. *Trends in cognitive sciences*, 6(6):248–254, 2002.
- [190] David H Skuse. Imprinting, the x-chromosome, and the male brain: explaining sex differences in the liability to autism. *Pediatric Research*, 47(1):9–9, 2000.
- [191] Catherine Lord, Eric Schopler, and Dennis Revicki. Sex differences in autism. *Journal of autism and developmental disorders*, 12(4):317–330, 1982.
- [192] Sébastien Jacquemont, Bradley P Coe, Micha Hersch, Michael H Duyzend, Niklas Krumm, Sven Bergmann, Jacques S Beckmann, Jill A Rosenfeld, and Evan E Eichler. A higher mutational burden in females supports a female protective model in neurodevelopmental disorders. *The American Journal of Human Genetics*, 94(3):415–425, 2014.
- [193] Hans Asperger and Uta Trans Frith. 'autistic psychopathy' in childhood. 1991.
- [194] T Brugha, S McManus, H Meltzer, J Smith, FJ Scott, S Purdon, J Harris, and J Bankart. Autism spectrum disorders in adults living in households throughout england: Report from the adult psychiatric morbidity survey 2007. *Leeds: The NHS Information Centre for Health and Social Care*, 2009.
- [195] Tony Attwood. Strategies for improving the social integration of children with asperger syndrome. *Autism*, 4(1):85–100, 2000.
- [196] Stephan Ehlers and Christopher Gillberg. The epidemiology of asperger syndrome. *Journal of child psychology and psychiatry*, 34(8):1327–1350, 1993.
- [197] Judith Gould and Jacqui Ashton-Smith. Missed diagnosis or misdiagnosis? girls and women on the autism spectrum. *Good Autism Practice (GAP)*, 12(1):34–41, 2011.
- [198] Shannon L Dean and Margaret M McCarthy. Steroids, sex and the cerebellar cortex: implications for human disease. *The cerebellum*, 7(1):38–47, 2008.
- [199] EB Becker and Catherine J Stoodley. Autism spectrum disorder and the cerebellum. *Int Rev Neurobiol*, 113:1–34, 2013.
- [200] Gabriella D'Arcangelo. Reelin in the years: controlling neuronal migration and maturation in the mammalian brain. *Advances in Neuroscience*, 2014, 2014.
- [201] Giovanni Laviola, Elisa Ognibene, Emilia Romano, Walter Adriani, and Flavio Keller. Gene-environment interaction during early development in the heterozygous reeler mouse: clues for modelling of major neurobehavioral syndromes. *Neuroscience & Biobehavioral Reviews*, 33(4):560–572, 2009.

- [202] Filippo Biamonte, Giovanni Assenza, Ramona Marino, Marcello D’Amelio, Roger Panteri, Donatella Caruso, Samuele Scurati, Josue Garcia Yague, Luis Miguel Garcia-Segura, Roberta Cesa, et al. Interactions between neuroactive steroids and reelin haploinsufficiency in purkinje cell survival. *Neurobiology of disease*, 36(1):103–115, 2009.
- [203] N Hadj-Sahraoui, F Frederic, N Delhaye-Bouchaud, and J Mariani. Gender effect on purkinje cell loss in the cerebellum of the heterozygous reeler mouse. *Journal of neurogenetics*, 11(1-2):45–58, 1996.
- [204] Autumn D Abadesco, Marianne Cilluffo, Griselda M Yvone, Ellen M Carpenter, Brian W Howell, and Patricia E Phelps. Novel disabled-1-expressing neurons identified in adult brain and spinal cord. *European Journal of Neuroscience*, 39(4):579–592, 2014.
- [205] Takaki Miyata, Kazunori Nakajima, Katsuhiko Mikoshiba, and Masaharu Ogawa. Regulation of purkinje cell alignment by reelin as revealed with cr-50 antibody. *The Journal of neuroscience*, 17(10):3599–3609, 1997.
- [206] Takayuki Uchida, Atsushi Baba, F Javier Pérez-Martínez, Terumasa Hibi, Takaki Miyata, Juan M Luque, Kazunori Nakajima, and Mitsuharu Hattori. Downregulation of functional reelin receptors in projection neurons implies that primary reelin action occurs at early/premigratory stages. *The Journal of Neuroscience*, 29(34):10653–10662, 2009.
- [207] Luis Miguel Garcia-Segura and Julio Perez-Marquez. A new mathematical function to evaluate neuronal morphology using the sholl analysis. *Journal of neuroscience methods*, 226:103–109, 2014.
- [208] Josef P Kapfhammer and Olivia S Gugger. The analysis of purkinje cell dendritic morphology in organotypic slice cultures. *Journal of visualized experiments: JoVE*, (61), 2012.
- [209] SA Tobet and TO Fox. Sex differences in neuronal morphology influenced hormonally throughout life. In *Sexual differentiation*, pages 41–83. Springer, 1992.
- [210] Jennifer Brielmaier, Paul G Matteson, Jill L Silverman, Julia M Senerth, Samantha Kelly, Matthieu Genestine, James H Millonig, Emanuel DiCicco-Bloom, and Jacqueline N Crawley. Autism-relevant social abnormalities and cognitive deficits in engrailed-2 knockout mice. *PLoS one*, 7(7):e40914, 2012.
- [211] LR Edelstein and FJ Denaro. The claustrum: a historical review of its anatomy, physiology, cytochemistry and functional significance. *PATHOLOGY*, 104:368–415, 2004.
- [212] John-Irwin Johnson, Brian A Fenske, Amar S Jaswa, and John A Morris. Exploitation of puddles for breakthroughs in claustrum research. *Frontiers in systems neuroscience*, 8, 2014.
- [213] Brian N Mathur. The claustrum in review. *The Claustrum: charting a way forward for the brains most mysterious nucleus*, page 7, 2015.
- [214] Richard F Thompson and Jon A Shaw. Behavioral correlates of evoked activity recorded from association areas of the cerebral cortex. *Journal of Comparative and Physiological Psychology*, 60(3):329, 1965.
- [215] George Ettliger and WA Wilson. Cross-modal performance: behavioural processes, phylogenetic considerations and neural mechanisms. *Behavioural brain research*, 40(3):169–192, 1990.
- [216] John Smythies, Lawrence Edelstein, and Vilayanur Ramachandran. Hypotheses relating to the function of the claustrum. *Front. Integr. Neurosci*, 6(53):10–3389, 2012.
- [217] Jared B Smith and Kevin D Alloway. Interhemispheric claustral circuits coordinate sensory and motor cortical areas that regulate exploratory behaviors. *The Claustrum: charting a way forward for the brains most mysterious nucleus*, 2015.

- [218] Yael Goll, Gal Atlan, and Ami Citri. Attention: the claustrum. *Trends in neurosciences*, 38(8):486–495, 2015.
- [219] S LeVay and H Sherk. The visual claustrum of the cat. i. structure and connections. *The Journal of Neuroscience*, 1(9):956–980, 1981.
- [220] R Druga. Neocortical inhibitory system. *Folia biologica*, 55(6):201, 2009.
- [221] Xiangmin Xu, Keith D Roby, and Edward M Callaway. Immunochemical characterization of inhibitory mouse cortical neurons: three chemically distinct classes of inhibitory cells. *Journal of Comparative Neurology*, 518(3):389–404, 2010.
- [222] György Buzsáki, Cornelius H Vanderwolf, et al. Cellular bases of hippocampal eeg in the behaving rat. *Brain Research Reviews*, 6(2):139–171, 1983.
- [223] Miles A Whittington, Roger D Traub, and John GR Jefferys. Synchronized oscillations in interneuron networks driven by metabotropic glutamate receptor activation. 1995.
- [224] Gábor Tamás, Eberhard H Buhl, Andrea Lörincz, and Peter Somogyi. Proximally targeted gabaergic synapses and gap junctions synchronize cortical interneurons. *Nature neuroscience*, 3(4):366–371, 2000.
- [225] Emilio Salinas and Terrence J Sejnowski. Correlated neuronal activity and the flow of neural information. *Nature reviews neuroscience*, 2(8):539–550, 2001.
- [226] Marlene Bartos, Imre Vida, and Peter Jonas. Synaptic mechanisms of synchronized gamma oscillations in inhibitory interneuron networks. *Nature reviews neuroscience*, 8(1):45–56, 2007.
- [227] Tamás F Freund and István Katona. Perisomatic inhibition. *Neuron*, 56(1):33–42, 2007.
- [228] Guillermo Gonzalez-Burgos and David A Lewis. Gaba neurons and the mechanisms of network oscillations: implications for understanding cortical dysfunction in schizophrenia. *Schizophrenia bulletin*, 34(5):944–961, 2008.
- [229] Anita K Roopun, Mark O Cunningham, Claudia Racca, Kai Alter, Roger D Traub, and Miles A Whittington. Region-specific changes in gamma and beta2 rhythms in nmda receptor dysfunction models of schizophrenia. *Schizophrenia bulletin*, 34(5):962–973, 2008.
- [230] Jessica A Cardin, Marie Carlén, Konstantinos Meletis, Ulf Knoblich, Feng Zhang, Karl Deisseroth, Li-Huei Tsai, and Christopher I Moore. Driving fast-spiking cells induces gamma rhythm and controls sensory responses. *Nature*, 459(7247):663–667, 2009.
- [231] Peter J Uhlhaas and Wolf Singer. Abnormal neural oscillations and synchrony in schizophrenia. *Nature reviews neuroscience*, 11(2):100–113, 2010.
- [232] Takaichi Fukuda. Structural organization of the gap junction network in the cerebral cortex. *The Neuroscientist*, 13(3):199–207, 2007.
- [233] Ma Angeles Real, José Carlos Dávila, and Salvador Guirado. Expression of calcium-binding proteins in the mouse claustrum. *Journal of chemical neuroanatomy*, 25(3):151–160, 2003.
- [234] S<sup>3</sup>awomir Wójcik, Jerzy Dziewiatkowski, Edyta Spodnik, Beata Ludkiewicz, Beata Domaradzka-Pytel, Przemys<sup>3</sup>aw Kowiański, and Janusz Morys. Analysis of calcium binding protein immunoreactivity in the claustrum and the endopiriform nucleus of the rabbit. *Acta neurobiologiae experimentalis*, 64(4):449–460, 2004.
- [235] Fahad E Rahman and Joan S Baizer. Neurochemically defined cell types in the claustrum of the cat. *Brain research*, 1159:94–111, 2007.

- [236] Bruno Cozzi, Giulia Roncon, Alberto Granato, Maristella Giurisato, Maura Castagna, Antonella Peruffo, Mattia Panin, Cristina Ballarin, Stefano Montelli, and Andrea Pirone. The claustrum of the bottlenose dolphin *tursiops truncatus* (montagu 1821). *The Claustrum: charting a way forward for the brains most mysterious nucleus*, page 47, 2015.
- [237] Andrea Pirone, Maura Castagna, Alberto Granato, Antonella Peruffo, Francesca Quilici, Laura Cavicchioli, Ilaria Piano, Carla Lenzi, and Bruno Cozzi. Expression of calcium-binding proteins and selected neuropeptides in the human, chimpanzee, and crab-eating macaque claustrum. *Frontiers in systems neuroscience*, 8, 2014.
- [238] DV Hinova-Palova, L Edelstein, BV Landzhov, E Braak, LG Malinova, M Minkov, A Paloff, and W Ovtcharoff. Parvalbumin-immunoreactive neurons in the human claustrum. *Brain Structure and Function*, 219(5):1813–1830, 2014.
- [239] David Arthur and Sergei Vassilvitskii. k-means++: The advantages of careful seeding. In *Proceedings of the eighteenth annual ACM-SIAM symposium on Discrete algorithms*, pages 1027–1035. Society for Industrial and Applied Mathematics, 2007.
- [240] MR Celio. Calbindin d-28k and parvalbumin in the rat nervous system. *Neuroscience*, 35(2):375–475, 1990.
- [241] Dimka V Hinova-Palova, Lawrence R Edelstein, Adrian M Paloff, Stanislav Hristov, Vassil G Papanchev, and Wladimir A Ovtcharoff. Parvalbumin in the cat claustrum: ultrastructure, distribution and functional implications. *Acta histochemica*, 109(1):61–77, 2007.
- [242] K Reynhout and JS Baizer. Immunoreactivity for calcium-binding proteins in the claustrum of the monkey. *Anatomy and embryology*, 199(1):75–83, 1999.
- [243] Christof Koch and Idan Segev. The role of single neurons in information processing. *nature neuroscience*, 3:1171–1177, 2000.

